Thermal modelling of water-cooled electric machines of some tens of kilowatts

vorgelegt als Dissertation

zur Erlangung des akademischen Grades
Doktor der technischen Wissenschaften

an der

Technischen Universität Graz

von

Dipl.-Ing. Hendrik Kolbe

1. Gutachter: Univ.-Prof. Dr.-Ing. Annette Mütze
Institut für Elektrische Antriebstechnik und Maschinen (EAM)
Technische Universität Graz, Österreich
2. Gutachter: Assoc. Prof. Dr. Andrea Cavagnino
Dipartimento Energia (DENERG)
Politecnico di Torino, Italia

2015

STATUTORY DECLARATION

I declare that I have authored this thesis independently, that I have not used other than the declared sources / resources and that I have explicitly marked all material which has been quoted either literally or by content from the used sources.

…….. ……..

date (signature)

Contents

Abstract

Thermal modelling of electric machines forms a vital and integral part of electric machine design and analysis. Attempts to boost the utilisation or the efficiency of electric machines even increase the importance of thermal considerations during machine design and analysis.

In order to understand or even predict the thermal behaviour of electric machines, both the heat generation and the heat transfer mechanisms in electric machines need to be understood.

In the first part, a detailed analysis of the key components is carried out by analytic and numerical means targeting at not only providing a comprehensive overview of the relevant components and the available methods and tools for the analysis but also to review the modelling approaches themselves. Particularly the parallel model development of the same components—with specific differences and similarities between both modelling approaches—allows to verify and compare the models.

The target of a subsequent case study of a tested induction machine is to merge the two modelling concepts, the analytic and the numerical modelling, with actual measurements of the induction machine. For this purpose, several specific experimental tests are carried out and the corresponding analytic and numerical simulations are run. The comparison of the simulation results with the measurements allows to verify not only the models but also to better understand the connection between simulated and measured values and to identify potential strengths and weaknesses.

Zusammenfassung

Das Streben nach einer Erhöhung der Ausnutzung elektrischer Maschinen (teilweise einhergehend mit einer stärkeren thermischen Beanspruchung) wie auch die Tatsache, dass elektrische Maschinen in zunehmenden Maße nicht mehr nur in ei-

nem fixen Bemessungspunkt oder einem festgelegten einfachen Bereich betrieben werden, erfordern ein besseres Verständnis des thermischen Verhaltens elektrischer Maschinen. Neben der Fragestellung der korrekten Modellierung der Wärmepfade kommt auch der möglichst akkuraten Modellierung der Verlustquellen eine entscheidende Rolle zu, da die Verluste die Eingangsgrößen der thermischen Modelle darstellen und somit einen unmittelbaren Einfluss auf die Ergebnisse haben.

Die für thermische Simulationen zur Verfügung stehenden analytischen und numerischen Methoden und Werkzeuge werden in einem ersten Schritt zur vergleichenden Analyse der thermischen Modellierung der verschiedenen Komponenten eletrischer Maschinen verwendet. Der parallele Aufbau analytischer und numerischer Modelle ermöglicht hierbei eine vergleichende Betrachung der beiden Ansätze und auch eine Verifikation der Modelle.

Eine Asynchronmaschine dient in einem weiteren Schritt als Fallbeispiel, um Gesamtmodelle elektrischer Maschinen auf Basis der beiden Modellierungsansätz gegenüberstellen und mit Ergebnissen experimenteller Tests vergleichen zu können. Spezielle experimentelle Tests mit einer reduzierteren Komplexität in Bezug auf die Verluste und die relevanten Wärmepfade erlauben hierbei eine erleichterte und zielgerichtete Analyse und Validierung.

Overview of Contribution

Thermal modelling of electric machines is a combined problem of how to adequately model the separate components and of how to combine the component models to an overall model. Studying the thermal behaviour of electric machines furthermore comprises the study of the different heat transfer mechanisms heat conduction, convection and radiation, which are all present in electric machines. Additional complexity is added by the input of the thermal simulations, namely the losses, which are generated in different components of electric machines and which are by themselves complex phenomena.

Numerous thermal models have been developed that cover a wide range of aspects associated with the thermal analysis of machines, ranging from very detailed analyses of specific effects (e.g. the convective heat transfer in the end winding region of special machine types) to thermal models that allow for the analysis of complete machines with complex cooling systems.

Yet, even though the thermal analysis has been the subject of research for more than one century, both the complex loss phenomena in electric machines (being the input for the thermal models) and the heat transfer mechanisms in the complex motor assemblies are still active fields of research. The advance of numerical methods and tools and the general availability of powerful computers, for instance, provide researchers with a powerful method capable of potentially refined thermal analyses, while modern variable-speed drives introduce additional challenges with respect to the generated losses and the dynamic operational patterns at the same time.

This work targets at introducing, analysing and interpreting the thermal component modelling as well as the modelling of complete machines, using the available analytic and numerical tools and methods. A particular focus is put on the provision of reference models or reference data for the model validation. This more holistic approach differs from existing works in that analytic and numerical models are consistently developed in parallel, wherever possible. The analytic and the numerical approaches are, additionally, compared with respect to underlying assumptions and their effects on the simulation results.

In a following step, the analytic and the numerical component models are incorporated in an analytic as well as in a numerical modelling framework (respectively)

that allow to simulate a complete electric machine. Experimental tests furthermore allow to not only compare analytic and numerical simulations but also to merge both modelling approaches with actual measurements.

In contrast to most studies, in which the target and also the criterion for the model accuracy is the best match with measurement data, the target in this work is not to develop and to adjust thermal models in order to achieve the best match between the developed models and benchmark models or measurements. By contrast, the fact that no hidden calibrations are carried out but deviations are accepted, a more transparent analysis and discussion is expected together with offering a better insight into the challenges related to field of thermal modelling.

The component modelling is analysed by reviewing the existing modelling approaches or models first and, subsequently, by deriving analytic and numerical models. Where an explicit modelling is not possible or feasible, e.g. in the case of the contact resistances, the possible consideration in analytic and numerical models is explained.

Experimental tests of an induction machine, which has been equipped with thermal sensors, extends the component modelling in that an additional source for verification is provided. Similar to the analysis of the component modelling, the aim of the case study is not to achieve the best match with e.g. just one standard load point, which would easily be possible with some parameter adjustments. Instead, the partly even very significant deviations permit to discuss associated challenges when using different modelling techniques and when trying to merge those with measured data.

Symbols

Roman

A	Area, cross-sectional area, interface area, area of bearing seating	m^2
A_i	Area; i = index	m^2
$\hat{B}$	Peak value of the magnetic field strength	T
b_b	Bearing width	m
Bi	Biot number	1
$\mathbf{C}$	Matrix of thermal capacities	$\frac{J}{K}$
$C_{b,dyn}$	Basic dynamic load rating	N
c_{fr}	Friction coefficient	1
c_p	Specific heat (at constant pressure)	$\frac{J}{kg\,K}$
C_{th}	(Lumped) Thermal capacitance	$\frac{J}{K}$
$C_{th,cj}$	(Lumped) Thermal capacitance of the cooling jacket	$\frac{J}{K}$
$C_{th,i}$	(Lumped) Thermal capacitance; i = index	$\frac{J}{K}$
D	Bearing outer diameter	m
d	Thickness	m
d_b	(Bearing) Bore diameter	m
$\overline{d}_b$	Mean bearing diameter	m
d_{co}	Wire copper diameter	m
d_h	Hydraulic diameter	m
d_s	Seal counterface diameter	m
d_{wire}	Wire diameter	m
E_{rad}	Rate of energy radiation per unit surface area	$\frac{W}{m^2}$
f	Frequency	Hz
f_{0b}	Coefficient for the speed-dependent frictional torque	1
f_1	Stator frequency	Hz
F_{12}	Shape factor between surfaces 1 and 2	1

f_{1b}	Coefficient for the load-dependent frictional torque	1
f_2	Rotor frequency	Hz
f_{ra}	Rated stator frequency	Hz
$\mathbf{G}$	(Thermal) Conductance matrix	$\frac{W}{K}$
g	Gravitational acceleration; $g = 9.8\,\frac{m}{s^2}$	$\frac{m}{s^2}$
$G_{i,j}$	Entry in (thermal) conductance matrix, i: row index, j: column index	$\frac{W}{K}$
$g_{i,j}$	Thermal conductance between node i and node j	$\frac{W}{K}$
h	(Local) Heat transfer coefficient	$\frac{W}{m^2\,K}$
$\overline{h}$	Average heat transfer coefficient	$\frac{W}{m^2\,K}$
h_{intf}	(Thermal) Interface conductance	$\frac{W}{m^2\,K}$
$\vec{I}$	Vector containing the current of each phase	A
I_1	Stator current	A
I_2	Rotor current	A
I_μ	Magnetising current	A
I_{phRMS}	Effective current through one phase	A
I_{ra}	Rated stator current	A
$k_{cc,i}$	Convection correlation factor; i = index	1
k_{ec}	Empirical factor used for the estimation of eddy current losses	1
k_{hyst}	Empirical factor used for the estimation of hysteresis losses	1
k_q	Heat transfer coefficient of bearing seating surface	$\frac{W}{m^2\,K}$
k_{rou}	Roughness factor	1
k_{s1}	First empirical factor for the calculation of sealing losses	1
k_{s2}	Second empirical factor for the calculation of sealing losses	1
L	Characteristic length	m
l	Length, axial rotor/stator stack length	m
$L_{1\sigma}$	Stator leakage inductance	H
$L_{2\sigma}$	Rotor leakage inductance	H
$L'_{2\sigma}$	Rotor leakage inductance referred to the stator	H
l_{cyl}	Cylinder or pipe length	m
L_h	Magnetising inductance	H
l_r	Rotor length	m

l_w	Wetted perimeter	m
M	Output torque	N m
$\dot{m}$	Mass flow rate	$\frac{kg}{s}$
m	Number of phases	1
M_0	Speed-dependent frictional torque	N m
M_1	Load-dependent frictional torque	N m
M_b	Frictional bearing torque	N m
M_{seal}	Sealing torque	N m
n	Rotational speed	$\frac{1}{s}$
n_{hyst}	Empirical exponent used for the estimation of hysteresis losses	1
Nu	Nusselt number	1
$\overline{Nu}$	Average Nusselt number	1
$\vec{P}$	Vector containing the input power of each phase; vector of loss injections	W
p	Number of pole pairs	1
P_{lb}	Bearing load	N
P_{add}	Additional losses	W
P'_{airGap}	Losses per unit length generated in the air gap	$\frac{W}{m}$
P_{be}	Frictional bearing losses	W
p_{ec}	Eddy current losses per unit mass	$\frac{W}{kg}$
p_{hyst}	Hysteresis losses per unit mass	$\frac{W}{kg}$
P_i	Loss injection; i = index	W
p_{iron}	Total iron losses per unit mass	$\frac{W}{kg}$
$\overline{P}_{Joule}$	Average Joule losses of winding	W
Pr	Prandtl number	1
P_{ra}	Rated input power	W
P_{rot}	Injected losses from the rotor	W
P_{sl}	Copper slot losses	W
P_{wi}	Windage losses	W
$\dot{Q}$	Heat flow rate	W
$\vec{q}$	Local heat flux density (vector)	$\frac{W}{m^2}$

q	Local heat flux density	$\frac{W}{m^2}$
$\dot{q}$	Heat generation rate per unit volume	$\frac{W}{m^3}$
Q_r	Number of rotor slots	1
r	Radial position (radius) in a hollow cylinder	m
R_1	Resistance of the stator winding	Ω
R_2	Resistance of the rotor winding	Ω
R_2'	Resistance of the rotor winding referred to the stator	Ω
Ra	Rayleigh number	1
R_{add}	Equivalent resistance of additional losses	Ω
R_{bar}	Resistance of a rotor bar	Ω
Re	Reynolds number	1
R_{er}	End ring resistance	Ω
R_{FE}	Equivalent resistance of iron losses	Ω
r_i	Radius; i = index	m
R_{ph}	Resistance of one phase	Ω
$r_{r,o}$	Outer radius of the rotor	m
R_{th}	Thermal resistance	$\frac{K}{W}$
$R_{th,be}$	Thermal bearing resistance	$\frac{K}{W}$
$R_{th,beIn}$	Thermal bearing resistance at the inner bearing seating	$\frac{K}{W}$
$R_{th,beOut}$	Thermal bearing resistance at the outer bearing seating	$\frac{K}{W}$
$R_{th,cond}$	Thermal resistance due to conduction	$\frac{K}{W}$
$R_{th,cont}$	Thermal contact resistance	$\frac{K}{W}$
$R_{th,conv}$	Thermal resistance due to convection	$\frac{K}{W}$
$R_{th,i}$	Thermal resistance; i = index	$\frac{K}{W}$
$R_{th,rad}$	Thermal resistance due to radiation	$\frac{K}{W}$
$R_{th,sli}$	Equivalent thermal slot resistance; i = index	$\frac{K}{W}$
$R_{th,sti}$	Equivalent thermal of resistance of the stator stack; i = index	$\frac{K}{W}$
S	Shape factor	m
s	Slip	1
T	Temperature	K
t	Time	s

Ta	Taylor number	1
T_{av}	Average temperature	K
T_i	Temperature; i = index	K
T_p	Plate temperature	K
T_∞	Free-stream temperature, ambient temperature	K
u_∞	Free-stream velocity	$\frac{m}{s}$
$\vec{V}$	Vector containing the voltage of each phase	V
V	Volume	m^3
v	Velocity	$\frac{m}{s}$
V_1	Line voltage	V
w_{hyst}	Energy per unit volume required for one cycle in the hysteresis curve	$\frac{J}{m^3}$

Greek

α	Thermal diffusivity	$\frac{m^2}{s}$
$\alpha_{20,Al}$	Linear temperature coefficient of the specific resistivity of aluminium at 20 °C	$\frac{1}{K}$
$\alpha_{20,Co}$	Linear temperature coefficient of the specific resistivity of copper at 20 °C	$\frac{1}{K}$
β	Volumetric thermal expansion coefficient	$\frac{1}{K}$
β_s	Empirical exponent for the calculation of sealing losses	1
δ	Length of air gap (in radial direction)	m
ϵ	Emissivity	1
ϵ_i	Emissivity; i = index	1
ζ_{conv}	Conversion factor	1
$\vec{\vartheta}$	Vector of average temperatures	°C
ϑ	Temperature	°C
ϑ_{be}	Mean bearing temperature	°C
$\vartheta_{cj,av}$	Average temperature of the cooling jacket	°C
$\vartheta_{fl,av}$	Average temperature of the coolant (fluid)	°C
ϑ_i	Temperature; i = index	°C
$\vartheta_{if,av}$	Average interface temperature	°C
ϑ_{in}	(Average) Coolant temperature at the inlet	°C
ϑ_{out}	Average coolant temperature at the outlet	°C
$\vec{\vartheta}_{rot}$	Measured rotor temperatures (vector)	°C

$\vec{\vartheta}_{\text{stat}}$	Measured temperatures of stationary machine parts (vector)	°C
λ	Thermal conductivity	$\frac{\text{W}}{\text{m K}}$
λ_{av}	Average thermal conductivity	$\frac{\text{W}}{\text{m K}}$
λ_{imp}	Thermal conductivity of impregnating resin	$\frac{\text{W}}{\text{m K}}$
μ_{b}	Constant coefficient of friction	1
μ_{r}	Relative magnetic permeability	1
ν	Kinematic viscosity	$\frac{\text{m}^2}{\text{s}}$
ρ	Volumetric mass density	$\frac{\text{kg}}{\text{m}^3}$
σ	Stefan-Boltzmann constant; $\sigma = 5.670 \cdot 10^{-8} \frac{\text{W}}{\text{m}^2\text{K}^4}$	$\frac{\text{W}}{\text{m}^2\text{K}^4}$
ς	Friction factor	1
ω	Angular frequency	$\frac{\text{rad}}{\text{s}}$

Chapter 1

Introduction

A concise description of the thermal modelling problem of electric machines can be found in C. Soderberg's paper *Steady Flow of Heat in Large Turbine-Generators* published back in 1931 [1]:

"*The predetermination of the temperature in electrical machines involves three distinct problems:*

1. *The magnitude and the distribution of the losses.*
2. *The flow of the cooling medium through the machine, and its cooling effect.*
3. *The flow of heat from the source of generation to the cooling medium.*"

Soderberg, who focussed on the third aspect in the cited paper, identified the challenges and key aspects of the thermal electric machine modelling more than eighty years ago. Despite fundamental developments in the fields of computer technology and electric machine and drive technology, such as the advance of computer-aided engineering and inverter-fed electric machines, the steps required when analysing the thermal behaviour still remain valid.

1.1 Scope of the thesis

The determination or prediction of losses in electric machines (being the first subproblem according to Soderberg) is a prerequisite for carrying out thermal analyses since the losses are the direct input for subsequent or coupled thermal calculations. More specifically, the spatial distribution of the losses highly affects the temperature distribution in the electric machine and, moreover, the losses themselves vary with temperature. Consequently, machine losses are an integral part of an overall thermal study and are thus covered in this work.

However, due to the complexity of the loss mechanisms in electric machines with some of them not even having been fully understood, losses are introduced and analysed with respect to the basic requirements for building and analysing thermal

models, i.e. the identification and approximation of the dominating loss sources.

The different loss mechanisms inside an electric machine—such as Joule heating in the machine windings and losses in the ferromagnetic material—cause spatial temperature differences within the components as well as between the machine components and lead to a temperature elevation of the machine with respect to its surrounding. In order to increase the utilisation of electric machines and to ensure that the thermal limits of the different machine components are not exceeded, a myriad of different cooling designs have been developed for the different machine types, their rating and application. The wide range of cooling systems, including free cooling, direct conductor cooling and cooling concepts with multiple cooling circuits, are classified in (ÖVE) EN standard 60034-6 [2]. This work's focus on three-phase water-jacket cooled electric machines in the power range of tens of kilowatts allows an in-depth analysis of one particular cooling system, yet—due to the presence of all three heat transfer phenomena, namely convection, conduction and radiation—the findings may be applied to all other concepts accordingly.

Moreover, it would neither be feasible nor possible to cover all types of electric machines. Therefore, machine types such as DC machines and slip-ring induction machines that are not the first choice in variable-speed application with high demands on torque and power density are not covered. Nonetheless, the concepts and methods may be applied to all machine types similarly.

An induction machine is used to validate the analytic and numerical models and to illustrate the use of the modelling approaches and tools. Nonetheless, the induction machine only serves as an exemplary case study. The key concepts are not specific to the presented induction machine but may be applied to different machine types. The modelling of random-wound machine windings, for instance, is by no means limited to the presented induction machine and the findings may be even used in the context of form-wound windings.

1.2 Outline of the thesis

A brief summary of the basic loss sources in electric machines is given in Section 1.3, including analytic and numerical methods to estimate their magnitudes.

The three heat transfer mechanisms that form the basis of the second and third of Soderberg's sub-problems are introduced in Sec. 1.4.

Finally, approaches to model and solve the resulting heat transfer problems by means of analytic and numerical methods are reviewed in Sec. 1.5.

Analytic and numerical thermal models are developed and analysed for the dif-

ferent machine components in Chapter 2. The parallel development permits to identify similarities in both modelling approaches, such as common underlying assumptions, as well as differences.

The process of developing complete thermal machine models is illustrated by an in-depth case study of an induction machine in Chapter 3, which comprises both the detailed analytic and numerical modelling as well as an experimental validation by actual measurements.

In addition to the conclusions, which are provided at the end of each main section and each chapter, general conclusions are provided in Chapter 4 and areas for further research are suggested.

1.3 Losses in electric machines

The calculation of losses in electric machines may be seen as one of the most challenging tasks in electric machine design [3] and, besides the different loss sources, even the manufacturing influences the machine losses [4, 5]. When determining the losses experimentally, the problem of accurately identifying the different losses remains. To take one example, IEC standard 60349-3 distinguishes between the following loss types [6]:

- No-load losses at the fundamental frequency:
  - ◇ Losses in the electric steel and other metal parts,
  - ◇ Frictional losses and windage losses (including integral fans);
- Load-dependent losses at the fundamental frequency:
  - ◇ Joule losses in the stator windings,
  - ◇ Joule losses in the rotor winding of induction machines,
  - ◇ Additional load losses in the electric steel and other parts as well as eddy current losses in the stator and rotor windings due to flux pulsations;
- Losses at all frequencies other than the fundamental frequency;
- Joule losses and brush contact losses in the excitation circuit of synchronous machines.

The classification of the machine losses and the standardised testing and calculation procedures defined in [6] allow a comparable experimental determination of the losses according to the defined loss categories. The fact that additional load losses in induction machines are defined to be 1 % of the equivalent 50 Hz rated input

power in this standard may illustrate the complexity of the loss phenomena present in electric machinery.

In the field of thermal modelling the aim is to estimate losses and, in particular, to link the losses to the corresponding machine components in a thermal model. Therefore, an equivalent loss classification that is partly based on [3, 7] is explained and subsequently used:

(i) **Copper losses**
Joule losses due to resistive heating in the stator and rotor windings (if applicable).

(ii) **Iron losses**
Losses in the ferromagnetic material of the magnetic circuit.

(iii) **Rotor losses**
Losses in the different rotor components, including eddy current losses in magnets and (additional) iron losses.

(iv) **Additional losses**
The so-called additional losses are a lumped description of electromagnetic losses in electric machines that occur in addition to the fundamental losses in the windings and in the ferromagnetic material.

(v) **Mechanical losses**
Frictional losses in the bearings and windage losses due to the movement of the inner air. Additional mechanical loss sources may include sealing losses or brush losses.

(vi) **Heat flux from or to adjacent components**
Heat flux from losses generated by adjacent components or heat flux to connected components that act as heat sinks.

1.3.1 Copper losses

Joule losses in the stator winding are caused by a current flow through the wires of the winding and they are proportional to the square of the current. For a symmetrical machine with m phases, the Joule losses $\overline{P}_{\text{Joule}}$ may be written as:

$$\overline{P}_{\text{Joule}} = m R_{\text{ph}} {I_{\text{phRMS}}}^2. \tag{1.1}$$

The phase resistance R_{ph} in Eq. (1.1) is not constant but temperature-dependent as the resistivity of copper significantly varies with temperature. Given the linear temperature coefficient $\alpha_{20,\text{Co}}$ of $3.9 \cdot 10^{-3}\,\text{K}^{-1}$ [8] and a constant current supply, the

resistance and thus the Joule losses increase by about 30 % when the temperature rises by 80 °C. Consequently, the temperature dependency of the losses must not be neglected, which, in consequence, leads to a coupled problem.

Machine types such as induction machines and separately excited synchronous machines feature a secondary winding in the rotor which causes additional Joule heating in the rotor that can be calculated accordingly. Yet, additional or increased losses due to the skin effect (in particular in the case of cage windings in induction machines) or due to brushes might have to be considered as well [7].

1.3.2 Iron losses

Both the stator and the rotor of electric machines typically consist of ferromagnetic electrical steel that presents a comparably low magnetic reluctance ($\mu_\mathrm{r} \gg 1$) allowing for the channelling of the magnetic fields and for a reduction in the magnetomotive forces (MMF) required for typical magnetic field strengths. The induced eddy currents are reduced by the stacking of thin steel sheets and further reductions are achieved by adding silicon, reducing the electrical conductivity, and by coating the sheets with an insulation [9, 10]. An overview of the numerous different iron loss models, which have been developed in the past—including the well-known *Steinmetz* model—may be found in [11]. One approach, which is partly used in the numerical and the analytic modelling of the iron losses in the case study, is derived in the following.

Under sinusoidal conditions, the eddy current losses per unit mass p_ec may be expressed in terms of the peak value of the magnetic field strength $\hat{B}$ and its frequency f as follows [7, 12]

$$p_\mathrm{ec} \propto \hat{B}^2 f^2. \tag{1.2}$$

Hysteresis losses, the second main iron loss phenomenon, are caused by the lossy change of the magnetisation in the ferromagnetic material, in particular due to the movement of the domain walls [9]. The energy needed for one cycle w_hyst is proportional to the area contained by the hysteresis curve (BH-curve), the losses are proportional to the product of the contained area and the frequency. Thus, the hysteresis losses per unit mass p_hyst are [7, 9, 12]

$$p_\mathrm{hyst} \propto w_\mathrm{hyst} f, \tag{1.3}$$

and, using an empirical correlation between w_hyst and $\hat{B}$, namely n_hyst, which is also referred to as *Steinmetz coefficient*, yields

$$p_\mathrm{hyst} \propto \hat{B}^{n_\mathrm{hyst}} f, \tag{1.4}$$

where $n_{\text{hyst}} \in [1.5, 2.5]$.

When n_{hyst} is chosen to be 2—as proposed in [3] for modern magnetic materials—the total iron losses per unit volume p_{iron} can be expressed as follows

$$p_{\text{iron}} = \left(k_{\text{ec}} f^2 + k_{\text{hyst}} f\right) \hat{B}^2. \tag{1.5}$$

The actual iron losses in an electric machine depend on multiple factors such as the thickness of the sheets and the material properties of the electrical steel, which are significantly influenced during machine manufacturing, i.e. the cutting and stacking of the sheets. The presence of higher harmonics further increases the iron losses. These aforementioned effects need to be accounted for in loss equations similar to Eq. (1.5). In practice, this is achieved by introducing one or more correction coefficients increasing the iron losses by 30 % to 70 % [3,7,12] compared with the reference values for losses or loss coefficients obtained from experimental tests of steel sheets under sinusoidal conditions, usually by means of Epstein frame tests.

The nomenclature of non-oriented electrical steel follows the classifications defined in applicable standards, such as EN 10106 [13] in Europe. *M400-64A*, for instance, refers to a fully-processed non-oriented electrical steel (no final annealing required; *M* for electrical steel, *A* for fully-processed) with a thickness of 0.64 mm (*64*) and maximum permissible specific losses of 4 $\frac{\text{W}}{\text{kg}}$ at 1.5 T and 50 Hz (*400*).

The factors k_{ec} and k_{hyst} in Eq. (1.5) are provided either directly by the steel sheet manufacturer or may be extracted from provided tabulated loss data or loss curves that state the losses at different magnetic flux densities and frequencies.

1.3.3 Rotor losses

Depending on the machine type, Joule losses, eddy current losses and iron losses may be present in the rotor. The Joule losses in separately-excited synchronous machines may be calculated similarly to Sec. 1.3.1 with additional losses being generated if brushes are used [7, 14]. In induction machines, the magnetic field rotates with a slip s at a frequency $f_2 = sf_1$ and, thus, the Joule and iron losses can generally be estimated according to Sec. 1.3.1 and Sec. 1.3.2. The resistance of the cage winding in the rotor is influenced by the slip as the skin effect leads to a reduction of the effective conductor height and thus to an increased resistance. The influence of the operating point on the resistance therefore needs to be accounted for in the calculation of Joule losses even though induction machines normally operate near synchronous speed, therefore limiting this effect. Additional iron losses in the rotor of induction machines are caused by reluctance variations due to the slotting of both rotor and stator. The slotting of the stator also leads to higher harmonics in the

MMF waveform causing further losses [3].

The rotor of permanent magnet (PM) machines is equipped with permanent magnets instead of windings, eliminating the Joule losses in the rotor. The fundamental frequency approaches presented in the preceding sections cannot be employed for the approximation of iron losses and eddy current losses since the rotor rotates synchronously under normal operating conditions. The causes of both loss sources in the rotor are similar to those of the above mentioned additional loss phenomena in induction machines [15]. Those additional losses phenomena are generally difficult to approximate and analytic approaches are specific to certain machine types (e.g. magnet losses in surface-mounted PM machines [16]). A more general method for the calculations is the finite element method (FEM) that might be employed as an alternative [17].

1.3.4 Additional losses

The additional losses are electromagnetic losses which occur in addition to the fundamental losses in the windings and in the ferromagnetic material. Comprehensive overviews of the so-called stray (no-load and load) losses in induction machines and synchronous machines may be found in [14, 18, 19]. Additional losses include losses induced by the slotting of stator and rotor (Sec. 1.3.3) but also losses due to effects in the end region of the machine as well as losses due to the high-frequency switching in modern inverter-fed machines. Cutting or punching of the steel sheet and mechanical stress may lead to a deterioration of the steel sheet, increasing the iron losses and thus being a further contributor to the overall additional losses.

Since additional losses are difficult to calculate, factors for different machine types are frequently used to estimate additional losses in terms of the input power [3, 6, 7, 12]. In the context of thermal machine simulations, the approximated additional losses are then to be assigned to the corresponding machine parts where the losses are generated (typically also by factors) [3, 20].

1.3.5 Mechanical losses

The rotation of the rotor causes **frictional losses** in the machine bearings and, if applicable, in sealing rings. Additional frictional losses are generated in the air that are commonly referred to as windage losses.

Losses in bearings depend on multiple factors such as the bearing type, the bearing load, the rotational speed and tribological aspects, including properties of the lubricant (e.g. its chemical composition and its temperature) and bearing wear [21, 22].

(Non-ideal) bearing fitting might affect the losses and lead to deviations from calculated loss values (Eq. (1.6)–(1.9)) [22]. The accuracy of bearing loss calculations therefore generally depends on the availability of detailed bearing and assembly data.

Methods for calculating the frictional losses range from dynamic bearing simulations [23] to simplified models used in standards, including ISO 15312 [24], that distinguish between load-dependent frictional losses and speed-dependent frictional losses. The latter approach suffices in the context of thermal electric machine modelling as the transient bearing behaviour is not required and using coefficients that are provided by the bearing manufactures for different bearing types and under normal operating conditions allows for sufficient estimates.

The speed-dependent frictional torque M_0 (in N m) may be defined as [22, 25]

$$M_0 = \begin{cases} 1.53 \cdot 10^4 \, f_{0\mathrm{b}} \, (\nu \cdot n)^{\frac{2}{3}} \, \overline{d}_{\mathrm{b}}{}^3 & \text{if } \nu \cdot n \geq \frac{100}{3} \cdot 10^{-6} \frac{\mathrm{m}^2}{\mathrm{s}^2} \\ 16 \, f_{0\mathrm{b}} \, \overline{d}_{\mathrm{b}}{}^3 & \text{if } \nu \cdot n < \frac{100}{3} \cdot 10^{-6} \frac{\mathrm{m}^2}{\mathrm{s}^2} \end{cases}, \tag{1.6}$$

where

ν kinematic viscosity,
n rotational speed,
$f_{0\mathrm{b}}$ coefficient for the speed-dependent frictional torque,
$\overline{d}_{\mathrm{b}}$ mean bearing diameter.

The load-dependent frictional torque M_1 is given by

$$M_1 = 1000 \, f_{1\mathrm{b}} \, P_{1\mathrm{b}} \, \overline{d}_{\mathrm{b}}, \tag{1.7}$$

where

$f_{1\mathrm{b}}$ coefficient for the load-dependent frictional torque,
$P_{1\mathrm{b}}$ bearing load (the calculation of the relevant bearing load for different bearing types is explained in [22, 25]).

If bearings with sealings are used, losses also occur due to friction in the sealings. The additional torque caused by sealings M_{seal} is given by [21]

$$M_{\mathrm{seal}} = 10^{-3} \left[k_{\mathrm{s1}} \left(10^3 d_{\mathrm{s}} \right)^{\beta_{\mathrm{s}}} + k_{\mathrm{s2}} \right], \tag{1.8}$$

where

k_{s1} first empirical factor for the calculation of sealing losses,
k_{s2} second empirical factor for the calculation of sealing losses,
d_{s} seal counterface diameter,
β_{s} empirical exponent for the calculation of sealing losses.

The factors k_{s1}, k_{s2} and the exponent β_s are specific to certain sealing types and also depend on the bearing size and type. Values corresponding to the bearing and sealing size and types may be found in form of tabulations [21].

Alternatively, bearing manufactures also provide constant coefficients of friction (μ_b) for different bearing types under operation conditions deemed normal. Rough estimated of the bearing torque due to friction M_b may then be estimated as follows (assuming the bearing load to be equal to 10 % of the basic dynamic load rating $C_{b,dyn}$ and with d_b being the bore diameter) [21, 22]

$$M_b = 5 \cdot 10^{-2} C_{b,dyn}\, \mu_b\, d_b. \tag{1.9}$$

Windage losses in electric machines are the result of the frictional forces acting on the inner air due to the relative movement of the rotor and the stator. The loss magnitude is therefore influenced by the rotational speed of the rotor, the properties of the surrounding gas (which are generally temperature-dependent) and all surfaces that are in contact with the air.

A simple equation allowing to estimate the sum of both, the frictional losses in the bearings and the complex windage losses, is provided in [14]. The presented equation shows that the combined frictional and windage losses are approximately proportional to the square of the rotational speed, which is confirmed in [3]. [14] also lists typical factors for frictional and windage losses for different machine types, including factors for machines with hydrogen cooling or with rotor-mounted fans. The fact that the different exponent in the case of a mounted fan (cubic relationship) is implicitly considered in an adjusted value for the coefficient in the quadratic equation in [14] indicates that the equation is not generally applicable to all machine types or non-standard machines.

The windage losses P_{wi} are frequently computed with the following equation (e.g. [26])

$$P_{wi} = c_{fr}\, \rho\, \pi\, \omega^3\, {r_{r,o}}^4\, l_r, \tag{1.10}$$

where

c_{fr}	friction coefficient,
ρ	volumetric mass density (of air),
ω	angular velocity,
$r_{r,o}$	outer radius of the rotor,
l_r	rotor length.

A roughness coefficient k_{rou} (ranging between 1 for smooth surfaces and 1.4 [7]) is added to Eq. (1.10) in [27].

Numerous experimental tests and theoretical studies of rotating concentric cylinders, including the effect of slotting, have been carried out since the early tests by Taylor [28] and estimates of the friction coefficient c_{fr} in terms of the Reynolds number Re have been developed.

The Reynolds number for tangential flow in the air gap of an electic machine is calculated with [7, 29]

$$Re = \frac{\omega \, r_{\mathrm{r,o}} \, \delta}{\nu}, \tag{1.11}$$

where

δ length of air gap (in radial direction),
ν kinematic viscosity (of air).

The windage losses may then be calculated with empirically determined functions that approximate c_{fr} ([27, 29]).

It should be noted, however, that c_{fr} depends on the angular velocity and the windage losses are thus not generally proportional to ω^3 as Eq. (1.10) might suggest.

1.3.6 Heat flux from or to adjacent components

Additional loss sources, such as integrated power electronics or a gear set which is directly connected to the electric machine, might influence the temperature of the electric machine. Therefore, such losses might need to be included in thermal models by heat injections if they have a significant influence on the thermal behaviour. Comparably small heat injections into the rotor could, for instance, have a notable influence on the rotor temperature. Furthermore, the temperature of the coolant might vary depending on ambient conditions or other components that are cooled simultaneously. A possibly higher coolant temperature would then lead to an increased temperature level in the machine, possibly requiring consideration when predicting the temperatures in the machine.

Adjacent components may also act as heat sinks. The contacting surface between an electric machine and a test bench may, for instance, present an additional heat flow path to the typically cooler surrounding. This may affect the thermal behaviour and consequently lead to deviations between the test set-up and standard operating conditions (e.g. asymmetrical temperature distributions). In such cases, particular attention is required when verifying thermal models by experimental tests.

1.4 Heat transfer in electric machines

The modelling of heat transfer in electric machines is complex as it comprises the analysis of heat conduction through complex materials in multiple directions with unevenly distributed internally generated losses (for instance iron losses in the stator stack), as well as the analysis of convective heat transfer and radiation.

1.4.1 Conductive heat transfer

Heat conduction, which is a complex heat transfer mechanism on a microscopic scale at an atomic or molecular level, is defined phenomenologically on a macroscopic level. The local heat flux density $\vec{q}$, caused by a temperature gradient, is computed with the thermal conductivity λ and the temperature T by *Fourier's law* [30]

$$\vec{q} = -\lambda \nabla T. \tag{1.12}$$

The heat equation, derived from the energy balance of a differential control volume and Eq. (1.12), is in Cartesian coordinates (x,y,z) [30]

$$\frac{\partial}{\partial x}\left(\lambda \frac{\partial T}{\partial x}\right) + \frac{\partial}{\partial y}\left(\lambda \frac{\partial T}{\partial y}\right) + \frac{\partial}{\partial z}\left(\lambda \frac{\partial T}{\partial z}\right) + \dot{q} = \rho\, c_\mathrm{p} \frac{\partial T}{\partial t}, \tag{1.13}$$

where

λ	thermal conductivity (a tensor in the case of anisotropic materials),
T	temperature,
$\dot{q}$	heat generation rate per unit volume,
ρ	volumetric mass density,
c_p	specific heat at constant pressure,
t	time.

The heat equation in cylindrical coordinates (r,φ,z) is [30]

$$\frac{1}{r}\frac{\partial}{\partial r}\left(\lambda\, r \frac{\partial T}{\partial r}\right) + \frac{1}{r^2}\frac{\partial}{\partial \varphi}\left(\lambda \frac{\partial T}{\partial \varphi}\right) + \frac{\partial}{\partial z}\left(\lambda \frac{\partial T}{\partial z}\right) + \dot{q} = \rho\, c_\mathrm{p} \frac{\partial T}{\partial t}. \tag{1.14}$$

Eq. (1.13) and Eq. (1.14) allow the calculation of the temperature distribution in bodies, including the effect of internal heat generation and also transient heat conduction.

Assuming a constant uniform thermal conductivity $\lambda = const$ and stationary conditions $\frac{\partial T}{\partial t} = 0$, Eqs. (1.13) and (1.14) reduce to

$$\nabla^2 T + \frac{\dot{q}}{\lambda} = 0. \tag{1.15}$$

Integrating the heat equation yields the temperature distribution. To give an example, the temperature distribution in a hollow cylinder without internal heat generation is found by integrating Eq. (1.14), neglecting the partial derivatives with respect to φ and z and with setting $\dot{q} = 0$.

With the temperature of the inner surface of the hollow cylinder $T(r_1) = T_1$ and the temperature of the outer surface of the hollow cylinder $T(r_2) = T_2$, the temperature at the radial position r in the cylinder is given by

$$T(r) = T_1 + \frac{T_1 - T_2}{\ln(\frac{r_1}{r_2})} \ln(\frac{r}{r_1}) = T_2 + \frac{T_1 - T_2}{\ln(\frac{r_1}{r_2})} \ln(\frac{r}{r_2}). \tag{1.16}$$

(The temperature profile inside hollow cylinders is illustrated in Fig. 1.2, including the effect of interface gaps (Sec. 1.4.4).)

The heat flow rate $\dot{Q}$ across the hollow cylinder with the length l_{cyl} is

$$\dot{Q}(r) = \dot{Q} = 2\pi\, l_{\mathrm{cyl}}\, r \left(-\lambda \frac{(T_1 - T_2)}{\ln(\frac{r_1}{r_2})} \frac{1}{r} \right) = \underbrace{\frac{2\pi\, l_{\mathrm{cyl}}\, \lambda}{\ln(\frac{r_2}{r_1})}}_{1/R_{\mathrm{th,cond}}} (T_1 - T_2). \tag{1.17}$$

Similarly to an electrical resistance, a thermal resistance (due to conduction) $R_{\mathrm{th,cond}}$ can be defined in terms of the temperature difference between both terminals of the thermal resistance ΔT and the heat flow rate $\dot{Q}$ across it, as indicated in Eq. (1.17).

$$R_{\mathrm{th,cond}} = \frac{\Delta T}{\dot{Q}} \tag{1.18}$$

The thermal resistances of other basic geometries, such as plane walls and spheres, are computed similarly by combining Fourier's law and the heat equation.

1.4.2 Convective heat transfer

Convective heat transfer is the sum of heat transfer by diffusion (microscopic molecular motion) and advection (bulk motion of fluids). The convective heat transfer is referred to as forced convection if the movement of the fluid is caused by an external force (e.g. when a coolant is pumped through cooling channels) and as natural convection if the motion is caused by buoyancy forces due to density gradients (e.g. due to the induced movement of air in the vicinity of a hot plate) [31].

The concept of boundary layers introduced by Prandtl [32] is illustrated in Fig. 1.1 by a flat heated plate (at temperature T_{p}) that is immersed in a uniform flow with a free-stream velocity u_∞. The fluid flow is divided into the flow in the boundary layer where viscous forces act that eventually reduce the velocity of the fluid to zero at the boundary and the flow beyond the boundary layer where viscous forces

are negligible. Similarly to the velocity boundary, a temperature boundary may be defined with the free-stream temperature T_∞ of the fluid and the temperature T_p at the boundary. The link between the velocity boundary layer and the temperature boundary layer is given by the dimensionless Prandtl number Pr [30,31,33]

$$Pr = \frac{\nu}{\lambda/\rho c_\mathrm{p}}, \tag{1.19}$$

which is a function of the kinematic viscosity ν, the thermal conductivity λ, the density ρ, and the specific heat c_p.

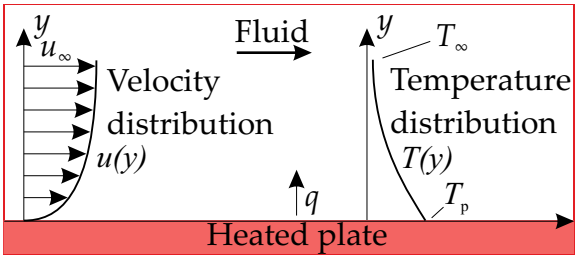

Figure 1.1: Illustration of the velocity and the temperature boundary layer, adapted from [30,31].

The heat transfer by convection can be expressed conveniently by a (local) heat transfer coefficient h that depends on the properties of the fluid (such as its temperature, thermal conductivity and viscosity), the surface geometry and the fluid motion [33].

$$q = h\left(T_\mathrm{p} - T_\infty\right) \tag{1.20}$$

Using the average heat transfer coefficient $\bar{h}$ for an entire surface of area A [33]

$$\bar{h} = \frac{1}{A}\int_A h\, dA, \tag{1.21}$$

the overall heat transfer rate $\dot{Q}$ is calculated with

$$\dot{Q} = \underbrace{\bar{h}\, A}_{1/R_\mathrm{th,conv}}\left(T_\mathrm{p} - T_\infty\right). \tag{1.22}$$

A thermal resistance due to conduction $R_\mathrm{th,conv}$ may be defined similarly to the thermal resistance due to conduction, as indicated in Eq. (1.22).

Functional relationships in terms of dimensionless numbers are commonly used to determine the (average) convective heat transfer coefficient of flow problems. Such typically empirical relations for common problems are available in the literature, e.g. in [31,34].

Correlations for the heat transfer coefficients for forced convection (present in cooling jackets and the inner air volume due to the movement of the rotor) are typically given by correlations between the Nusselt number (Nu), the Prandtl number (Pr) (Eq. (1.19)) and the Reynolds number (Re): $Nu = f(Pr, Re)$ [34,35].

The Reynolds number is a measure of the ratio between inertia forces and viscous forces and is given by (L: characteristic length) [30,31,33,35]

$$Re = \frac{v\,L}{\nu}. \tag{1.23}$$

The Nusselt number, which is the ratio between convective heat transfer to (assumed merely) conductive heat transfer, is [30,31,33,35]

$$Nu = \frac{h\,L}{\lambda}. \tag{1.24}$$

Consequently, if a value for Nu is obtained from a correlation, the corresponding (average) heat transfer coefficient and thus the equivalent thermal resistance can be computed with Eq. (1.24).

1.4.3 Radiative heat transfer

Matter above absolute zero emits energy by radiation and, in contrast to conduction and convection, the transfer of heat by radiation does not require a medium. The Stefan-Boltzmann law gives the rate of energy radiation per unit surface area E_{rad} in terms of the emissivity ϵ of a body, its temperature T and the Stefan-Boltzmann constant σ [30,31,33]

$$E_{\text{rad}} = \epsilon\,\sigma\,T^4. \tag{1.25}$$

Generally, mater not only emits energy by radiation but may also absorb, reflect or transmit radiation. Calculating the effective heat transfer between the different parts of an assembly is therefore a complex task. Yet, in many cases, this task may be approximated by the simplified case of radiation heat exchange between two surfaces that are separated by a non-participating medium (this assumption is typically valid for gases [30]). The heat transfer rate by radiation $\dot{Q}$ then depends on the temperatures T_1 and T_2 of surfaces 1 and 2, their emissivities ϵ_1 and ϵ_2, their surface areas A_1 and A_2 and the shape factor F_{12}, which is obtained from the geometric analysis of the position and the orientation of the parts of the assembly [30,33]

$$\dot{Q} = \frac{\sigma\left({T_1}^4 - {T_2}^4\right)}{\frac{1-\epsilon_1}{\epsilon_1 A_1} + \frac{1}{A_1 F_{12}} + \frac{1-\epsilon_2}{\epsilon_2 A_2}}. \tag{1.26}$$

A thermal resistance due to radiation $R_{\text{th,rad}}$ may be defined similarly to $R_{\text{th,conv}}$ in Eq. (1.22). For example, the heat transferred by radiation from a small object with the surface area A_1 at the temperature T_1 to a much larger surrounding body (such that $A_1/A_2 \approx 0$) at T_2 is (using Eq. (1.26))

$$\dot{Q} = \underbrace{\sigma \epsilon_1 \frac{({T_1}^4 - {T_2}^4)}{(T_1 - T_2)} A_1}_{h A_1 = 1/R_{\text{th,rad}}} (T_1 - T_2). \tag{1.27}$$

It follows from Eq. (1.27) that h and $R_{\text{th,rad}}$ are by no means constant but highly depend on the temperature and it is therefore essential to pay particular attention to the temperature dependency of $R_{\text{th,rad}}$ when integrating it into a lumped parameter model.

1.4.4 Interface gaps

Asperity contacts between (rough) surfaces lead to a temperature drop at the interface due to microscopic gaps that increase the effective thermal resistance (Fig. 1.2). The extent of the temperature drop depends on the material properties of both surfaces, in particular the surface roughness, the interfacial medium and the pressure in the contact region.

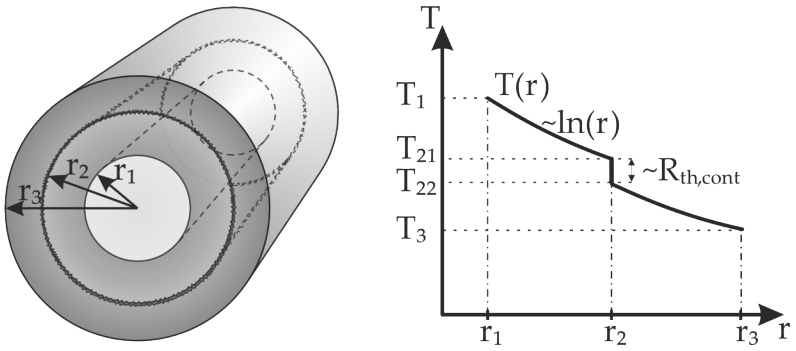

Figure 1.2: Illustration of the temperature profile inside two contacting hollow cylinders with a rough interface.

Typical ranges of thermal interface conductances can be found in the literature for various materials, contact pressures, surface roughnesses and interfacial fluids [30, 31, 35]. The thermal contact resistance $R_{\text{th,cont}}$ is given in terms of the thermal interface conductance h_{intf} and the contact area A

$$R_{\text{th,cont}} = \frac{1}{h_{\text{intf}} A}. \tag{1.28}$$

It may be noted that the thermal interface conductance h_{intf} in Eq. (1.28) ($[h_{\text{intf}}] = \frac{\text{W}}{\text{m}^2\,\text{K}}$) is, strictly speaking, not a thermal conductance (i.e. the property of a body

or cavity to conduct heat or the inverse of the thermal resistance) but it may be regarded as a thermal contact conductance coefficient (a measure of the thermal conductance between the contacting bodies per contact area) or as the ratio between the thermal conductivity and the layer thickness of a homogeneous material in the interface gap.

1.5 Modelling of heat transfer in electric machines

Heat transfer in the context of electric machinery may be modelled by analytic or numerical methods. In analytic approaches, simplifications are employed to reduce the complexity of heat transfer to a problem or sub-problems that can be solved analytically. In numerical approaches, the governing heat transfer equation is solved numerically for a discrete representation of the geometry.

1.5.1 Stationary lumped parameter modelling

Lumped thermal resistances offer a simple, yet (ideally) exactly equivalent, description of the thermal behaviour of the modelled components with respect to their boundaries. To give an example, Fig. 1.3 shows the equivalent thermal lumped parameter model of the contacting hollow cylinders in Fig. 1.2. $R_{\mathrm{th},1}$ and $R_{\mathrm{th},3}$ denote the thermal resistances of the inner and of the outer cylinder respectively, $R_{\mathrm{th},2}$ models the contact resistance between both cylinders.

The thermal behaviour of the assembly between the inner surface of the inner hollow cylinder and the outer surface of the outer hollow cylinder in Fig. 1.2 (nodes 1 and 3 in Fig. 1.3) may be modelled equivalently by one combined thermal resistance, which is, in this case, simply the sum of $R_{\mathrm{th},1}$, $R_{\mathrm{th},2}$ and $R_{\mathrm{th},3}$.

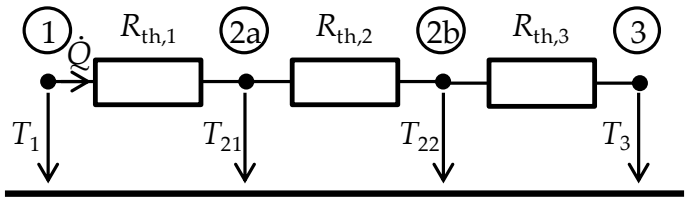

Figure 1.3: Equivalent thermal lumped parameter network of the contacting hollow cylinders in Fig. 1.2.

It is apparent that the overall lumped parameter model of both hollow cylinders and the contact resistance at the interface does not give the spatial temperature distribution within the elements (as provided in Fig. 1.2) but it provides an equivalent

model that correctly calculates the temperatures at the connectors corresponding to a heat flow rate $\dot{Q}$ across the assembly. (The thermal resistances in Fig. 1.3 are calculated with Eqs. (1.17) and (1.28).)

By combining the thermal resistances of different machine parts, thermal lumped parameter models of parts of electric machines or the complete assembly may be built. A frequently cited thermal lumped parameter model of an induction machine is given in Fig. 1.4.

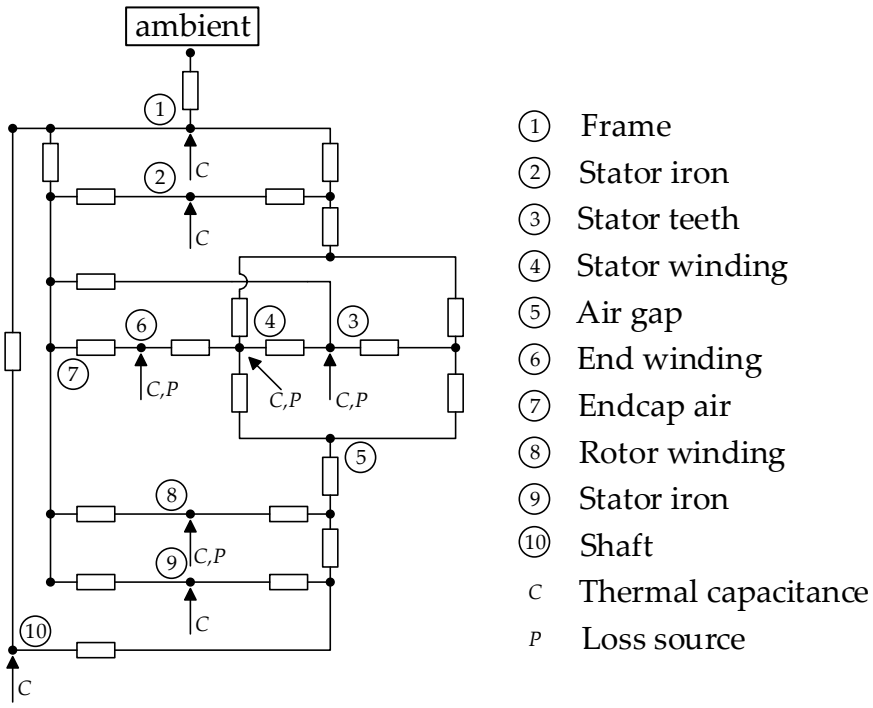

Figure 1.4: Thermal lumped parameter network of an induction machine [36].

1.5.2 Transient lumped parameter modelling

The transient thermal lumped parameter modelling requires the consideration of the heat capacity of the machine components (amongst other effects such as temperature-dependent material properties), e.g. the term $\rho\, c_\mathrm{p} \frac{\partial T}{\partial t}$ in Eq. (1.13).

In the frame of lumped parameter studies, lumped capacitances are used to approximate the transient behaviour of the components in the electric machine. Depending on the number of nodes in the lumped parameter model, the stator stack, for instance, may be modelled by two lumped capacitances, one for the yoke and one the teeth, or one combined lumped capacitance.

The underlying assumption of the lumped capacitance concept is a spatially uniform temperature in the corresponding solid. This assumption, in turn, is identical

with the assumption that there is no heat transfer in the solid (Eq. (1.12)). As soon as heat is transferred, this assumption does not hold and temperature gradients occur that, for example, lead to a temperature profile such as the one given in Fig. 1.2 for cylindrical systems.

A measure for the accuracy of the assumption of an approximately uniform internal temperature in a body is provided by the dimensionless Biot number Bi, which is defined as [30, 37]

$$Bi = \frac{L\,h}{\lambda}, \tag{1.29}$$

where

L	characteristic length (e.g. ratio volume of body / surface area of body),
h	(average) heat transfer coefficient at the surface of the body,
λ	thermal conductivity of the body.

Bi may consequently be regarded as the ratio between the thermal resistance inside the body and the resistance at the surface (interface) to the environment. At Biot numbers well below 1 (according to [33], results are expected to lie within around 5 % if $Bi = 0.1$), the temperature distribution inside the body is expected to be approximately uniform as the internal resistance is negligible compared with the resistance to the environment.

Given the temperature distribution is uniform ($Bi \ll 1$), the body's transient thermal behaviour may consequently be modelled by one thermal capacitance C_{th}, which is given by

$$C_{\mathrm{th}} = \rho\, V\, c_{\mathrm{p}}, \tag{1.30}$$

where

C_{th}	thermal capacitance of the body,
ρ	volumetric mass density of the body,
V	volume of the body,
c_{p}	specific heat of the body.

The fact that C_{th} may actually be modelled in a thermal lumped parameter similarly to a capacitance in an electric lumped parameter model is illustrated by the cooling down of the body, which is at the initial temperature T_0 at $t = 0$ ($T(0) = T_0$). h is the heat transfer coefficient at the interface (surface area A) of the body to the ambient at the temperature T_∞.

The following is then valid for the temperature of the body $T(t)$ [33, 37]

$$-h\,A\,[T(t) - T_\infty] = C_{\mathrm{th}} \frac{dT(t)}{dt}. \tag{1.31}$$

The solution for $T(t)$ is [33, 37]

$$T(t) = T_\infty + (T_0 - T_\infty)\, e^{-\frac{h\,A}{C_{\text{th}}}t}. \tag{1.32}$$

Eq. (1.32) describes an exponential cooling down, which is equivalent to the discharging of an electric capacitance.

As certain temperature differences exist in each body, the required single component temperature in the lumped capacitance approach is modelled by the average component temperature. The lumped resistance approach and the lumped capacitance approach are then simply combined by connecting the lumped capacitance to the node that gives the average temperature of the modelled component. Examples of transient lumped parameter models may, for instance, be found in [3, 36, 38].

A simple example is provided in Fig. 1.5, which shows the transient lumped parameter model of a single component with the thermal resistance $R_{\text{th}} = R_{\text{th},1} + R_{\text{th},2}$.

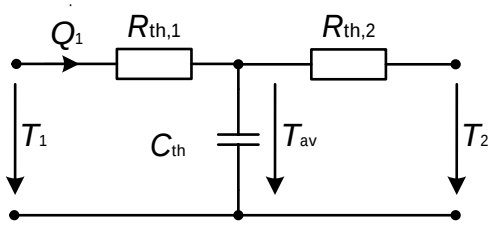

Figure 1.5: Simple transient lumped parameter model.

In the steady state, the average temperature is

$$T_{\text{av}} = T_1 - \frac{R_{\text{th},1}}{R_{\text{th},1} + R_{\text{th},2}}\,(T_1 - T_2) = T_1 - \frac{R_{\text{th},1}}{R_{\text{th}}}\,(T_1 - T_2)\,. \tag{1.33}$$

The thermal capacitance C_{th} of the component is connected to the node which gives the average temperature. R_{th} is, however, not generally split into two identical subresistances $R_{\text{th},1}$ and $R_{\text{th},2}$.

The elements of the lumped parameter model may be derived from the analytic solution for the temperature profile inside the component (Sec. 1.4.1). Based on this temperature profile, the equation for the average temperature may be determined (integration over the temperature profile) and the elements of the lumped parameter model may finally be found by merging the analytic equation for the average temperature and the corresponding relationship according to the lumped parameter model.

1.5.3 Modelling of loss sources

In lumped parameter models, losses are modelled by discrete loss injections, the thermal equivalent of electric current sources. In elements such as the machine

windings and the ferromagnetic stator stack, losses are generated inside the elements. This consequently leads to thermal problems of heat conduction with internal heat generation.

If the geometry is not complex and if the heat generation rate $\dot{q}$ is spatially uniform, an analytic solution to Eq. (1.15) may be found which allows to derive an analytically accurate equivalent lumped parameter model (Fig. 1.6(a)).

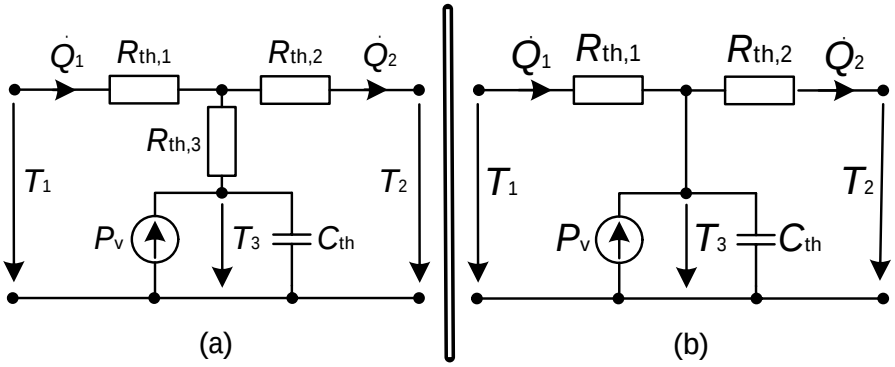

Figure 1.6: Equivalent transient lumped parameter model (typically derived for non-complex geometries with spatially uniform internal heat generation) (a) and simplified transient lumped parameter model with internal loss injection (b).

The computation of the temperature profiles in one-dimensional plane wall-like as well as in radial systems with spatially uniform internal heat generation is explained in [30, 33, 35], which is the first step to derive the parameters of the equivalent lumped parameter model.

The calculation of the average temperature and the determination of $R_{th,1}$, $R_{th,2}$ and $R_{th,3}$ by solving Eq. (1.15) (including the spatially uniform internal heat generation) and by comparing the results with the lumped parameter model in Fig. 1.6(a)) is carried out in the appendix of [38] for axial and radial heat flow though cylindrical elements. The results for straight heat flow problems may be derived from the axial flow in cylindrical systems or the resulting equations may be taken directly from [3, 7].

$R_{th,3}$ in Fig. 1.6 has a negative value, which can be verified by deriving the average temperature for a simple plane wall with spatially uniform internal heat generation, yielding that in this case: $R_{th,3} = -\frac{1}{3}R_{th,1} = -\frac{1}{3}R_{th,2}$. The result is confirmed in [38], where cylindrical problems are analysed.

The negative resistances may be regarded as mathematical corrections that compensate the error which is introduced by modelling the internal losses by a concentrated loss source.

It may be noted that the model in Fig. 1.6(a) is an accurate equivalent lumped parameter description only if an analytic solution for the average component temperature can be found and incorporated into the lumped parameter model (only possible for non-complex geometries and non-complex internal loss generation). If the heat generation is not spatially uniform or if the geometry of the body is more complex, analytic solutions may generally not be found and exactly equivalent lumped parameter models may therefore not be built. In such cases, the simpler (generally approximate) model given in Fig. 1.6(b) may as well be used, in which the overall thermal resistance is simply split into two sub-resistances without an additional third sub-resistance.

1.5.4 Multi-dimensional analytic modelling

Heat transfer has been treated as being confined to one dimension so far. Multi-dimensional heat transfer problems generally require solving Eq. (1.13). Exact analytic solutions of heat transfer problems between simple geometries with two distinct temperatures (at the boundaries) have already been derived in the literature and are given in terms of a shape factor S ($[S] = \mathrm{m}$). The heat $\dot{Q}$ transferred between the two temperatures T_1 and T_2 in the assembly is [30, 31, 33, 35]

$$\dot{Q} = \lambda S \left(T_1 - T_2\right). \tag{1.34}$$

It is evident from Fig. 1.4 that the concept of shape factors cannot simply be employed to model multi-dimensional heat transfer in the frame of lumped parameter studies of electric machines. Mathematically, the temperatures of most nodes depend on the temperatures of more than one neighbouring node. The shape factor concept reduces multi-dimensional problems to a heat transfer problem between two distinct temperatures. Consequently, heat transfer in axial and radial direction in a hollow cylinder, which is as a function of the temperatures of all four surfaces, cannot be modelled with a shape factor but would actually require solving Eq. (1.13) with the corresponding boundary conditions.

As analytic solutions of multi-dimensional problems for assemblies consisting of complex shapes and components are difficult (if not impossible) to determine, multi-dimensional heat transfer is almost always treated as the superposition of one-dimensional heat transfer in lumped parameter studies of electric machines. The superposition of the transient one-dimensional lumped parameter model of Fig. 1.6(a) is given in Fig. 1.7(a). T_a and T_b denote the temperatures in the first dimension , T_α and T_β denote the temperatures in the second dimension. In the case of a hollow cylinder, T_a and T_b may be defined as the temperatures at both ends of the cylinder

(axial direction) and T_α and T_β as the temperatures of the inner and the outer surface of the hollow cylinder (radial direction).

The model in Fig. 1.7(a) is the combination of the model in Fig. 1.6(a) to model heat flow in two, ideally independent, directions. It may, at the same time, be regarded as only an approximate model because it is based on the assumptions of uniform internally generated losses, independent heat flow in both directions and the model implies that the single mean temperature defines the heat flow in both directions.

Particularly if one or more of the above stated assumptions are apparently not fulfilled and e.g. analytical solutions cannot be found for the one-dimensional heat paths (which are treated independently), the even simpler model in Fig. 1.7(b) may be used in the frame of generally approximate lumped parameter studies. In such cases, a straightforward choice for the model parameters, which does not require significant computational effort, may be splitting the thermal resistance in each direction into equal sub-resistances ($R_{\text{th},7} = R_{\text{th},8}$ and $R_{\text{th},9} = R_{\text{th},10}$) and modelling the losses as a point loss source and connecting the loss source and the thermal capacitance to the mid-point. However, the validity of such the simplification may need to be verified.

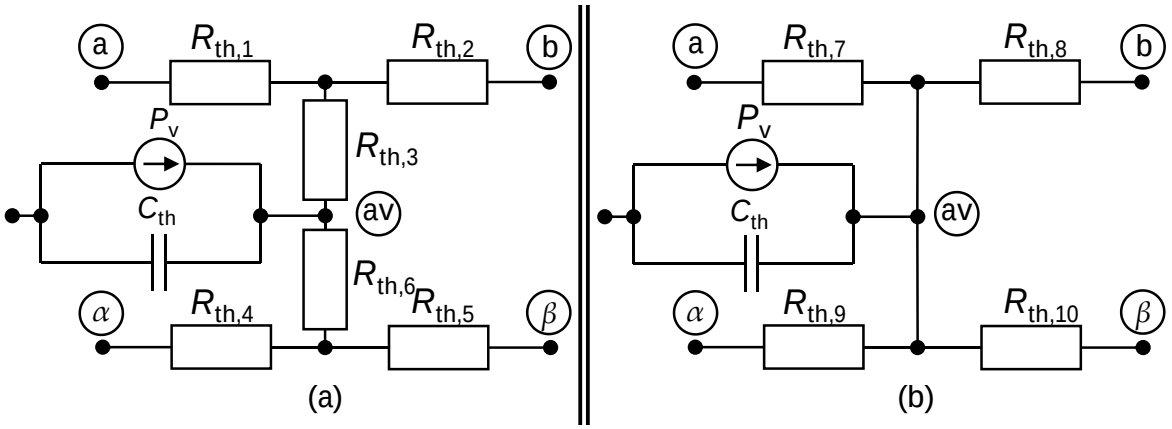

Figure 1.7: Two-dimensional lumped parameter models based on the one-dimensional models in Fig. 1.6.

The difference between the analytic solution of a two-dimensional heat transfer problem and its simplified lumped modelling is analysed for a flat plate (rectangle) in [1] and a sufficient accuracy for practical purposes is confirmed. However, the exact quantification of the error introduced by superposing heat transfer is difficult to determine as it would require knowing the exact solution. In simple cases, experimental set-ups or the comparison with numerical simulations might be an option.

The exact solution of a straight two-dimensional heat transfer problem and the equivalent two-dimensional lumped parameter model (not only a superposed one-

dimensional model) is derived in [7].

1.5.5 Numerical modelling of heat transfer

In numerical approaches, the heat transfer equations are not solved analytically but the component or the assembly is converted into a discrete (meshed) representation and the equations are subsequently solved numerically.

In this work the CFD software package STAR-CCM+ [39] is used to simulate heat transfer. The software uses the finite volume method (FVM), which is typically used in computational fluid dynamics. In the finite volume method, the governing continuous conservation equations (conservation of momentum, mass and energy) are applied to small discrete volumes (control volumes). Therefore, the continuous space (the three-dimensional model) is discretised and the conservation equations are solved for each control volume [39–41]. STAR-CCM+ offers several different meshing modules which, amongst others, allow to automatically generate tetrahedral and polyhedral grids or to manually discretise surfaces and extrude the 2D grid to generate a 3D grid. Different solver modules in STAR-CCM+ allow to simulate the motion of fluids (liquids and gases) and to couple mass transfer and heat transfer [39].

To exemplify the required steps for simulating heat transfer numerically, the **conductive heat transfer** problem in Fig. 1.8 is solved numerically. First, a CAD model of the contacting cylinders is created with $r_1 = 0.05\,\mathrm{m}$, $r_2 = 0.08\,\mathrm{m}$, $r_3 = 0.12\,\mathrm{m}$, $l_{\mathrm{cyl}} = 0.5\,\mathrm{m}$. The parameters $\lambda = 130\,\frac{\mathrm{W}}{\mathrm{m\,K}}$ and $h_{\mathrm{intf}} = 2 \cdot 10^4\,\frac{\mathrm{W}}{\mathrm{m^2\,K}}$ are set and the following boundary conditions are assigned to the inner surface of the inner cylinder and the outer surface of the outer cylinder (all other surfaces are adiabatic boundaries): $\dot{Q} = 8540\,\mathrm{W}$ and $\vartheta(r_3) = \vartheta_3 = 20\,^{\circ}\mathrm{C}$ (Fig. 1.8(a)).

The geometry is converted into a meshed representation that is shown in the close-up in Fig. 1.8(d) and the heat equation is solved for these discrete elements. Following Eq. (1.17), (1.18) and (1.28), the temperature of the inner surface of the inner cylinder $\vartheta(r_1)$ is (for reference)

$$\vartheta(r_1) = \vartheta_3 + \frac{\dot{Q}}{2\pi\, l_{\mathrm{cyl}}} \left(\frac{\ln(\frac{r_3}{r_1})}{\lambda} + \frac{1}{h_{\mathrm{intf}}\, r_2} \right) = 40\,^{\circ}\mathrm{C}. \tag{1.35}$$

The results of the numerical simulation are shown in Fig. 1.8(c) and the temperature profile in radial direction is given in Fig. 1.8(b). The fact that the temperature is calculated for each discrete element may be seen in Fig. 1.8(b), where every square corresponds to the result of one of the elements along the x-axis (indicated by a thin white line) in Fig. 1.8(d).

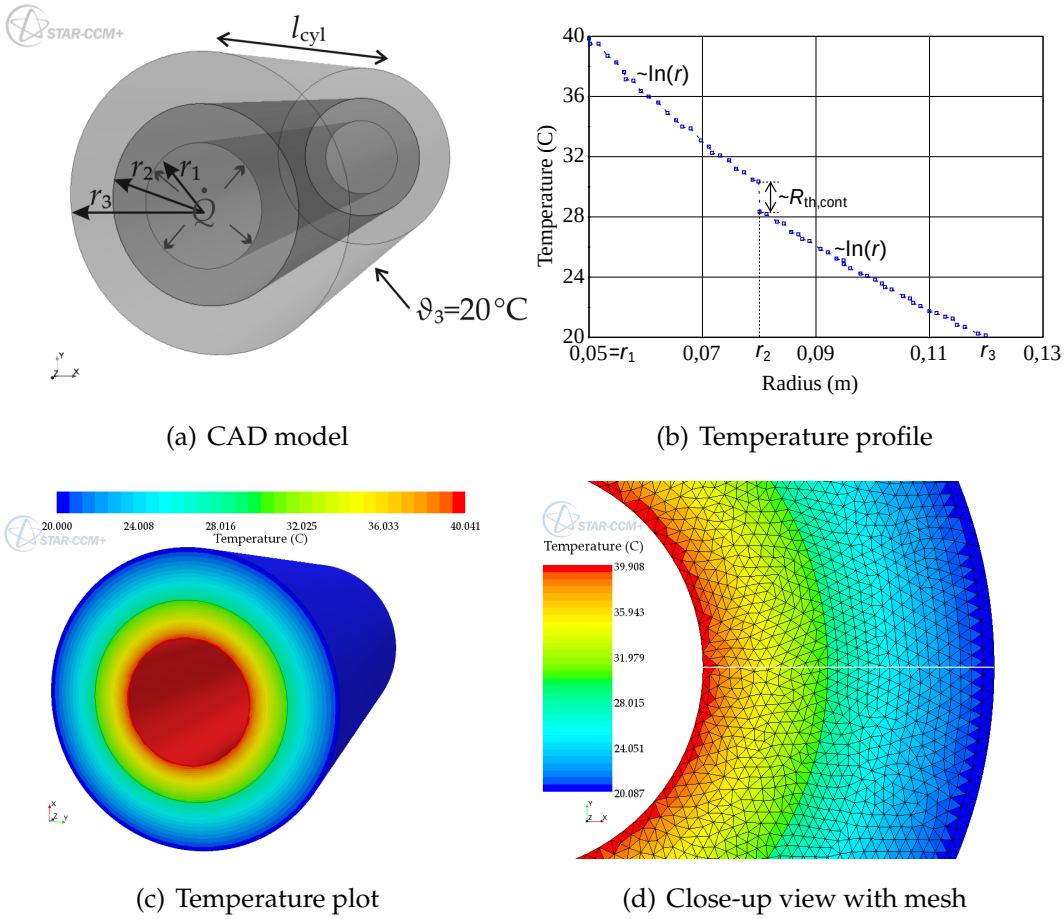

(a) CAD model

(b) Temperature profile

(c) Temperature plot

(d) Close-up view with mesh

Figure 1.8: Numerical simulation of the temperature in the assembly in Fig. 1.2.

The simulation of **convection** requires the simulation of the motion of fluids, which is illustrated in Fig. 1.9 by the simulation of the flow of water through a pipe with an inner radius of $r_1 = 0.0127\,\text{m}$ and the length $l_{\text{cyl}} = 3\,\text{m}$ at two different velocities $v = 0.02\,\frac{\text{m}}{\text{s}}$ and $1\,\frac{\text{m}}{\text{s}}$. Using Eq. (1.23) with $L = 2r_1$ [33], the Reynolds numbers for both cases are $Re = \frac{2r_1 v}{\nu} = 1060$ and 53 100.

The Reynolds number, which describes the ratio between inertia forces and viscous forces (Sec. 1.4.2), is used to distinguish between the different flow regimes. At low Reynolds numbers viscous forces dominate and the flow is laminar, whereas inertia forces (momentum of fluid) dominate at high Reynolds numbers and the flow is turbulent. According to [8,33], flow in a pipe is usually turbulent if $Re > 2300$ and usually laminar if $Re < 2000$. Therefore, laminar flow is expected in the first case and turbulent flow in the second. The simulated velocities of the fully-developed flow on cross-sections perpendicular to the direction of flow are given in Fig. 1.9(a) and 1.9(b).

The approximately parabolic laminar profile and the comparably flat profile in

the turbulent case are confirmed in [30, 33]. In the simulation, the temperature of the fluid is set to $\vartheta = 60\,°C$, the outer surface of the pipe is held constant at $\vartheta = 80\,°C$. Cross-sectional plots near the inlet (Fig. 1.9(c)) and near the outlet (Fig. 1.9(d)) illustrate the gradual heating of the fluid in the laminar case. An analytic calculation of the laminar flow in [33] yields a value of 72 °C for the average water temperature at the outlet.

It may be noted that constant material properties are used in the simulation. If large temperature changes occur, material properties such as the kinematic viscosity might change significantly. In such cases, temperature-dependent material properties should be used instead or, if this is not supported by the used software, the material properties should be adjusted iteratively.

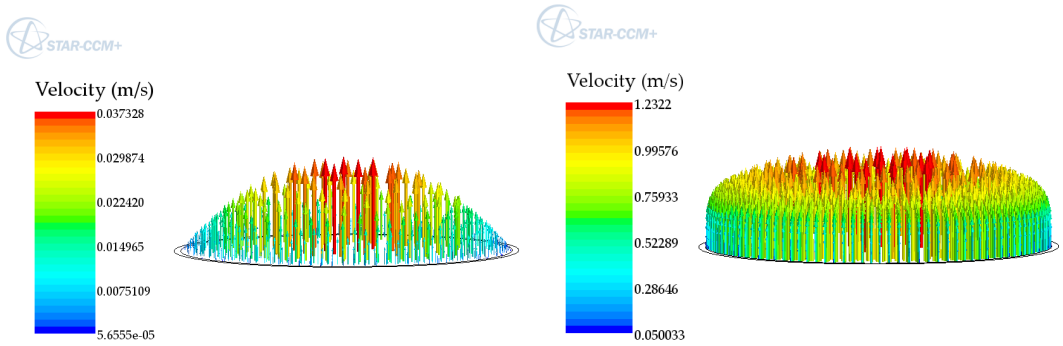

(a) Laminar flow

(b) Turbulent flow

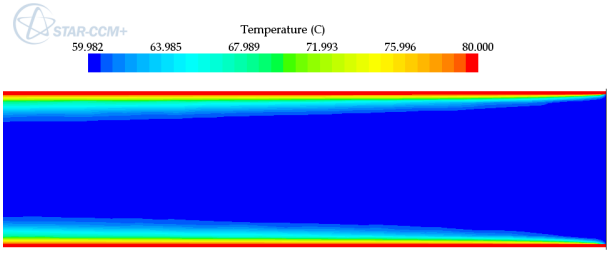

(c) Temperature in the inlet region (first 10 cm, inlet on the right), laminar case.

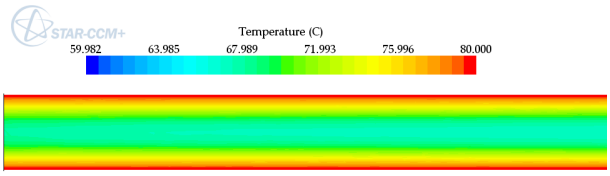

(d) Temperature in the outlet region (last 20 cm, outlet on the left), laminar case.

Figure 1.9: Numerical simulation of water flow through a pipe.

Radiative heat transfer may be simulated with a formulation of Eq. (1.26) for

discrete elements. Commercial software such as STAR-CCM+ typically includes a solver for radiation which can be combined with solvers for conduction and convection [39].

1.5.6 Conclusions

Analytic thermal models of components or even a complete machine assembly may be built by combining lumped parameter models (presented in Sec. 1.5.1), consisting of thermal resistances (due to conduction, convection or radiation) and including losses as lumped loss injections. The losses need to be estimated according to Sec. 1.3. If the transient behaviour shall be modelled, the relevant thermal capacitances are to be calculated and to be connected to the corresponding nodes.

Depending on the desired output temperatures, the general level of detail as well as on the available data and the study context, the resulting thermal networks may differ significantly from study to study. In [42] 6 nodes are used to model the thermal behaviour of a PM synchronous machine, whereas 38 nodes are used in [43] to model an induction machine.

Numerical modelling of heat transfer may be achieved by software packages that allow to solve the equations for conduction, convection and radiation numerically (jointly). Losses in numerical models may be included as conditions, e.g. lumped loss values may be assigned to certain bodies. The loss values or the loss distribution might as well be the result of analytic calculations or come from other numerical tools, such as electromagnetic FEM software. Depending on the available solvers, transient simulations are generally possible (at the expense of calculation time).

The implementations of the heat transfer equations depend on the used software and information on the actual implementations may be found in the corresponding user guides and solver manuals. In this work, STAR-CCM+ v.8–v.10 [39] and JMAG v.13 and v.14 [44] are used for the numerical simulation. MATLAB R2011b [45] is used for the analytic modelling (numerical solution of the analytic models), Motor-CAD v.7.1.6 [46] is used for verification purposes and several CAD models are created or assembled in CREO Parametric 2.0 [47].

Chapter 2

Analysis of modelling approaches

In this chapter, the thermal modelling of the different machine components is analysed in detail. Exemplary models are developed for key components and used to illustrate the model development, the analytic and the numerical analysis as well as to compare both approaches directly.

More specifically, the discussion of thermal contact resistances is followed by detailed studies of the analytic and the numerical modelling of water jacket housings and the slot region (including convective heat transfer in the air gap). Furthermore, the modelling of the rotor, the end winding region, the bearings, and axial heat flow is analysed. Additionally, actual measurements exemplify the effect of adjacent components on the temperatures in the electric machine.

2.1 Thermal contact resistance

As illustrated in Sec. 1.4.4, asperity contacts cause thermal contact resistances between contacting bodies. Values for combinations of contacting materials may be found in the literature, yet only limited data is available on the materials used in electric machines. Since certain contact resistances in electric machinery can significantly influence the thermal behaviour, the identification of relevant contact resistances and the estimation of their magnitudes is an important step in thermal analyses. Potentially important thermal contact resistances may be found between the following components:

- stator stack & stator housing,
- stator stack & stator winding,
- rotor stack & rotor cage winding or buried magnets, and
- rotor stack & shaft.

Values of thermal interface conductances h_{intf} (partly converted from equivalent air gap lengths, Sec. 2.6.1) are summarised in Table 2.1. As the stator windings of elec-

tric machines are typically impregnated, the contact resistance between the stator stack and the stator winding may be regarded as a function of the remaining voids in the impregnation. An experimental analysis of this effect can be found in [48].

Table 2.1: Thermal interface conductances h_{intf}.

Interface	h_{intf} / $(\frac{\text{W}}{\text{m}^2\,\text{K}})$	**Source**
Machine housing and stator stack	350 – 870	[7]
	338 – 2 600	[49]
	420 – 2 630	[38]
	325 – 2 600	[50]
	5 100 – 11 100*	[51]
Rotor stack and rotor bars	430 – 2 600	[7]
Rotor stack and shaft	325 – 2 600	[46]

*Shrink-fit, machined surfaces & thermal interface material employed.

It should be noted that the range given in [38] for the contact resistance between the housing and the stator stack reflects the variation of the thermal interface conductance with contact pressure.

The comparably high values in [51] result from the comparison of nine similar prototypes assembled with, amongst others, different contact pressures, surface finishes as well as with and without thermal interface materials (thermal compound and phase change material). By using a similar set-up and comparing well-defined manufacturing steps, the comparative study clearly shows how the pressure in the contact region influences the contact resistance (decreasing resistance with increasing pressure). Further, it is shown that machining (smoothing) the surfaces reduces the thermal contact resistance. However, the study is limited to one prototype design (with a comparably high thermal interface conductance of $h_{\text{intf}} = 5\,100\,\frac{\text{W}}{\text{m}^2\,\text{K}}$ even in the case of rough surfaces) which therefore forbids to simply apply the values to other machine types. Additionally, the high value of h_{intf} ($h_{\text{intf}} = 11\,100\,\frac{\text{W}}{\text{m}^2\,\text{K}}$), when thermal interface material is used, does not allow for a direct comparison with the other values in Table 2.1. It may nonetheless generally illustrate the effect of thermal interface material.

The results in [49, 50] for various machine types with differing power ratings do not give any clear correlations which would allow to estimate a value for a given machine type. It may also be noted that the contact resistances of the machines with aluminium frames in [49] are comparably small but, as the authors state, the change

of the thermal contact resistance with temperature due to different coefficients of thermal expansion should be accounted for.

In both, analytic and numerical thermal models, the thermal contact resistances are modelled by using values for h_{intf}. If experimental tests are not possible, the ranges given in Table 2.1 may serve as initial values and, if required, values from the literature for typical contacts in engineering problems may be used in addition, e.g. provided in [30, 31, 35].

2.2 Water jacket housing

The heat dissipation in water jacket cooled, totally enclosed electric machines is achieved by the forced flow of a coolant through cooling channels in the cooling jacket, which also serves as the machine housing.

Typical ranges of the heat transfer coefficient h for free and forced convection are compiled in Table 2.2. The comparably high values for forced convection in liquids illustrate why water jackets, which cool the outer surface of the stator stack by forced flow through channels in the cooling jacket, are a comparably simple and effective cooling method, in particular if the cooling circuit may be used to cool the inverter or other components in a vehicle environment as well. The cooling medium is typically a water glycol solution, the frame is typically made of aluminium.

Table 2.2: Typical ranges of h [34].

Convection regime	$h\,/\,(\frac{\mathrm{W}}{\mathrm{m^2\,K}})$
Free convection in gases	2 – 25
Free convection in liquids	10 – 1 000
Forced convection in gases	25 – 250
Forced convection in liquids	50 – 20 000

The heat transfer in the water jacket in Fig. 2.2 is modelled analytically and numerically in order to illustrate the required steps for analysing the heat transfer problem and to allow for a comparison of both modelling approaches.

The input parameters, which are used in the following analyses, are tabulated in Table 2.3. The values have been chosen in order to allow for a comparative analysis with significant temperature gradients in the housing and to ensure turbulent flow in the cooling channels. Typically, the coolant flow rates for the presented cooling jacket (with a non-standard cooling channel design) are lower than the chosen flow

rate in this example. The resulting heat transfer coefficients are consequently also lower than the obtained value in this example. A higher flow rate is chosen to ensure comparability between the numerical and the analytic analysis since the typically existing partly laminar flow would not permit to carry out a sufficiently accurate analytic analysis (suitable for a comparison with the numerical results) considering the cooling jacket design (Sec. 2.2.1, [30]).

In order to allow for a comparison of solely the convective heat transfer in the cooling jacket by analytic and numerical means, the surfaces of the cooling jacket are defined as adiabatic boundaries, i.e. radiation and free convection to the machine surrounding are neglected in the comparative analysis.

Nonetheless, a brief evaluation of radiative and convective heat transfer is given in the following, using the method presented in Sec. 1.4.3 for the modelling of radiation and using an empirical correlation for free convection. Moreover, radiation and free convection between the housing and the ambient are discussed in the frame of both the numerical and the analytic modelling.

The approaches for calculating the radiative and the convective heat transfer between the housing and the surrounding are, strictly speaking, valid for long horizontal cylindrical bodies and the results may therefore be regarded as rather rough approximations, intending to give an overview of the relevance of both heat transfer phenomena.

Radiative heat transfer between the cooling jacket and the surrounding

The estimation of the heat transfer due to radiation from the outer surface of the cooling jacket (treated as a cylinder with r_1) at $\vartheta_1 = 60\,^{\circ}\mathrm{C}$

(i) to a surrounding concentric cylinder with the inner radius r_2 at $\vartheta_2 = 20\,^{\circ}\mathrm{C}$ with a gap of just 4 mm between both cylinders ($\epsilon_1 = 0.04$, $\epsilon_2 = 0.2$) and

(ii) between the cooling jacket and a much larger surrounding body (Eq. (1.27)) at $\vartheta_2 = 20\,^{\circ}\mathrm{C}$ ($\epsilon_1 = 0.04$)

is based on the principles introduced in Sec. 1.26. Rearranging Eq. (1.26) with

$$\text{(i)}\quad F_{12} = 1 \;\&\; \frac{A_1}{A_2} = \frac{{r_1}^2}{{r_2}^2} \text{ and} \tag{2.1}$$

$$\text{(ii)}\quad F_{12} = 1 \;\&\; \frac{A_1}{A_2} \approx 0 \tag{2.2}$$

Table 2.3: Key input parameters for the simulation of the cooling jacket.

Parameter			
Symbol	**Name**	**Value**	**Unit**
ν	kinematic viscosity of the coolant	$1.50 \cdot 10^{-6}$	$\frac{\mathrm{m}^2}{\mathrm{s}}$
ρ	volumetric mass density of the coolant	1060	$\frac{\mathrm{kg}}{\mathrm{m}^3}$
c_p	specific heat of the coolant	3410	$\frac{\mathrm{J}}{\mathrm{kg\,K}}$
λ_fl	thermal conductivity of the coolant	0.394	$\frac{\mathrm{W}}{\mathrm{m\,K}}$
λ_alu	thermal conductivity of the cooling jacket	160	$\frac{\mathrm{W}}{\mathrm{m\,K}}$
$\dot{Q}$	heat injection at inner surface	2000	W
ϑ_in	coolant inlet temperature	60	°C
$\dot{m}$	mass flow rate	1.90	$\frac{\mathrm{kg}}{\mathrm{s}}$

yields (Eq. (1.27) and [30])

$$\text{(i)}\quad h = \frac{\sigma({T_1}^4 - {T_2}^4)}{\left[\frac{1}{\epsilon_1} + \frac{1-\epsilon_2}{\epsilon_2}\left(\frac{r_1}{r_2}\right)\right](T_1 - T_2)} = 0.24\,\frac{\mathrm{W}}{\mathrm{m^2\,K}} \text{ and} \tag{2.3}$$

$$\text{(ii)}\quad h = \frac{\sigma\epsilon_1({T_1}^4 - {T_2}^4)}{(T_1 - T_2)} \qquad = 0.28\,\frac{\mathrm{W}}{\mathrm{m^2\,K}}\,. \tag{2.4}$$

As shown in Eq. (1.27), h and the heat transfer due to radiation highly depend on the temperature difference between both surfaces. Nonetheless, the comparably low values for a temperature difference of 40 °C in the exemplary cases illustrate that radiation only has a minor effect compared with the typically significantly higher values of h for forced fluid flow (Table 2.2) in water jacket cooled electric machines.

Convective heat transfer between the cooling jacket and the surrounding

The value of $\overline{h}$ for convective heat transfer due to free convection between the outer surface of the cooling jacket ($\vartheta_1 = 60\,°\mathrm{C}$) and surrounding air ($T_\infty = 20\,°\mathrm{C}$) is approximated by a correlation for free convection of a horizontal cylinder [30, 34]

$$\overline{Nu} = \left\{0.6 + \frac{0.387Ra^{1/6}}{\left[1 + \left(0.559/Pr^{9/16}\right)\right]^{8/27}}\right\}^2 = \frac{\overline{h}L}{\lambda}, \tag{2.5}$$

where

$\overline{Nu}$ average Nusselt number,

L characteristic length,

Pr	Prandtl number,
λ	thermal conductivity,
Ra	Rayleigh number.

The Rayleigh number Ra is determined with [31, 34]

$$Ra = \frac{g\beta\,(T_1 - T_\infty)\,L^3}{\nu\alpha}, \tag{2.6}$$

where

g	gravitational acceleration ($g = 9.8\,\frac{\mathrm{m}}{\mathrm{s}^2}$),
β	volumetric thermal expansion coefficient,
ν	kinematic viscosity,
α	thermal diffusivity ($\alpha = \frac{\lambda}{\rho c_\mathrm{p}}$).

With $\beta = 3.3 \cdot 10^{-3}\,\frac{1}{\mathrm{K}}$, $\nu = 15.9 \cdot 10^{-6}\,\frac{\mathrm{m}^2}{\mathrm{s}}$, $\alpha = 22.5 \cdot 10^{-6}\,\frac{\mathrm{m}^2}{\mathrm{s}}$, $\lambda = 0.0263\,\frac{\mathrm{W}}{\mathrm{m\,K}}$, and $Pr = 0.707$ [30], as well as with Eqs. (2.5) and (2.6)

$$Ra = 34.5 \cdot 10^6, \tag{2.7}$$

$$\overline{Nu} = 40.9 \quad \text{, and} \tag{2.8}$$

$$\overline{h} = 5.1\,\frac{\mathrm{W}}{\mathrm{m}^2\,\mathrm{K}}. \tag{2.9}$$

The heat transfer coefficient for free convection lies within the typical range given in Table 2.2 and it is just 0.03 %–10 % of the stated values for forced fluid flow.

Conclusions

The relatively low values of the heat transfer coefficients for radiation and free convection—which result from a temperature difference of 40 °C between the surface of the (assumed long cylindrical horizontal) cooling jacket and the surrounding—indicate why only the heat transfer path to the coolant by forced convection is modelled in some studies on water jacket cooled machines, e.g. in [42, 52–54]. The resulting heat transfer by convection and radiation might indeed be negligible if heat transfer coefficients similar to the listed typical range in Table 2.2 are achieved in the cooling jacket.

2.2.1 Analytic modelling

Lumped parameter models of the cooling jacket

Generally, numerous different lumped parameter models may be developed for one and the same component. Two lumped parameter models of a cooling jacket are

shown in Fig. 2.1. The models are analytic in that the components are determined with analytic equations and in that the resulting thermal model or network may be solved analytically. The equations may, however, be based on empirical correlations as in the case of convection. Strictly speaking, even analytic models are commonly solved numerically on computers as well.

The first model in Fig. 2.1(a) is the simplest one for studying the heat transfer problem between the inner surface of the cooling jacket, where heat is injected, and the coolant. $\vartheta_{\mathrm{cj,av}}$, $\vartheta_{\mathrm{fl,av}}$ and ϑ_1 denote the average temperatures of the cooling jacket, the coolant and the inner surface where heat is injected respectively. $C_{\mathrm{th,cj}}$ is the lumped thermal capacitance of the cooling jacket. Similar models are commonly used to simulate water-cooled electric machines, e.g. in [42, 52–54], in particular since the temperature gradients in cooling jacket are typically comparably small.

In the extended model in Fig. 2.1(b), the cooling jacket model is split into three parts, differentiating between the lateral surface and the side surfaces and including terminals to combine the frame model with the model of an electric machine. Similar extended models—which allow to model discrete different temperatures in the housing and therefore generally offer a higher modelling flexibility and accuracy in the case of significant temperature gradients in the housing—are used in [46]. Since the average temperature node is split into several nodes in the extended model in Fig. 2.1(b), the thermal capacitance in Fig. 2.1(a) might need to be split into several thermal capacitances in a transient model. The validity of treating a body as a lumped thermal capacitance, thereby assuming a spatially uniform temperature, may be verified by comparing the body's thermal conductivity with the heat transfer coefficient(s) to the surrounding as shown in [33] and in Sec. 1.5.2.

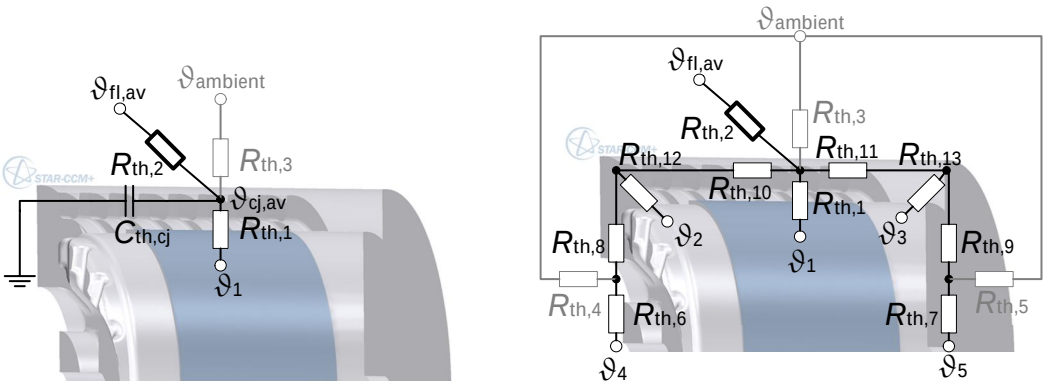

(a) Simple transient model

(b) Extended stationary model

Figure 2.1: Lumped parameter models of the cooling jacket.

The greyed out elements in Fig. 2.1 represent the thermal resistances to include

free convection and radiation to the surrounding.

$R_{\mathrm{th},1}$ is the thermal resistance from the inner surface to the interface to the coolant. $R_{\mathrm{th},2}$ is the lumped thermal resistance modelling the convective heat transfer between the housing and the coolant. $R_{\mathrm{th},3}$ in Fig. 2.1(a) as well as $R_{\mathrm{th},3}$, $R_{\mathrm{th},4}$ and $R_{\mathrm{th},5}$ in Fig. 2.1(b) model the heat flow path from the cooling jacket to the ambient node, which consists of heat conduction from within the cooling jacket to the outer surface of the cooling jacket and heat convection and radiation from the outer surface to the ambient node. $R_{\mathrm{th},6}$–$R_{\mathrm{th},11}$ in Fig. 2.1(b) model the conductive heat flow paths from the bearings to the coolant. $R_{\mathrm{th},12}$ and $R_{\mathrm{th},14}$ model the heat flow path to the inner air and therefore include convective heat transfer between the inner surfaces of the cooling jacket and the inner air.

It should be noted that the connection between the cooling jacket and the model components in Fig. 2.1 is an illustration and $R_{\mathrm{th},12}$, for instance, is not half the axial thermal resistance. The effective conductive length of the heat flow path is influenced by the spatial distribution of the cooling channels.

Modelling of heat transfer by forced convection

The convective heat transfer between the cooling jacket and the coolant is modelled by the (lumped) thermal resistance $R_{\mathrm{th},2}$. The slight conductive component in $R_{\mathrm{th},2}$ (between the virtual average cooling jacket temperature node and the interface) is neglected. Strictly speaking, the interface node and the average temperature node are not necessarily identical. The numerical results in Table 2.4 verify the assumption that the nodes are practically identical.

It is apparent from Fig. 2.1(a) that $R_{\mathrm{th},2}$ models the heat flow related to the temperature difference between the average cooling jacket temperature $\vartheta_{\mathrm{cj,av}}$ and the average coolant temperature $\vartheta_{\mathrm{fl,av}}$, which equals the total injected power $\dot{Q}$ at the inner surface in this study.

In contrast to the numerical simulation, in which the inlet temperature is specified and the temperature at the outlet is the result of the numerical simulation, an average value of the coolant is used in the analytic calculation. Once the heat flow rate to the coolant $\dot{Q}$ is determined, the temperature elevation of the coolant $\Delta\vartheta$ (and the inlet and outlet temperatures) is computed with

$$\Delta\vartheta = \frac{\dot{Q}}{\dot{m}\, c_{\mathrm{p}}}. \tag{2.10}$$

The average heat transfer coefficient $\overline{h}$ is determined with correlations for the average Nusselt number $\overline{Nu}$. As a detailed analytic study of the complex cooling channel shape would exceed the scope of the thesis, an approximation for the convective

heat transfer in the eight parallel cooling channels is found. The complex inflow region, consisting of the transition region from the inlets and outlets to the three parallel branches that branch into the eight parallel cooling channels, would need to be analysed jointly with special attention to the effects in each entry region. An identical mass flow rate in each channel ($\dot{m}/8$) is assumed.

The cooling channels of the exemplary cooling jacket are not circular, as may be seen in Figs. 2.2(b) and 2.3. For non-circular ducts, the hydraulic diameter d_h is used as the characteristic length L in Eq. (1.23), instead of the diameter in the case of circular channels. d_h is defined in terms of the cross-sectional area A and the wetted perimeter of the channel l_w as [30, 33]

$$d_\mathrm{h} = \frac{4A}{l_\mathrm{w}}. \tag{2.11}$$

Correlations for the flow through circular tubes, which have been studied extensively, may be used for non-circular tubes, in particular in the case of turbulent flow [30]. The reduction of the velocity of the fluid near sharp corners may, however, affect the accuracy of this approach. As the flow in the cooling channels is turbulent for the given mass flow rate ($Re = 1.09 \cdot 10^4$) and $Pr = 13.8$, the *Gnielinski correlation* [55], taken from [30], is used to determine Nu

$$Nu = \frac{(\varsigma/8)\,(Re - 1000)\,Pr}{1 + 12.7\,(\varsigma/8)^{1/2}\,(Pr^{2/3} - 1)}. \tag{2.12}$$

(In the case of laminar flow, Nusselt numbers for tubes with different cross sections may be found in the literature, e.g. in [30].)

Generally, the friction factor ς is determined by the *Moody chart* (e.g. in [30,31,33]) for rough surfaces. The *Petukhov formula* is employed to model the smooth interface in this example [35].

$$\varsigma = (0.790 \ln Re - 1.64)^{-2} \tag{2.13}$$

Using the input parameters as well as Eqs. (2.12) and (2.13) yields

$$\varsigma = 0.0307 \text{ and} \tag{2.14}$$

$$Nu = 111. \tag{2.15}$$

Nu applies to fully developed flow. In the entry region of the channels, the velocity and the temperature profile (Sec. 1.4.2) are not yet fully developed. Therefore, the determined Nusselt number for fully developed flow does not equal the average Nusselt number that is needed to determine the average heat transfer coefficient. According to [33], the entry region is shorter in turbulent flows with high Prandtl

numbers and both requirements are fulfilled in the studied case. Thus, the assumption $Nu \approx \overline{Nu}$ is made and the error is estimated to be below 10 % with the chart provided in [33] for the thermal entry Nusselt number in circular tubes.

Consequently, the approximated average heat transfer coefficient is

$$\overline{h} = \frac{\lambda\,\overline{Nu}}{L} = 3190\,\frac{\mathrm{W}}{\mathrm{m^2\,K}}. \tag{2.16}$$

With the interface surface area A, the thermal resistance $R_{\mathrm{th},2}$ due to forced convection in the cooling channels is

$$R_{\mathrm{th},2} = \frac{1}{\overline{h}\,A} = 1.26 \cdot 10^{-3}\,\frac{\mathrm{K}}{\mathrm{W}}. \tag{2.17}$$

The determined value of $R_{\mathrm{th},2}$ may be regarded as an approximation as correlations for circular pipes have been used and the Nusselt number for fully developed flow is applied to the complete interface, including the inlet and the outlet region.

The average coolant temperature $\vartheta_{\mathrm{fl,av}}$ is calculated with Eq. (2.10)

$$\vartheta_{\mathrm{fl,av}} = \vartheta_{\mathrm{in}} + \frac{\Delta\vartheta}{2} = \vartheta_{\mathrm{in}} + \frac{\dot{Q}}{2\,\dot{m}\,c_{\mathrm{p}}} = 60\,^{\circ}\mathrm{C} + 0.154\,^{\circ}\mathrm{C} = 60.2\,^{\circ}\mathrm{C}. \tag{2.18}$$

From the thermal resistance $R_{\mathrm{th},2}$, the average fluid temperature $\vartheta_{\mathrm{fl,av}}$ and the heat transfer to the coolant, which is identical with the injected heat $\dot{Q}$ in this example, $\vartheta_{\mathrm{cj,av}}$ may be computed as

$$\vartheta_{\mathrm{cj,av}} = \vartheta_{\mathrm{fl,av}} + \dot{Q} R_{\mathrm{th},2} \tag{2.19}$$

and ϑ_1 with

$$\vartheta_1 = \vartheta_{\mathrm{fl,av}} + \dot{Q}\,(R_{\mathrm{th},1} + R_{\mathrm{th},2})\,. \tag{2.20}$$

$R_{\mathrm{th},1}$ is approximated by a hollow cylinder spanning from the inner surface of the cooling jacket to the cooling channels and is calculated with Eq. (1.17). Using the input parameters and the computed values yields

$$\vartheta_{\mathrm{cj,av}} = 62.7\,^{\circ}\mathrm{C} \text{ and} \tag{2.21}$$

$$\vartheta_1 = 64.2\,^{\circ}\mathrm{C}. \tag{2.22}$$

2.2.2 Numerical modelling

CAD model

In order to minimise the required number of elements in the meshed representation, features of CAD models, such as design elements for mounting the electric machine

that are not required for a numerical analysis, may be removed or simplified to basic shapes. The simplified CAD model of the cooling jacket is given in Fig. 2.2(a), the inflow and outflow regions and the eight parallel cooling channels branching from three parallel inflow paths are illustrated in the transparent scene in Fig. 2.2(b).

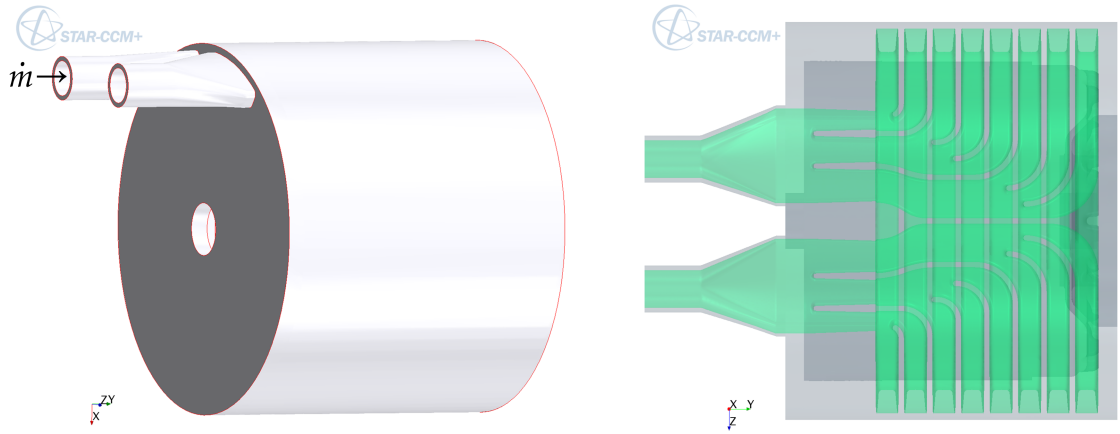

(a) Surface view and (mass flow) inlet (b) Transparent scene

Figure 2.2: CAD model of the cooling jacket.

Meshed representation

The CAD model of the cooling jacket and the extracted fluid volume are converted into meshed representations that are connected by a conformal interface. The resulting (comparably fine) mesh consists of polyhedral elements with prismatic layers at the boundaries, $11.5 \cdot 10^6$ elements in total. Prismatic layers are not only generated in the fluid domain (in order to resolve the near-wall region) but also in the thin solid in order to ensure a certain number of element layers, while keeping the element count within reasonable boundaries.

Boundary conditions and parameters of the numerical analysis

The material properties used in the numerical analysis may be found in Table 2.3. The inlet is defined by the mass flow rate at the inlet ($\dot{m}$) and the temperature of the coolant at the inlet (ϑ_{in}). The total heat $\dot{Q}$ is injected as a spatially uniform heat flux density at the inner surface of the cooling jacket that would be in direct contact with the outer surface of the stator stack (Fig.2.4). The remaining surfaces of the cooling jackets are defined as adiabatic boundaries with the exception of the interface to the fluid, which is defined as an imprinted in-place contact boundary in order to allow the transfer of heat at the interface between both domains. The surfaces are defined as smooth faces.

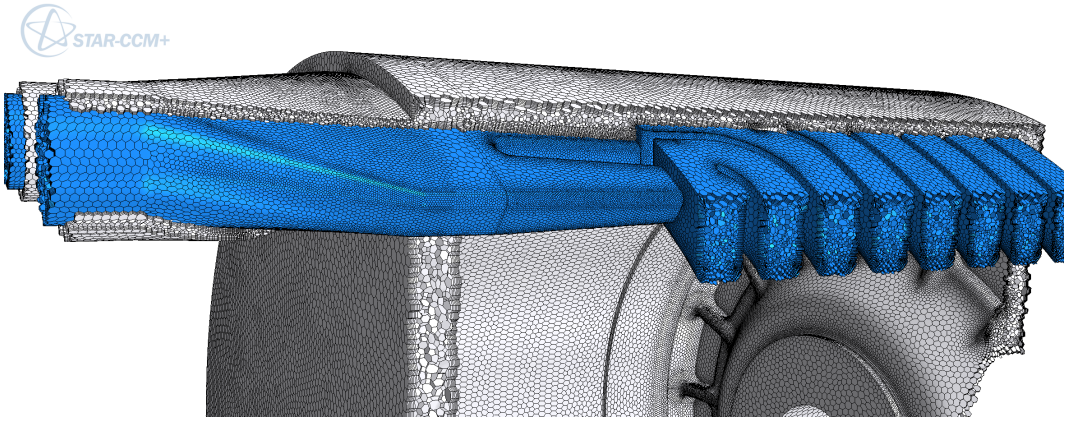

Figure 2.3: Cut-open view of the mesh.

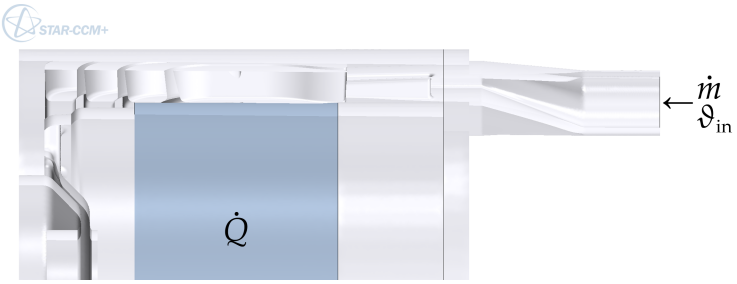

Figure 2.4: Spatially uniform heat injection (heat flux density) at coloured surface.

A segregated approach is used to model the fluid flow and the corresponding solver is linked with the solver modules for heat transfer in the fluid and in the solid domain. A modified $k - \epsilon$ turbulence model is employed [39].

Numerical analysis

The numerical simulation fully converges in around 3 h and 800 steps on a hexa-core CPU with 3200 MHz and 64 GB RAM, using 11 parallel computational processes and approximately 10 GB RAM.

The results of the numerical simulation are compiled in Table 2.4 together with the analytic results from Sec. 2.2.1.

The simulated temperature distribution on the surfaces of the cooling jacket is shown in Fig. 2.5. Additional streamlines indicate the direction of flow and the temperature of the fluid in the cooling channels. The cut-open view shows the surfaces on the opposite side of the inlet and the outlet.

The (unsmoothed) temperature distribution in the solids is given in Fig. 2.6 for each (polyhedral or prismatic) cell in the cutting plane and on the visible surfaces.

As expected, the hotspot are found on the inner surface of the cooling jacket,

Table 2.4: Numerically determined temperatures together with results from analytic model.

Symbol	Name	Temperature / °C	
		Numerical	Analytic
$\vartheta_{\mathrm{if,av}}$	average interface temperature	61.7	62.7
$\vartheta_{\mathrm{cj,av}}$	average cooling jacket temperature	61.9	62.7
ϑ_{out}	average coolant temperature at the outlet	60.3	60.3
$\vartheta_{\mathrm{fl,av}}$	average coolant temperature	60.2	60.2
ϑ_1	average temperature of inner surface	66.3	64.2

where the heat is injected (Figs. 2.5 and 2.6). Further, the spatial arrangement of the cooling channels leads to notable temperature gradients on the inner surfaces and inside the cooling jacket (Fig. 2.5). The coolant, however, exhibits only minor temperature gradients. This stems from the fact that the high mass flow rate only causes an overall temperature increase of 0.31 K (Eqs. (2.10) and (2.18)) with the given heat injection, as may be seen in Figs. 2.5 and 2.6.

The slight temperature difference between the upper side of the cooling jacket, in particular near the inlet, and the lower side opposing the inlet—which may be seen clearly in Fig. 2.6—is due to the additional cooling effect of the entrance region. For the same reason, the cooling jacket is warmer on the opposite end of the inlet in Fig. 2.5.

As stated in Sec. 1.4.2 (Eq. (1.21)), an average heat transfer coefficient requires integrating the local heat transfer coefficient over the interface. The local heat transfer coefficient itself may be determined according to Eq. (1.20) from the heat flux and the wall (interface) temperature but it also requires the definition of a reference temperature (e.g. the free-stream temperature T_∞ in Eq. (1.20)). The local heat transfer coefficient and thus the average heat transfer coefficient are therefore ambiguous as they depend on the local reference temperatures.

In order to provide a simple comparison between the heat transfer coefficient of the analytic approach and the numerical results, an average numerical heat transfer coefficient may be derived simply from the results in Table 2.4. Assuming $\overline{h} = h$ and consequently setting the reference temperature to the average coolant temperature ($T_\infty = \vartheta_{\mathrm{fl,av}} = 60.2\,^\circ\mathrm{C}$), using Eq. (1.22) (with $T_\mathrm{p} = \vartheta_{\mathrm{if,av}} = 61.7\,^\circ\mathrm{C}$) yields $\overline{h} = 5160\,\frac{\mathrm{W}}{\mathrm{m^2\,K}}$.

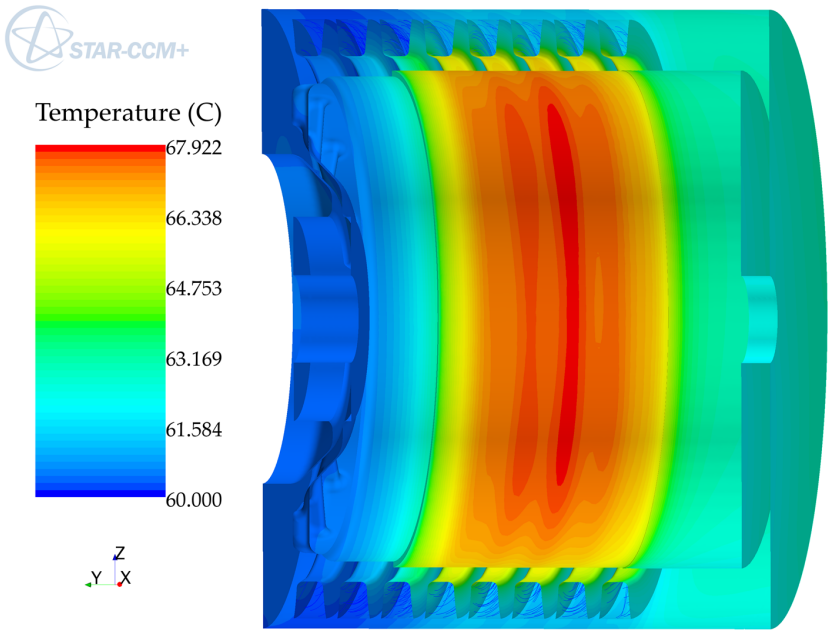

Figure 2.5: Cut-open view showing the temperature distribution on the surfaces and in the cooling channels (streamlines).

2.2.3 Conclusions

In the analytic model in Fig. 2.1(a) the assumption has been made that the average cooling jacket temperature equals the average interface temperature. The numerical analysis gives a temperature difference of 0.12 K (Table 2.4) between the interfacial and the average temperature, validating this assumption.

Comparing the analytic and the numerical analysis does not only show differing results for the average temperatures of the cooling jacket and the inner surface. It also reveals fundamental differences of both approaches.

Correlations have been used in the analytic analysis to calculate the average heat transfer coefficient and the corresponding lumped thermal resistance due to forced convection. Therefore, the complete temperature distribution in the cooling jacket, which is shown in Figs. 2.5 and 2.6, is modelled by just one average temperature in the presented simple analytic approach. Consequently, the information about the maximum local temperature of the inner surface in Fig. 2.5 is also lost and local effects, such as hot spots, cannot be evaluated.

Modelling temperature differences in the cooling jacket requires a subdivision of the cooling jacket into several nodes and using several thermal resistances from these nodes to the coolant. The determination of correct values would, however, require a difficult, if not impossible, precise analysis of the heat flow paths in the cooling jacket and to the coolant.

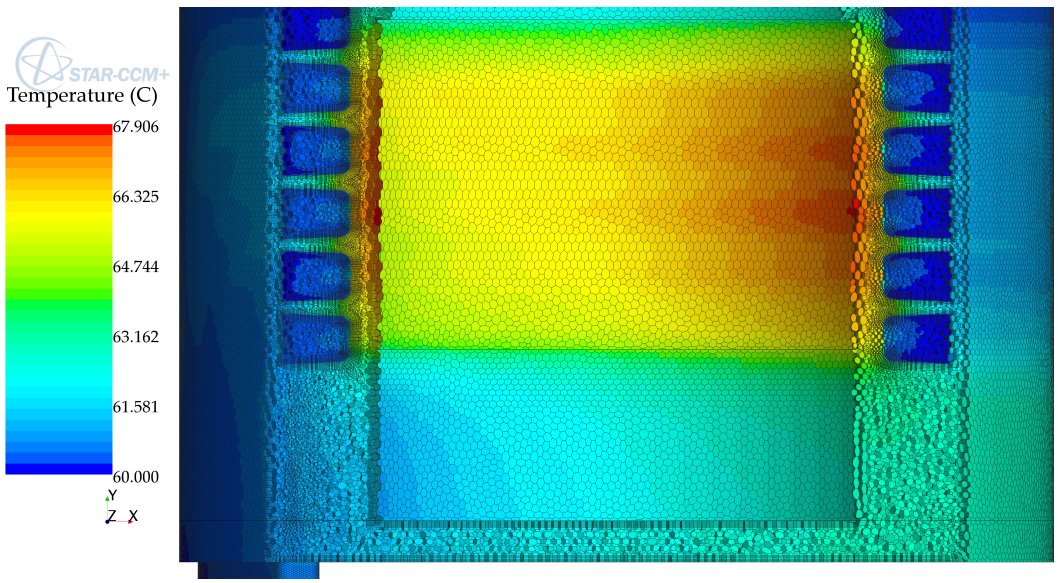

Figure 2.6: Cut-open view showing the temperature distribution in both domains.

The analysis of convective heat transfer due to the turbulent flow in the non-circular channels has been reduced to an analysis of circular channels. For the sake of simplicity, the inlet and the outlet regions leading to the cooling channels have been modelled by the same average Nusselt number, which is a significant simplification. The accuracy could be improved by analysing the flow in the inlet regions separately, paying attention to the effects in each entry region, and by combining this with the convective heat transfer in the cooling channels.

The numerical simulation, by contrast, allows the direct calculation of the branching channels in the inlet regions and the study of the flow through the edged channels and gives the spatial distribution in all domains. The detailed information obtained from CFD simulations comes, however, at the cost of computation time and more complex model adjustments.

The analytic calculation yields results for the temperature levels practically instantaneously. In the case of changes of the input parameters, such as the inlet temperature, the mass flow rate or the channel length, the input parameters in the corresponding equations need to be adjusted and, if the flow regime changes, the used correlation might need to be modified or changed.

The numerical simulation requires (i) the development of a CAD model, (ii) the generation of a volume mesh, (iii) the choice of the correct solver modules, (iv) setting up the input parameters and the boundary conditions, and (vii) the post-processing the results. The simulation of different scenarios requires separate simulations, each taking up to a few hours for a stationary simulation. In the case of changes of the geometry, at least the CAD model needs to be modified and re-

meshed (steps (i) and (ii)), which may take up to a few hours or even days.

Relevance of thermal resistances

If thermal resistances have a dominant effect in heat flow paths, the remaining resistances may be negligible. The thermal resistance of aluminium is, for instance, small compared with the thermal resistance due to convection and radiation but lies within the same range as the thermal resistance modelling the convective heat transfer to the coolant.

This may be exemplified by determining the thickness d of a rectangular aluminium body that would result in a (conductive) thermal resistance that equals the thermal resistance of free convection of a body with the same surface, with $\lambda_{\text{alu}} = 160\,\frac{\text{W}}{\text{m K}}$ (Table 2.3) and the median value for the average heat transfer coefficient for free convection in gases $\overline{h} = 13.5\,\frac{\text{W}}{\text{m}^2\,\text{K}}$ (Table 2.2).

$$\frac{1}{R_{\text{th,conv}}} = \overline{h}A = \frac{A\lambda}{d} = \frac{1}{R_{\text{th,cond}}} \tag{2.23}$$

$$\Leftrightarrow \qquad \overline{h} = \frac{\lambda}{d} \tag{2.24}$$

$$\Rightarrow \qquad d = \frac{\lambda}{\overline{h}} = \frac{160\,\frac{\text{W}}{\text{m K}}}{13.5\,\frac{\text{W}}{\text{m}^2\,\text{K}}} = 11.9\,\text{m}. \tag{2.25}$$

The thermal resistance $R_{\text{th,3}}$ in Fig. 2.1 models the heat flow path from within the cooling jacket to the ambient node and comprises a conductive component in the aluminium to the surface and the combination of radiative and convective heat transfer to the ambient node. Considering the high value of d in Eq. (2.25), which would lead to the same thermal resistance as free convection, heat conduction in the aluminium cooling jacket ($R_{\text{th,cond}}$ and the resulting temperature drop) is not relevant in the flow path to the ambient node. Consequently, the correct identification of the resulting thermal resistance due to conduction from near the channels to the outer surface is of minor relevance and the corresponding resistance may be neglected.

Similarly, using the computed value $\overline{h} = 3190\,\frac{\text{W}}{\text{m}^2\,\text{K}}$ in Eq. (2.16) for the average heat transfer coefficient that models the convective heat transfer to the coolant yields

$$d = \frac{\lambda}{\overline{h}} = \frac{160\,\frac{\text{W}}{\text{m K}}}{3190\,\frac{\text{W}}{\text{m}^2\,\text{K}}} = 0.0502\,\text{m}. \tag{2.26}$$

Eq. (2.26), by contrast, indicates that the conductive element in the heat flow path between the inner surface and the coolant $R_{\text{th,1}}$ in $(R_{\text{th,1}} + R_{\text{th,2}})$ is of significant importance.

The comparison between the listed ranges of the thermal interface conductance h_{intf} (ranging between 350 $\frac{\mathrm{W}}{\mathrm{m^2\,K}}$ and 11 100 $\frac{\mathrm{W}}{\mathrm{m^2\,K}}$ in Table 2.1) and the typical ranges of h for forced convection in fluids (ranging between 50 $\frac{\mathrm{W}}{\mathrm{m^2\,K}}$ and 20 000 $\frac{\mathrm{W}}{\mathrm{m^2\,K}}$ in Table 2.2) shows very clearly that, if an electric machine is fitted into a water jacket, the contact resistance significantly influences the heat flow path to the coolant. Moreover, in water-cooled electric machines most internally generated heat is dissipated by the cooling jacket and, consequently, the contact resistance of the interface between the stator stack and the cooling jacket has a considerable influence on most calculated temperatures in electric machine models.

2.3 Slot modelling

The stator winding of electric machines in the power range considered in this thesis typically consists of thin enamelled copper wires that are placed (rather randomly) in the stator slots. The wires and the stator stack are separated by a slot insulation (slot liner). In the case of two-layer windings, a separator is placed between the coil sides of the different phases. The slot is closed by a slot wedge and filled with an impregnation resin during the impregnation of the machine.

The different components are shown in the exemplary slot model in Fig. 2.7, which is similar to the presented assemblies in [7, 56] with the exception that the slot liner at the top of the slot is not folded underneath the slot wedge in the CAD model in Fig. 2.7. In order to simplify the mesh generation and the correct interface definition, no impregnating resin is modelled above the slot wedge, i.e. between the wedge and stator as well as between the wedge and the slot liner. At the same time, this assumption allows to study the effect of resulting air-filled cavities at the tooth top which may occur in the case of a non-ideal impregnation in this region.

The different model components as well as typically used materials and their properties are provided in the following. This ensures the use of well-founded values but does not limit the validity of the models in which these values are used. The choice of a different impregnating resin, e.g. epoxy, just requires an adjustment of the corresponding input parameters in the analytic equations or the numerical software.

2.3.1 Copper wires

Enamelled round copper wires are standardised in IEC standard 60317-0-1 [57]. More specifically, enamelled round wires with dual coating (enamelled round copper winding wire with an underlying coating that is based on polyester or **p**oly**e**ster-

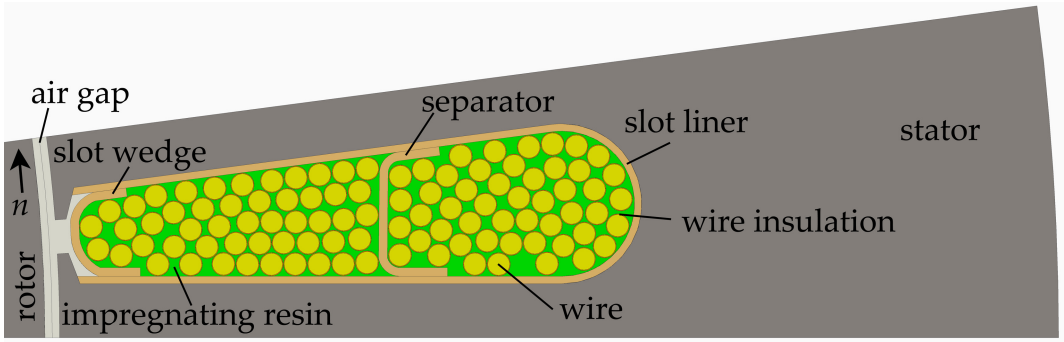

Figure 2.7: Detailed CAD model of a stator slot with inserted double-layer winding (with ideal impregnation).

imide (PEI) and a superimposed **p**oly**a**mide-**i**mide (PAI) coating) are standardised in IEC standard 60317-13 [58].

The wire copper diameter and the overall wire diameter (including the wire insulation) in the CAD model in Fig. 2.7 have been chosen in accordance with IEC standard 60317-13; according to [35], the thermal conductivity of (electrolytic tough pitch, ETP) copper is 386 $\frac{\mathrm{W}}{\mathrm{m\,K}}$.

The wire enamel is typically composed of 60 to 80 % PEI and 20 to 40 % PAI [59]. According to [60], the thermal conductivity of PEI lies in the range of 0.17 $\frac{\mathrm{W}}{\mathrm{m\,K}}$ to 0.23 $\frac{\mathrm{W}}{\mathrm{m\,K}}$ (Sec. 2.3.2), the thermal conductivity of PAI (Torlon 4000T®) in [59] is 0.24 $\frac{\mathrm{W}}{\mathrm{m\,K}}$.

The large variations of the overall wire diameter—which are permissible according to the corresponding IEC standards—and the fact that data sheets typically refer back to the standards do not allow to determine the thickness of each coating precisely and, thus, the thermal conductivities separately. Also, the large variations only allow for an approximate averaged estimate of the overall insulation thickness. The dual coating wire enamel may therefore be modelled by one wire enamel layer with an equivalent combined thermal conductivity.

If the wire enamel and the impregnating resign have similar thermal conductivities, an explicit modelling of the wire enamel might not be required. Instead, it might be treated as a part of the impregnation, reducing the number of components in the slot model and thus the complexity of the mesh.

2.3.2 Insulating materials

Ageing-related deterioration of the insulating materials is directly linked with the temperature the insulation is exposed to during machine operation. Thermal classes that give the recommended maximum permissible temperature for insulating ma-

terials, as well as for insulating systems, are defined in IEC standard 60085 [61]. The temperature classes are summarised in Table 2.5 and the commonly used *Class H* (180 °C) insulation materials are used in the following. It may be noted that the temperature class of an insulating material may differ from the (potentially higher) temperature class of the same material when it is used as part of an insulating system.

Table 2.5: Thermal classes according to IEC standard 60085 [61].

Thermal class (°C)	**Letter designation**
90	Y
105	A
120	E
130	B
155	F
180	H
200	N
220	R
250	–

Impregnation

The stators of electric machines may be impregnated by several different methods, e.g. *vacuum pressure impregnation*, *trickle impregnation*, the *roll dip* as well as the *dip and bake* method, and the *current UV impregnation* method [7, 56].

During the impregnation of the stator, most air gaps between the wires, the stator and the insulating materials are filled with impregnating resign, reinforcing the mechanical strength, improving the protection against environmental influences and increasing the thermal conductance between the wires and the stator.

In addition to the thermal properties of the impregnation, the impregnation goodness, i.e. the number or extent of the remaining voids, may have a significant influence on the local temperature distribution and, more generally, on the overall average temperatures.

Local effects may be analysed by explicitly modelling voids in a model similar to Fig. 2.7. The macroscopic influence on the temperatures may be accounted for by impregnation goodness factors which are investigated experimentally in [48, 62] and which are used in the analytic computations in [46].

Polyester (imide) resins may be used in the covered power range [7, 63] with a thermal conductivity in the range of 0.17 $\frac{W}{mK}$ to 0.23 $\frac{W}{mK}$ [60].

Slot insulation, separator and wedge

The slot insulation as well as slot separator and slot wedge are typically composite materials. If the thermal conductivity is not stated in the datasheets, it may be approximated by combining the thermal conductivities of each component.

To give an example, a *Class H* (180 °C) insulating material consisting of a polyester (polyethylene terephthalate, PET) layer between two layers of NOMEX® (aramid paper).

The thermal conductivity of PET film lies in the range of 0.13 $\frac{W}{mK}$ to 0.15 $\frac{W}{mK}$ [64, 65], the thermal conductivity of NOMEX® aramid paper layers vary between 0.094 $\frac{W}{mK}$ (nominal thickness of 0.05 mm) and 1.5 $\frac{W}{mK}$ (nominal thickness of 1.5 mm) [66, 67]. It is apparent from [66, 67] that not only the conductance but the conductivity itself is significantly influenced by the layer thickness.

Neglecting the adhesives and possible contact resistances, the thermal conductivities in the slot model of the insulating components may be estimated by calculating the weighted sum of the thermal resistivities, using the thickness of each layer.

2.3.3 Electrical steel

The non-oriented electrical steel, which is used in electric machinery and which is available in numerous thicknesses and grades according to the specified maximum permissible specific iron losses at 50 Hz and 1.5 T, is standardised in (DIN) EN standard 10106 [13]; their insulating coating is classified in IEC standard 60404-1-1 [68]. The thermal conductivity of the electric steel depends on the alloy content and therefore on the exact steel type [69]. The values of the thermal conductivity in [69] vary between 21.5 $\frac{W}{mK}$ (3.45 % combined Si + Al content) and 34.0 $\frac{W}{mK}$ (1.40 % combined Si + Al content). [70] states a thermal conductivity of 28 $\frac{W}{mK}$ for an electrical steel with 3 % Si and 0.4 % Al content.

The thermal conductivity of the coating depends on the used coating type with the coatings differing significantly in their chemical composition. In [70], the thermal conductivity through the flat steel sheet (perpendicular direction) with a *Type C5* coating is 0.37 $\frac{W}{mK}$, which corresponds to a thermal conductivity of the coating of around 0.03 $\frac{W}{mK}$.

Despite the varying thermal conductivities with steel and coating type, the conductivity along the flat steel sheet is generally significantly higher than the thermal conductivity of the coating. The thermal conductivity of stacked electrical steel

sheets in electric machines is therefore significantly lower in axial direction (through the coatings) than in radial direction.

The thermal conductivities of copper and aluminium (Tables 2.3 and 2.6) are also significantly higher than the axial conductivity of stacked electrical steel. Axial heat flow through the rotor and stator stack is consequently typically neglected in thermal machine models, e.g. in [36, 42, 71–73].

2.3.4 Model overview

The CAD model in Fig. 2.7 is used to analyse the numerical and the analytic slot modelling. Moreover, it serves to study the effect of simplifying the actual detailed slot model, to investigate the effect of locally varying losses and to assess the influence of the air gap on the temperature distribution inside the slot.

The parameters of the slot model are given in Table 2.6. The air gap in Fig. 2.7 is analysed separately in Sec. 2.5. The air gap and the rotor are therefore not included in the models in this section.

The thermal conductivity of the slot liner, the slot wedge and the separator are computed according to Sec. 2.3.2, using the conductivity $0.114\,\frac{\mathrm{W}}{\mathrm{m\,K}}$ that is given in [66] for 80 µm aramid paper. The wire enamel is modelled by a perfectly uniform film thickness and the value of the thermal conductivity is based on the ratio: 60 % PEI to 40 % PAI. The mean value of the stated ranges for PEI impregnating resin in Sec. 2.3.2 is chosen. The resulting slot fill factor, i.e. the ratio of the conductor (copper) area over the total slot area ($85.7\,\mathrm{mm}^2$), of 51.5 % may be regarded as a comparably high value for the used winding type.

The effect of the widening tooth cross-section at the comparably small tooth tip on the radial heat flow in the tooth is neglected. The tooth is, instead, treated as having a constant (equivalent) tooth width, the equivalent (average) slot width is derived from the CAD model, using the slot area and the tooth width. Both values are provided in Table 2.6.

The outer surface (edge) of the stator back iron is defined as the boundary to a reference (ambient) temperature to which it is connected by a (convective) heat transfer coefficient. The value is a typical value for forced convection in liquids (Table 2.2). A potential heat flow across the air gap to the stator teeth is modelled by a constant heat flux (heat rate) that enters the tooth.

Both sides of the model (the boundaries of both tooth halves) are adiabatic boundaries and no heat is transferred across the boundaries due to symmetry.

The slot model itself is not coupled to a circuit simulation and the winding scheme is therefore not considered in this model. Instead, an identical averaged current flow

is assumed in each of the wires. Two simplified loss cases are simulated, namely the case of identical averaged losses in all wires (identical, uniform loss density; case (i)) and, additionally, a temperature-dependent loss density is modelled in the wires (case (ii)). The temperature-dependent loss density is modelled by using defined copper losses at the reference temperature (20 °C) and the linear temperature coefficient of copper (Sec. 1.3.1). For an easier comparison with case (i), the total losses in the wires in case (ii), i.e. the integral of the loss densities in the wires, are also used in case (i).

Moreover, the detailed slot model is compared with a simplified numerical model in which the slot is represented by a single lumped body. This concept is commonly used in both analytic as well as numerical models since the development and the analysis of detailed slot models are time-consuming tasks. It is also not possible to find exact analytic solutions to the complex 2D heat flow problem (strictly speaking even a 3D problem because of axial heat flow) and simplified approaches are required, as will be shown in Sec. 2.3.6.

It may be noted that the CAD slot model in Fig. 2.7 is actually a 3D model as this simplifies the meshing and the analysis with the used 3D software. The numbers of elements in the meshed representations, which are provided in the following sections, therefore refer to thin 3D models that consist of a few element layers. The 3D CAD model also allows to verify the presence of predominantly two-dimensional flow in the air gap.

It may also be noted that the presented analytic and numerical models do not account for the local effects of voids (caused by imperfect impregnation) on the temperature field. Random voids may be added to the CAD model in order to study their effect. More general approaches—that might succeed in modelling the average temperature elevation but fail to model the real local effects—scale the thermal conductivity in the slot or use an additional contact resistance between the electrical steel and the slot. As such averaging approaches do not improve the accuracy in predicting the spacial temperature distribution compared with the studied CAD model, the impregnation goodness is left out of consideration and an ideal impregnation is assumed in the models.

2.3.5 Numerical modelling

Detailed slot model

The meshed representation of the detailed slot model (without air gap and rotor) consists of $2.15 \cdot 10^6$ elements. A polyhedral mesher is used in order to be able to build a conformal interface to the air gap in Sec. 2.5. Due to the high mesh density,

Table 2.6: Parameters of the slot model in Fig. 2.7.

Parameter	Value	Unit
Geometry		
Wire diameter	0.804	mm
Wire copper diameter	0.75	mm
Slot liner thickness	0.25	mm
Slot wedge thickness	0.3	mm
Separator thickness	0.3	mm
Number of wires	100	1
Slot fill factor	51.5	%
Air gap length	0.5	mm
Outer diameter (outer yoke edge)	174	mm
Inner diameter (tooth tip)	105.5	mm
Line contact length between slot liner and teeth	33.1	mm
Line contact length between slot and back iron	8.59	mm
Tooth height	17.24	mm
Tooth width (both halves)	3.70	mm
Equivalent tooth width (both halves)	3.77	mm
Equivalent slot width	4.33	mm
Model angle (corresponds to a full motor with 48 slots)	7.5	°mech.
Thermal conductivities		
Copper	386	$\frac{W}{mK}$
Wire insulation	0.22	$\frac{W}{mK}$
Slot liner	0.12	$\frac{W}{mK}$
Slot wedge	0.13	$\frac{W}{mK}$
Separator	0.13	$\frac{W}{mK}$
Impregnating resin	0.20	$\frac{W}{mK}$
Electrical steel	28	$\frac{W}{mK}$
Reference copper losses (per unit length) at 20 °C	140	$\frac{W}{m}$
Linear temperature coefficient (copper losses) at 20 °C	0.0039	$\frac{1}{K}$
Ambient temperature	60	°C
Heat transfer coef. between outer stator yoke edge & ambient	1000	$\frac{W}{m^2K}$
Heat injection from the rotor (per unit length)	20	$\frac{W}{m}$

the elements would not be visible in a figure of the complete model. A close-up view of the mesh is hence provided instead in Fig. 2.8(a). The element size of the mesh may still be seen in the unsmoothed temperature distributions in Figs. 2.9(a) and 2.9(b) (*jagged* isotherms).

The simulated temperature distribution with the temperature-dependent copper loss density in Fig. 2.9(a) is compared with the simulation using a spatially uniform loss density in the wires in Fig. 2.9(b). The spatially uniform losses in the wires equal the total losses in the temperature-dependent case.

As expected, the hot spots in Figs. 2.9(a) and 2.9(b) are found in the vicinity of the slot wedge since the air gap is not modelled and the slot wedge, which would be in contact with air, is consequently an adiabatic boundary. Moreover, the temperature is generally highest along the centre line of the slot.

Generally, both temperature distributions seem rather similar and the difference between the uniform loss density case and the temperature-dependent loss definition may be considered negligible. It may nonetheless be seen in Fig. 2.9(a)—particularly in the slot wedge region and along the centre line—that the hot spots are prone to elevated temperatures in the temperature-dependent case since higher temperatures lead to increased heating compared with the uniform case.

The minimum, the maximum and the average temperatures in the slot and in the stator part are summarised in Table 2.7. The average temperature inside the slot is in both cases 115 °C, the average temperature of the stator part is 89.6 °C. The maximum temperature in the slot is slightly higher (+0.4 K) in the temperature-dependent case.

The slightly elevated temperature in the hot spot region in the temperature dependent case may also be seen in the temperature plots (along the axis of symmetry from the wedge to the outer edge of the stator) in Fig. 2.10, the temperature is in turn lower in the slot region near the back iron.

Simplified slot model

The modelling depth of a detailed slot model may not be appropriate if it is to be integrated into the model of a complete machine since the number of elements in the overall mesh might exceed acceptable limits. A feasible alternative to the generally demanding analysis of a detailed slot model is the modelling of a slot by a single body with uniform material properties. This simplification targets at achieving a similar accuracy with a significantly decreased model complexity.

The possible loss of information and accuracy is studied by using the detailed slot model, merging the bodies inside the slot and using the parameters from the previ-

ous analyses, in particular the same resulting total losses (193 $\frac{W}{m}$). In the simplified model, the losses are defined as a spatially uniform loss density in the complete slot area, exclusive of the slot liner.

With the data in Table 2.6 the average thermal conductivity ($\lambda_{av} = 0.466 \frac{W}{mK}$) is determined by combining the specific thermal resistivities on the basis of the volume of each component in the slot.

The single body representation of the slot significantly reduces the number of elements, in this case down to 41 200 elements (less than 2 % of the detailed model) with similar meshing parameter. The mesh of the simplified slot model and the resulting temperature distribution are shown in Figs. 2.8(b) and 2.9(c) respectively. The values of the minimum, the maximum and the average temperature may be compared with the results of the detailed slot study in Table 2.7.

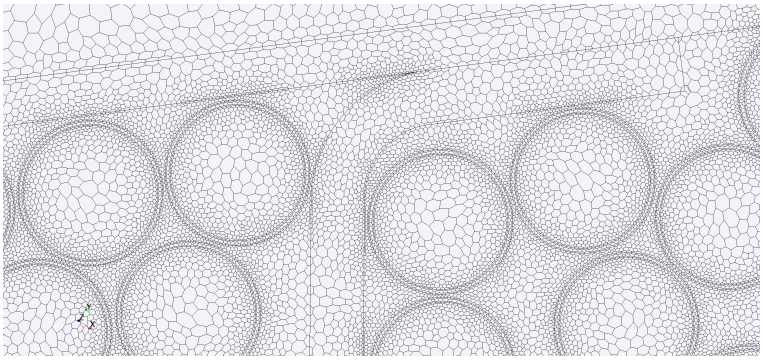

(a) Close-up view of the mesh of the detailed slot model.

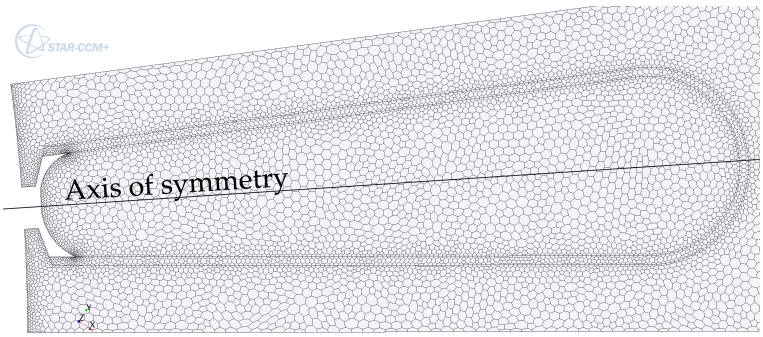

(b) Close-up view of the mesh of the simplified model.

Figure 2.8: Meshed representations of the slot models.

The average temperatures in the slot and in the stator part are 116.6 °C and 89.7 °C, respectively. The average temperatures therefore match the values of the detailed model remarkably well, especially when considering the substantial reduction in the modelling depth.

A certain loss of accuracy is related to the structures of the bodies. The loss of information concerning the copper cross-sections with their comparably high ther-

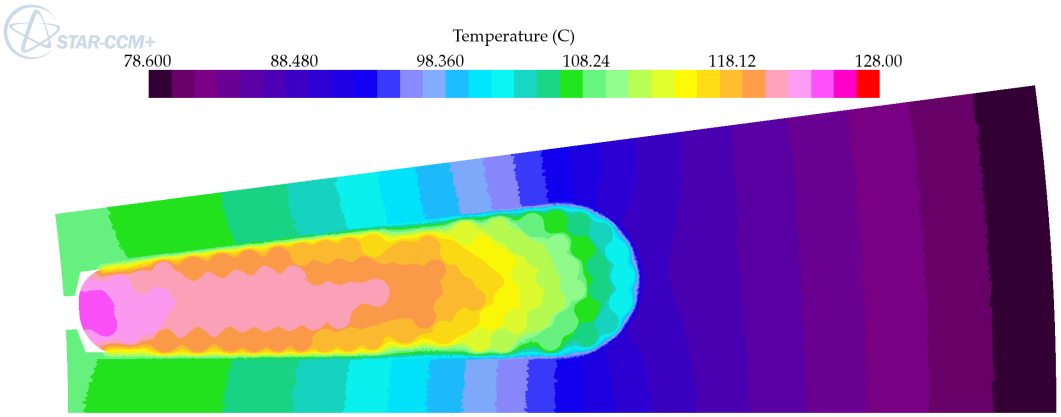

(a) Detailed slot model with temperature-dependent copper loss density (unsmoothed).

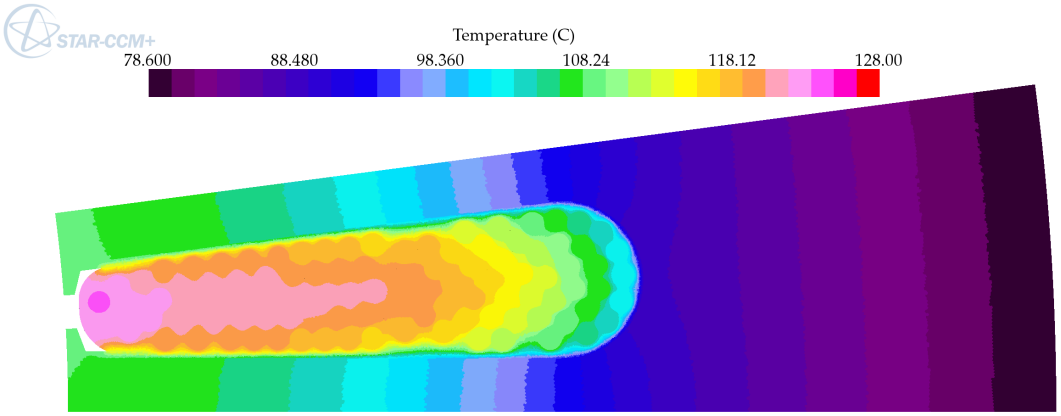

(b) Detailed slot model with spatially uniform copper losses (unsmoothed).

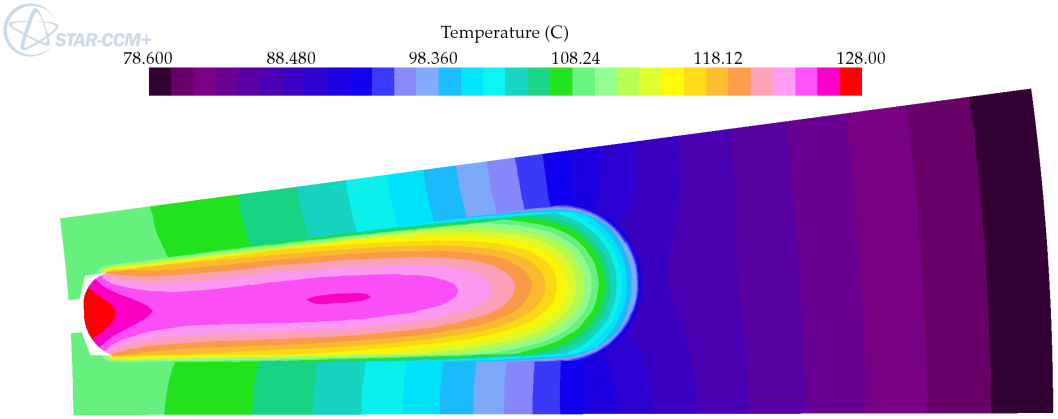

(c) Simplified slot model with spatially uniform slot losses.

Figure 2.9: Temperature distributions (with identical total slot losses).

Table 2.7: Computed temperatures corresponding to Fig. 2.9.

Model		**Temperature / °C**	
		Slot	Stator
Detailed slot model, temp.-dep. losses (Fig. 2.9(a))	min.	88.2	78.7
	max.	**123.8**	108.5
	av.	114.8	89.6
Detailed slot model, uniform losses (Fig. 2.9(b))	min.	88.2	78.7
	max.	**123.4**	108.4
	av.	114.7	89.6
Simplified slot model, uniform losses (Fig. 2.9(c))	min.	88.1	78.7
	max.	**127.7**	108.9
	av.	**116.6**	89.7

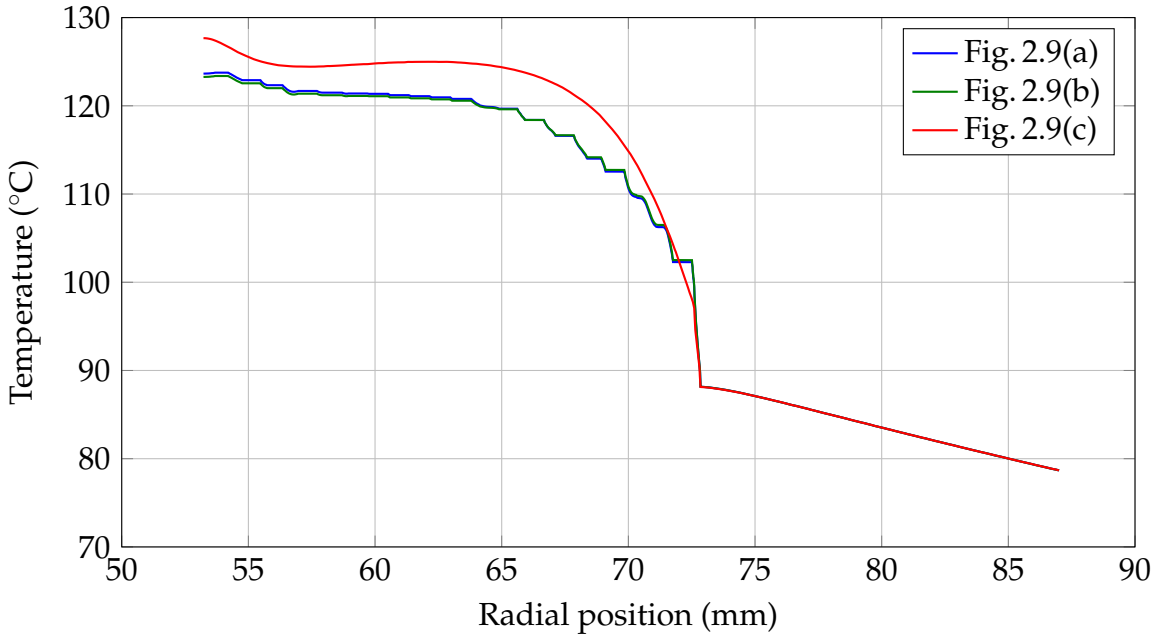

Figure 2.10: Temperatures along the axis of symmetry (mid-line) in radial direction for the three cases shown in Fig. 2.9.

mal conductivity, in particular, leads to noticeable deviations in the simulated temperature distribution. The difference between the detailed model (with a constant temperature in each copper cross section and distinct temperature steps to the next wire) and the simplified model (with a smooth temperature profile) may be seen very clearly in Fig. 2.10.

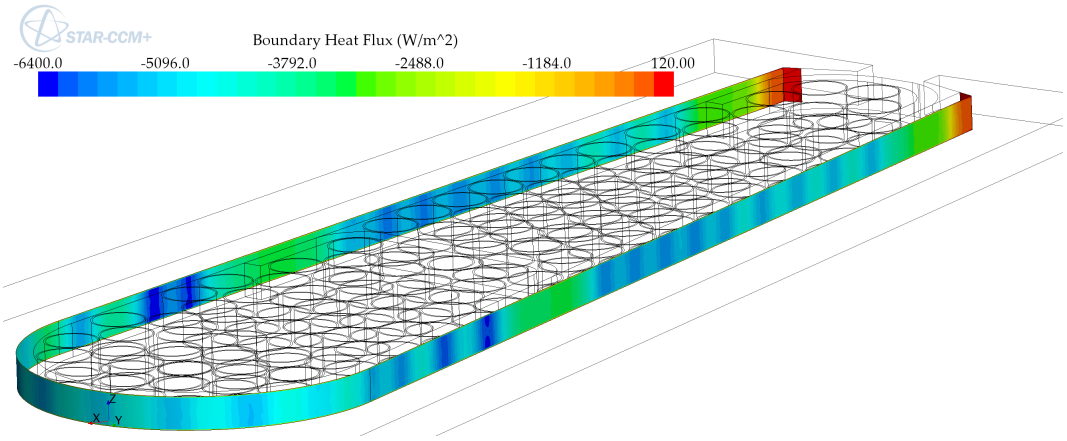

(a) Detailed slot model with uniform losses (Fig. 2.9(b))

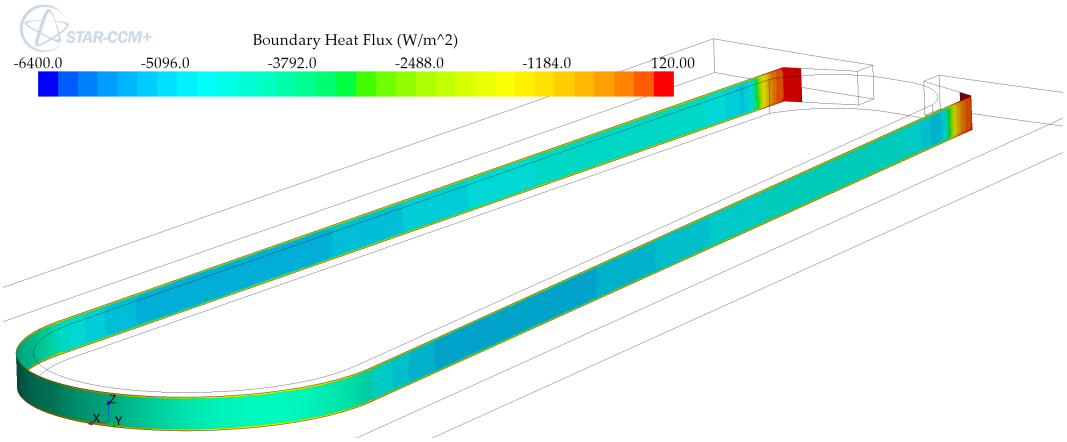

(b) Simplified model (Fig. 2.9(c))

Figure 2.11: Heat flux distributions at extruded interfaces between slot liner and stator stack.

The simplified slot model with uniform properties leads to a slight overestimation of the maximum temperature at the top of the slot (+4.3 K). The average slot temperature is 1.9 K higher than in the corresponding detailed model with uniform losses. The temperature in the tooth and particularly in the back iron region is, however, hardly affected by the slot modelling. It is apparent from in Fig. 2.10 that the temperatures of all three models are practically identical in the back iron region and very similar in the tooth region.

The positive values of the boundary heat fluxes between the liners and the stators at the tooth tops in Fig. 2.11, which are equivalent to minor heat transfers into the slot liners, are due to the injected heat at the tooth tops. Furthermore, the resulting heat flux distribution at the interface to the stator reflects the placement of the wires, the separator and the wedge on the other side of the slot liner, leading to a non-uniform heat flux distribution (Fig 2.11(a)). Even in the simplified case, the heat flux

is not entirely uniform but reaches the maximum just before the tooth region leads into the back iron region (Fig 2.11(b)).

Based on the comparison of the temperature plots in Figs. 2.9 and 2.10 and with the values given in Table 2.7, it may be argued that the simplified numerical model succeeds in approximately determining the position of the hotspots and gives approximately the correct average temperature.

Summary

In conclusion, the significant reduction in the model complexity (by not modelling the wires and the slot insulation explicitly) should in most study contexts outweigh the loss of accuracy in the local temperature distribution, particularly since the average temperatures and the location of the hotspots may nonetheless be determined with a sufficient level of accuracy.

2.3.6 Analytic modelling

In [74], the unidirectional heat flow through windings consisting of round enamelled wires is analysed analytically and simplified equations are derived in order to model the heat flow across such windings. The provided simplified equations for the equivalent thermal conductivity through regular (Fig. 2.12(a)) and shifted layers (Fig. 2.12(b)) are given in terms of the wire copper diameter d_{co}, the overall wire diameter d_{wire} and the thermal conductivity of the impregnating resign λ_{imp} (which is assumed to be identical with the thermal conductivity of the wire insulation).

(a) Regular layers (b) Shifted layers

Figure 2.12: Wire arrangements used in [74] to determine the equivalent thermal conductivity.

With the given model properties (Table 2.6), the equivalent average thermal con-

ductivities λ_{av} for the regular (a) and the shifted (b) layers are [74]

$$\text{(a)}\ \lambda_{av} \approx \lambda_{imp} \left(\frac{d_{co}}{d_{wire} - d_{co}} \right)^{2/3} = 1.16 \frac{W}{m\,K} \text{ and} \tag{2.27}$$

$$\text{(b)}\ \lambda_{av} \approx 1.45\,\lambda_{imp} \left(\frac{d_{co}}{d_{wire} - d_{co}} \right)^{3/4} = 1.94 \frac{W}{m\,K}. \tag{2.28}$$

The numerical simulation of the slot model with both parameters yields average slot temperatures of 112 °C (a) and 110 °C (b). The simulation with the simple volumetric average thermal resistance therefore matches the average temperature of the detailed model better than the simulation with the values calculated with Eq. (2.27) and (2.28), possibly due to the random wire placement and the the two-dimensional flow.

In [7], the following (different) equation is provided to approximate the average thermal conductivity of the assembly in Fig. 2.12(a)

$$\lambda_{av} \approx \lambda_{imp} \left(\frac{d_{co}}{d_{wire} - d_{co}} + \frac{d_{wire} - d_{co}}{d_{wire}} \right) = 2.79 \frac{W}{m\,K}. \tag{2.29}$$

The computed value slightly exceeds the values in Eqs. (2.27) and (2.28) and results in an average slot temperature of 110 °C with the simplified numerical slot model.

The comparison between the results from the detailed numerical slot model and the simplified numerical slot model allows to iteratively determine the optimum (*calibrated*) value for the average thermal conductivity (by subsequent simulations with the simplified numerical slot model). Telling from the previous results, the optimum value of λ_{av}, which would lead to the same average slot temperature in the detailed and in the simplified numerical model, lies between the volumetric average value ($0.466 \frac{W}{m\,K}$) and the value computed with Eq. (2.27).

The validity of the equations for the average thermal conductivity has been verified or compared with the actual detailed and simplified numerical model of the slot. In the frame of thermal lumped parameter modelling, the task of finding an equivalent lumped thermal conductivity is linked to the task of adequately modelling the conductive heat flow path or paths between the wires and the (interface to the) stator. Typically, the complex slot shape and also the teeth are approximated by standard geometric shapes such as rectangles.

In [72], the slot shape is approximated by a rectangular shape and analytic results published in [1] are used to derive the corresponding thermal resistance between the coil sides node and the stator teeth node. The transfer of heat between the slot and the yoke is neglected. The thermal resistance of the teeth is calculated by integrating the thermal resistance per unit length in radial direction along the tooth from the

tooth root to the tooth top. The same modelling approach is used in [42] and consequently in [53]. [3], by contrast, uses a simplified rectangular tooth shape, arguing that an accurate analytic integration does not significantly improve the accuracy.

In [7], the direct transfer of heat between the stator slot to the teeth is also neglected and a rectangular slot shape is used to derive the analytic solution of heat transfer through the assumed rectangular slot with uniform internal heat generation. The resulting model is similar to the approach mentioned in Sec. 1.5.3, using a slight negative thermal resistance in order to correct the otherwise elevated average temperature.

In [71] the slot is modelled by an equivalent quadratic slot containing an inner quadratic copper body, which is surrounded by an outer quadratic body with average properties of the insulation and the voids in the impregnation. Heat transfer from the copper body to the surrounding insulation body is assumed through all four sides and the calculated thermal resistance is scaled by a factor to presumably account for the distributed heat generation. Heat conduction from the surrounding body to the stator tooth node is modelled through three surfaces (slot sides and bottom to the back iron).

The above mentioned approaches, which aim at modelling the transfer of heat between the average slot temperature and the average tooth temperature, may all be represented by the thermal lumped parameter model in Fig. 2.13(a). The average temperatures ϑ_2 and ϑ_4 permit to connect the model to resistances in axial direction and to connect lumped thermal capacitances to model the transient behaviour (Sec. 1.5.2).

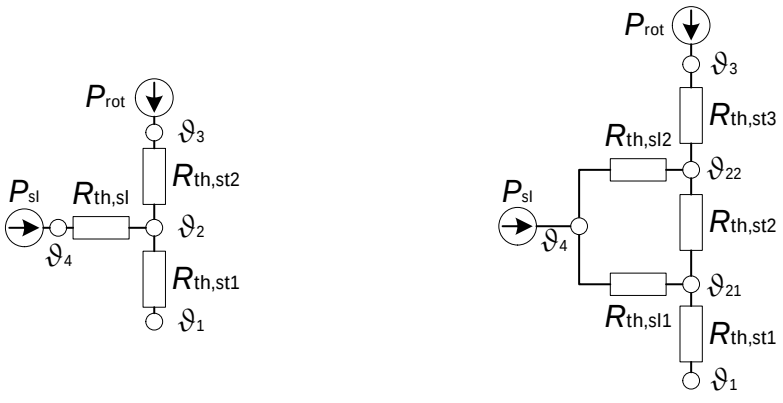

(a) Simple model (b) Extended model

Figure 2.13: Lumped parameter models of slot and stator stack.

For the sake of consistency and with regard to the numerical analysis in Sec. 2.3.5, a loss source (P_{rot}) is connected to the tooth top, modelling the heat flux from the

rotor. P_{sl} denotes the copper losses in the slot, $R_{th,sl}$ the equivalent thermal resistance between the node of average slot temperature and the tooth node. $R_{th,sl}$ may be determined with one of the above mentioned approaches and comprises several thermal resistances to the stator teeth, including the copper coil sides, the wire and the slot insulation, the impregnating resin and possibly voids in the impregnation. $R_{th,st1}$ is the thermal resistance from the outer yoke surface to the tooth node, $R_{th,st2}$ is the thermal resistance from the tooth node to the air gap.

Furthermore, an extended thermal model may be derived from [3, 75]. In [3] the iron losses in the stack are not assigned to one stator stack node but are injected into separate nodes for the teeth and the back iron. In [75] the direct heat flow path between the slot and the back iron is included in these considerations. Consequently the extended slot model in Fig. 2.13(b) may also be used to model the slot analytically. $R_{th,sl1}$ and $R_{th,sl2}$ denote the thermal resistances between the slot and the yoke and between the slot and the tooth, respectively. $R_{th,st1}$, $R_{th,st2}$ and $R_{th,st3}$ are the thermal resistances from the outer yoke surface to the yoke node, from the yoke node to the tooth node and from the tooth node to the interface to the air gap.

All above mentioned analytic approaches are approximations since exact analytic solutions are difficult to obtain for the complex two-dimensional flow and do generally not allow for a direct inclusion in lumped parameter models.

Typically, the analytic models are not compared with numerical simulations, that may serve to verify the analytic approaches. Therefore, two lumped parameter models similar to the models in Fig. 2.13 are developed and compared with the numerical model in Sec. 2.3.5, using the parameters given in Table 2.6. The same slot losses ($193\,\frac{\mathrm{W}}{\mathrm{m}}$) and the same uncalibrated average thermal conductivity ($0.466\,\frac{\mathrm{W}}{\mathrm{m\,K}}$) as in the simplified numerical model are used in the analytic slot models to permit an easy comparison between the analytic and the numerical results.

Simple slot model

The thermal resistance of the tooth (both tooth halves) in radial direction $R_{th,st10}$ is calculated with the average tooth width according to [3] and Sec. 1.4.1

$$R_{th,st10}\,l = \frac{1}{28\,\frac{\mathrm{W}}{\mathrm{m\,K}}} \cdot \frac{17.24\,\mathrm{mm}}{3.77\,\mathrm{mm}} = 0.163\,\frac{\mathrm{m\,K}}{\mathrm{W}}. \tag{2.30}$$

The thermal resistance of the back iron $R_{th,st11}$ is approximated by a segment of a hollow cylinder (Eq. 1.17)

$$R_{th,st11}\,l = \frac{\ln\left(\frac{174\,\mathrm{mm}}{105.5\,\mathrm{mm}+2\cdot 17.24\,\mathrm{mm}}\right)}{2\pi \cdot 28\,\frac{\mathrm{W}}{\mathrm{m\,K}}} \cdot \frac{360^\circ}{7.5^\circ} = 0.0594\,\frac{\mathrm{m\,K}}{\mathrm{W}}. \tag{2.31}$$

The thermal resistance of the slot liner $R_{\text{th,st12}}$ is approximated by a plane wall, the thickness is the thickness of the slot liner, the length of the contact between the slot liner and the stack is the line contact in the 2D heat conduction problem

$$R_{\text{th,st12}}\, l = \frac{1}{0.12\,\frac{\text{W}}{\text{m K}}} \cdot \frac{0.25\,\text{mm}}{33.1\,\text{mm} + 8.59\,\text{mm}} = 0.0500\,\frac{\text{m K}}{\text{W}}. \tag{2.32}$$

The thermal resistance $R_{\text{th,st13}}$ between the outer yoke edge and the ambient temperature ϑ_1 in Fig. 2.13(a) is calculated with Eq. (1.22)

$$R_{\text{th,st13}}\, l = \frac{1}{1000\,\frac{\text{W}}{\text{m}^2\,\text{K}} \cdot \pi \cdot \frac{7.5°}{360°} \cdot 174\,\text{mm}} = 0.0878\,\frac{\text{m K}}{\text{W}}. \tag{2.33}$$

The slot is modelled similarly to [7] in that the assumed uniform internal heat generation is modelled with the approach mentioned in Sec. 1.5.3. In the simple slot model approach heat is only transferred to the tooth node. In contrast to [7], the heat transfer is, nonetheless, assumed across the complete contact length between the stack and the slot liner and not only at the interface between slot liner and teeth. The thermal resistance between the slot node and the slot liner $R_{\text{th,st14}}$ may then be estimated roughly with

$$R_{\text{th,st14}}\, l = \frac{1}{0.466\,\frac{\text{W}}{\text{m K}}} \cdot \frac{\frac{2}{3} \cdot \frac{4.33\,\text{mm}}{4}}{41.69\,\text{mm}} = 0.0371\,\frac{\text{m K}}{\text{W}}. \tag{2.34}$$

$\frac{1}{4}$ of the equivalent slot width is used to determine the resistance to the node of average slot temperature due to symmetry [7] and the factor $\frac{2}{3}$ is due to the mentioned correction of heat conduction with assumed uniform internal heat generation (Sec. 1.5.3).

If the slot node is connected to the mid-point of the teeth resistance, i.e. between $\frac{1}{2}R_{\text{th,st10}}$, the thermal resistances in Fig. 2.13(a) are

$$R_{\text{th,st1}}\, l = R_{\text{th,st13}}\, l + R_{\text{th,st11}}\, l + \frac{1}{2}R_{\text{th,st10}}\, l = 0.229\,\frac{\text{m K}}{\text{W}}, \tag{2.35}$$

$$R_{\text{th,st2}}\, l = \frac{1}{2}R_{\text{th,st10}}\, l = 0.0817\,\frac{\text{m K}}{\text{W}}, \text{and} \tag{2.36}$$

$$R_{\text{th,sl}}\, l \;\; = R_{\text{th,st12}}\, l + R_{\text{th,st14}}\, l = 0.0871\,\frac{\text{m K}}{\text{W}}. \tag{2.37}$$

Solving the lumped parameter network with the specified loss sources and the reference temperature $\vartheta_1 = 60\,°\text{C}$ yields

$$\vartheta_2 = 109\,°\text{C}, \tag{2.38}$$

$$\vartheta_3 = 110\,°\text{C}, \text{ and} \tag{2.39}$$

$$\vartheta_4 = 126\,°\text{C}. \tag{2.40}$$

The temperature at the tooth root is in this case 91.4 °C.

By contrast, if the slot is connected to the tooth root, the thermal resistances are

$$R_{\mathrm{th,st1}}\, l = R_{\mathrm{th,st11}}\, l + R_{\mathrm{th,st13}}\, l = 0.147\, \frac{\mathrm{m\,K}}{\mathrm{W}}, \tag{2.41}$$

$$R_{\mathrm{th,st2}}\, l = R_{\mathrm{th,st10}}\, l = 0.163\, \frac{\mathrm{m\,K}}{\mathrm{W}}, \text{and} \tag{2.42}$$

$$R_{\mathrm{th,sl}}\, l \;\; = R_{\mathrm{th,st12}}\, l + R_{\mathrm{th,st14}}\, l = 0.0871\, \frac{\mathrm{m\,K}}{\mathrm{W}}. \tag{2.43}$$

The corresponding temperatures are ($\vartheta_1 = 60\,^{\circ}\mathrm{C}$)

$$\vartheta_2 = 91.3\,^{\circ}\mathrm{C}, \tag{2.44}$$

$$\vartheta_3 = 94.6\,^{\circ}\mathrm{C}, \text{ and} \tag{2.45}$$

$$\vartheta_4 = 108\,^{\circ}\mathrm{C}. \tag{2.46}$$

It is apparent from the two different cases, that the position where the heat source is connected to the stator part highly affects the temperatures of all model components.

In the first case, the total slot losses are connected to the mid-point of the tooth and therefore flow through $\frac{1}{2}R_{\mathrm{th,st10}}$. ϑ_3 matches the numerical results fairly well (1 K difference), whereas the average slot temperature exceeds the numerical value significantly by 9 K.

In the second case, the slot losses are connected to the tooth root, which leads to a significant underestimation of the slot temperature (-9 K) compared with the numerical analysis). ϑ_3 differs even more (-14 K) due to the fact that hardly any heat flows through the comparably high thermal tooth resistance because of the position of the heat injection from the slot.

Extended slot model

The parameters of the extended lumped parameter in Fig. 2.13(b) model may be derived similarly. The same models are used for $R_{\mathrm{th,st10}}$, $R_{\mathrm{th,st11}}$ and $R_{\mathrm{th,st13}}$. $R_{\mathrm{th,st12}}$ and $R_{\mathrm{th,st14}}$ are split into separate thermal resistances to the back iron and the tooth according to the line contact lengths in Table 2.6.

With this choice, the combined thermal resistance $R_{\mathrm{th,sl1}}$ between the slot node and the yoke is

$$R_{\mathrm{th,sl1}}\, l = \frac{41.69\,\mathrm{mm}}{8.59\,\mathrm{mm}} \cdot \left(R_{\mathrm{th,st12}} + R_{\mathrm{th,st14}}\right) = 0.423\, \frac{\mathrm{m\,K}}{\mathrm{W}}. \tag{2.47}$$

The combined thermal resistance $R_{\text{th,sl2}}$ between the slot node and the tooth is

$$R_{\text{th,sl2}}\, l = \frac{41.69\,\text{mm}}{33.1\,\text{mm}} \cdot (R_{\text{th,st12}} + R_{\text{th,st14}}) = 0.110\,\frac{\text{m K}}{\text{W}}. \tag{2.48}$$

The stator resistances are

$$R_{\text{th,st1}}\, l = R_{\text{th,st11}}\, l + R_{\text{th,st13}}\, l = 0.147\,\frac{\text{m K}}{\text{W}} \text{and} \tag{2.49}$$

$$R_{\text{th,st2}}\, l = R_{\text{th,st3}} = \frac{1}{2} R_{\text{th,st10}}\, l = 0.0817\,\frac{\text{m K}}{\text{W}}. \tag{2.50}$$

Solving the lumped parameter network with the specified loss sources and the reference temperature $\vartheta_1 = 60\,^\circ\text{C}$ yields

$$\vartheta_{21} = 91.3\,^\circ\text{C}, \tag{2.51}$$

$$\vartheta_{22} = 104\,^\circ\text{C}, \tag{2.52}$$

$$\vartheta_3 = 105\,^\circ\text{C}, \text{ and} \tag{2.53}$$

$$\vartheta_4 = 118\,^\circ\text{C}. \tag{2.54}$$

The approach to model two separate heat flow paths from the slot to the tooth and directly to the yoke leads to results that better match the (accurate) numerical results. This is due to the fact that it accounts for the direct transfer of some heat to the cooler back iron, as may be seen in Fig. 2.11. The average slot temperature is 118 °C compared with 117 °C in the numerical analysis, the temperature at the tooth tip is 105 °C compared with 109 °C.

Layered slot model

The presented winding models aim at modelling the average component temperatures for direct inclusion in a lumped parameter model of an electric machine. In order to allow for the modelling of the maximum slot temperature—which is, for instance, relevant for the ageing of the insulating materials—the slot models may be extended as presented in [46,62,76,77]. In these publications, the slot is modelled by several (virtual) layers of copper and insulating material. These layers correspond to thermal resistances (connected in series) between the interface to the stator and the hot spot in the winding.

The basic concept of the layered model approach is illustrated in Fig. 2.14. The actual slot assembly (Fig. 2.14(a)) is not treated as one uniform body but instead as several equivalent layers (Fig. 2.14(b)).

$R_{\text{th,1}}$ in Fig. 2.14(b) in this simple model comprises the thermal resistance between the interface to the stator stack and the slot insulation (i.e. slot liner and air pockets

due to a non-ideal impregnation) as well as thermal resistances corresponding to the first insulation layer and one half of the first copper layer. $R_{th,2}$ comprises one half of the first copper layer, the second insulation layer and one half of the second copper layer. ϑ_1 is consequently the temperature at the interface to the stator stack (The heat flow from the slot to the teeth and the back iron region is not separated in this exemplary model.), ϑ_2 is the copper temperature of the first copper layer and ϑ_3 is the copper temperature of the second copper layer and the expected hot spot temperature in this example.

(a) Slot assembly (b) Layer model

Figure 2.14: Schematic illustration of the layered slot modelling approach.

The layered approach is more complex compared with the single body approach as it requires correct definitions of the number of layers, the layer thicknesses and the corresponding loss injections, which also need to be validated and might also vary for different slot shapes.

Moreover, it should be noted that the maximum slot temperature node from a layered model (ϑ_3 in this example) should not be used as the average slot node which is then connected to the end windings. In [46, 76] the average temperature node, which is calculated from the layered model, is consequently connected to the overall machine model. The authors in [62, 77] propose to use the different copper layers also for the modelling of parallel axial heat transfer to the end windings. This approach is, however, combined with a simplified end winding modelling. Further research is required in that field in order to evaluate potential benefits of this more complex approach.

Additionally, it may also be noted that the single body representation also generally allows to approximate a maximum slot temperature in addition to the average temperature by, in simple terms, considering the heat flow path in the average slot material from the average temperature region to the hot spot region in the centre of the slot.

Summary

Different models may be derived to model heat transfer between the slot and the stator stack. Since even simplified analytic expressions of the complex 2D heat transfer are difficult to derive [1,75] (in reality the heat flow problem is of three-dimensional nature due to possible axial heat flow), simplified approaches are used to model the different components in the slot and the heat flow paths. The validity of such lumped parameter models may be verified by numerical simulations.

The iron losses may be modelled by concentrated losses that are connected to the corresponding node of the lumped parameter model. Separate loss sources for the iron losses in the tooth region and in the yoke region seem advisable.

Coupled electromagnetic and thermal FEM simulations may be used to study the heat transfer problem in greater detail and to validate derived analytic models. In particular if the effects of iron losses (e.g. their spatial distribution) and for instance proximity losses are to be investigated, detailed numerical analyses are required.

Thermal capacitances may be connected to the nodes that (approximately) give the average component temperature in order to model the thermal behaviour. Due to the expected difference between the average tooth temperature and the average temperature of the back iron (Fig. 2.9), it may be advisable to use separate thermal capacitances as the lumped capacitances approach is based on the assumption of a constant uniform temperature in the corresponding component (Sec. 1.5.2).

2.4 Rotor

Generally, the thermal analysis of the rotor does not differ significantly from the analysis of the stator. Depending on the motor type, the rotor is made of just the same stacked electric steel sheets (as in the case of switched reluctance or synchronous reluctance motors) or it may also comprise magnets or a rotor winding.

Induction machines—whose modelling is discussed and verified by a case study in Chapter 3—typically have a (copper or aluminium) rotor cage winding, where just one solid conductor is placed in each slot instead of multiple insulated wires and various insulating components. Additionally, solid end rings are used instead of the impregnated winding overhang in the end cap regions.

Consequently, the rotor cage winding may be treated similarly to the stator winding. Since the bars and the end rings are already bodies with uniform material properties, it is not required to model the slots and the end rings as simplified single bodies with average material properties.

Surface-mounted permanent magnet motors, to give another example, may be re-

garded as a serial connection of the thermal resistance of the rotor stack and the magnet to the air gap. Buried magnets, by contrast, need to be treated as heat flow paths parallel to heat transfer in the rotor stack. Analytic approaches for certain magnet arrangements, such as a layered cylindrical approach in [53]—which is based on the assumption of solely radial heat flow—may be validated by numerical models as shown in the preceding sections.

Special care needs to be taken, however, when comparing analytic and numerical models since numerical models typically also incorporate simplifications. One example being the detailed slot modelling which still uses perfect wire and wire insulation geometries (which vary in reality) and which does not explicitly model the imperfections in the impregnation. The resulting spatial temperature distribution may therefore also be regarded as an approximation similar to the analytically determined results.

In summary, the same or even simplified analytic approaches as well as generally the same numerical software tools, which are used for the thermal modelling of the stator (Sec. 2.3), may be used for the analysis of the rotor.

The calculation of the losses is more specific to the exact motor type than the thermal simulation. An analytic loss model is developed for the induction machine and compared with the losses calculated numerically in Chapter 3. Similar approaches may be followed for other machine types.

2.5 Air gap

The modelling of the air gap is analysed with the slot model provided in Fig. 2.7 in Sec. 2.3. The additional parameters, which are specific to the air gap, are given in Table 2.8. Constant and identical thermal properties are used in all simulations and in all analytic calculations in order to ensure comparability. The effect of temperature-dependent material properties on both models, which e.g. requires iterative analytic calculations, may be investigated in a follow-up study based on the results of this first analysis.

The rotor—which is only partly shown in the figure—serves as the boundary to the air gap, specifying the boundary conditions, i.e. the rotational speed and the heat flux to the air gap at the interface. The actual rotor geometry and its thermal properties are therefore not required.

Table 2.8: Additional air gap specific parameters at 115 °C and 1 atm [37].

Parameter	Value	Unit
Thermal conductivity	$3.29 \cdot 10^{-2}$	$\frac{\mathrm{W}}{\mathrm{m\,K}}$
Kinematic viscosity	$2.51 \cdot 10^{-5}$	$\frac{\mathrm{m}^2}{\mathrm{s}}$
Prandtl number	0.693	1
Specific heat	1 013	$\frac{\mathrm{J}}{\mathrm{kg\,K}}$
Rotational speed	1 500	$\frac{1}{\mathrm{min}}$
	9 000	
	15 000	

2.5.1 Numerical air gap modelling

In contrast to the adiabatic boundaries at the sides of the stator, the boundaries of the air gap are defined as internal periodic boundaries in order to allow mass flow and heat transfer across the boundaries and to account for symmetry.

Polyhedral elements are used in both the solid and the fluid domain with additional prismatic layers in the fluid domain at the boundaries to the contacting solids.

The surfaces are defined as smooth surfaces and radiation is neglected as the typical temperature differences between the stator and the rotor surfaces likely cause limited radiative heat exchange.

Comparison with slot model without air gap

The first of two air gap studies is based on the numerical analysis of the detailed slot model and of the simplified slot model with constant loss densities (Figs. 2.9(b) and 2.9(c)).

By using similar conditions as in the previous slot models, it is intended to allow for an evaluation of the effect of the air gap on the temperature distribution inside the slot. When using FEM software without CFD capabilities in thermal studies, for instance, a simulation of the convective heat transfer between the slot and the teeth to the air gap is not possible. Since the velocity of the air near the slot wedge is expected to be nearly zero (Fig. 2.17) and due to the comparably low thermal conductivity of air (Table 2.8), the simplest approach may be to model the convective heat transfer from the teeth to the air gap (by using an averaged heat transfer coefficient or a lumped thermal resistance to the rotor) and to neglect a potential heat transfer from the slot to the air gap. This approach is similar to the study without

the air gap, where heat is injected into the stator teeth.

The same loss inputs and the same reference temperature are used with the difference that the heat injection from the rotor side ($20\,\frac{\mathrm{W}}{\mathrm{m}}$) is no longer injected at the tooth surfaces but at the interface from the rotor to the air gap. Additionally, the velocity of the air at the boundary to the rotor is defined by the rotational speed $n = 9000\,\frac{1}{\mathrm{min}}$.

The coupled thermal and fluid dynamics problem is solved for the detailed and the simplified slot model and it is compared with the simplified slot model without modelled air gap in Fig. 2.15. The minimum, maximum and average temperatures are compared in Table 2.9.

Similar to the case without air gap, the average and the maximum slot temperature are slightly higher in the lumped model (+1.7 K and +3.9 K). This also leads to marginally elevated average and maximum air temperatures compared with the detailed model (+0.8 K and +0.5 K respectively).

More importantly, a hot spot is located in the vicinity of the slot wedge in the slot models without the air gap (Fig. 2.15(c)). Despite the comparably low thermal conductivity of air and the expected low velocities near the slot wedge, the hotspots are *removed* in the models including the air gap, which allows the transfer of heat between the slot and the air. The heat transfer from the top of the slot to the inner air is apparent from the negative values in the corresponding region in Fig. 2.16.

Therefore, the aforementioned approach to solely model heat transfer between the rotor and the stator teeth and to neglect heat transfer from the slot to the air gap influences the temperature distribution inside the slot, in particular the hot spots. The average temperature is, however, hardly affected.

Air gap without heat generation in the slots

In order to study the air gap and the effect of different rotational speeds on the temperature drop across the air gap in greater detail without the presence of secondary effects, the additional heat source in the slot is set to zero.

Vector plots of the velocity and scalar scenes of the temperature inside the air gap are shown for the three different rotational speeds in Fig. 2.17. The absolute values of the velocities and the temperatures across the air gap along the axis of symmetry of the air gap are illustrated in Fig. 2.18.

The simulated average temperatures at both interfaces (ϑ_1: average interface temperature to rotor, ϑ_2: average interface temperature to stator, slot liner and slot), the overall average temperature differences $\Delta\vartheta$ and the equivalent thermal resistance $R_{\mathrm{th}}l$ are tabulated in Table 2.10.

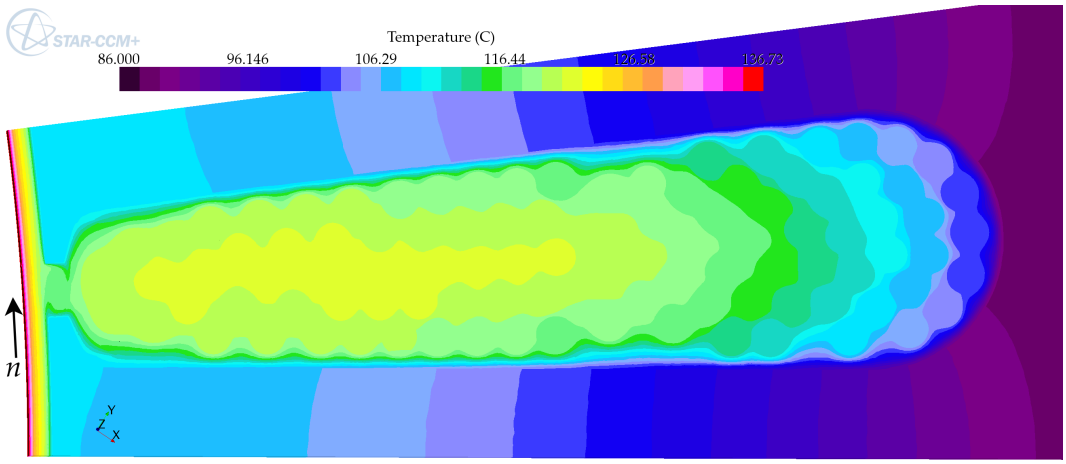

(a) Detailed slot model with air gap ($n = 9000\ \frac{1}{\text{min}}$)

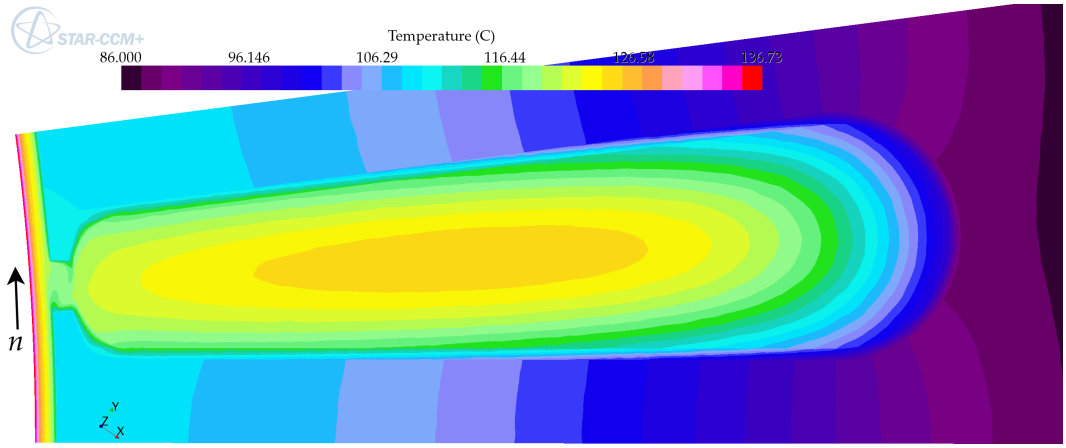

(b) Simplified slot model with air gap ($n = 9000\ \frac{1}{\text{min}}$)

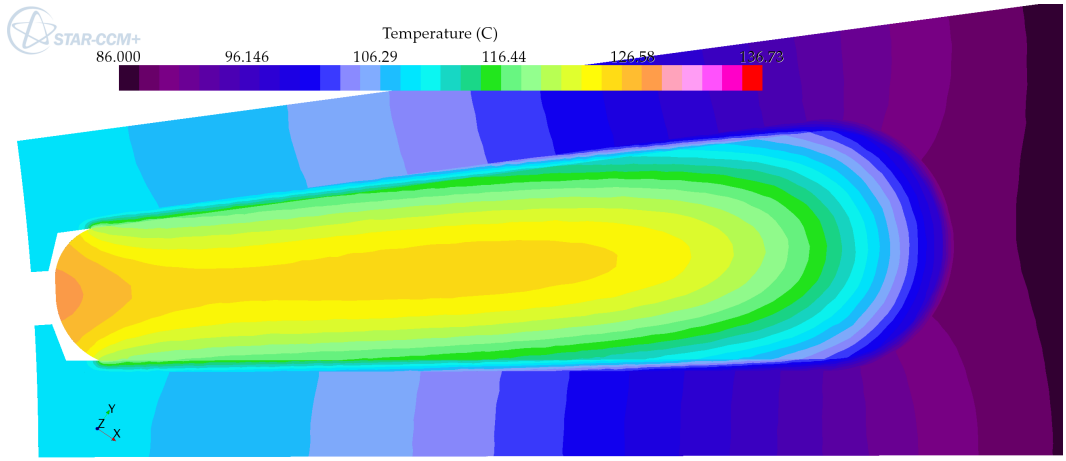

(c) Simplified model without air gap

Figure 2.15: Simulation of the slot model with air gap (with identical total slot losses).

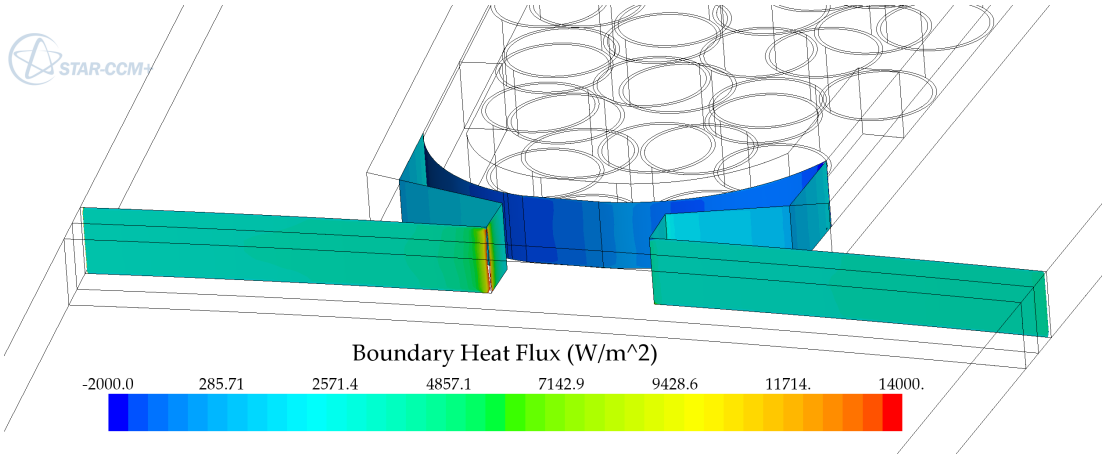

Figure 2.16: Boundary heat flux at extruded interfaces to stator, wedge, and slot liner (corresponding to Fig. 2.15(a)).

Table 2.9: Computed temperatures corresponding to Fig. 2.15.

Model		**Temperature / °C**		
		Slot	Air gap	Stator
Detailed slot model (Fig. 2.15(a))	min.	88.4	108.3	78.8
	max.	**121.4**	136.2	109.7
	av.	**114.8**	120.8	89.9
Simplified slot model (Fig. 2.15(b))	min.	88.3	108.9	78.8
	max.	**125.3**	136.7	110.4
	av.	**116.5**	121.6	90.0
Simplified slot model, no air gap (Fig. 2.15(c))	min.	88.1	—	78.7
	max.	**127.7**	—	108.9
	av.	**116.6**	—	89.7

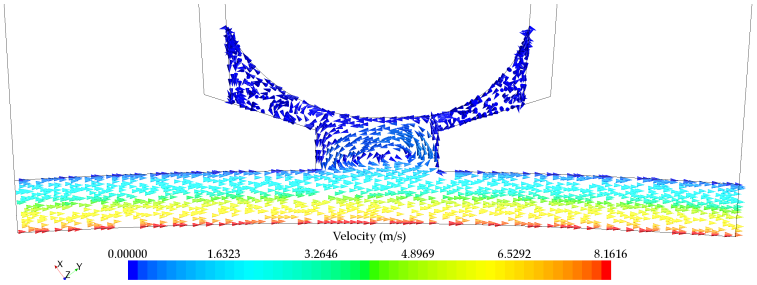

(a) Velocity vectors at $n = 1500\ \frac{1}{\text{min}}$

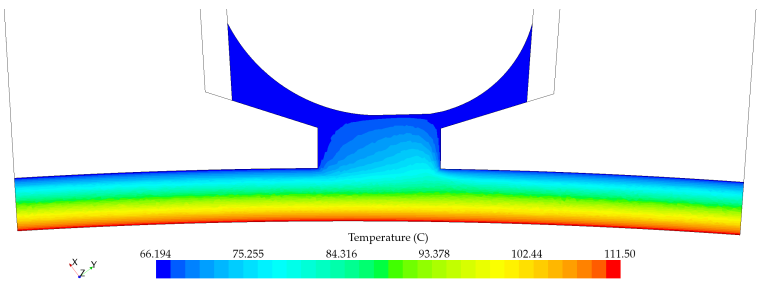

(b) Temperature distribution at $n = 1500\ \frac{1}{\text{min}}$

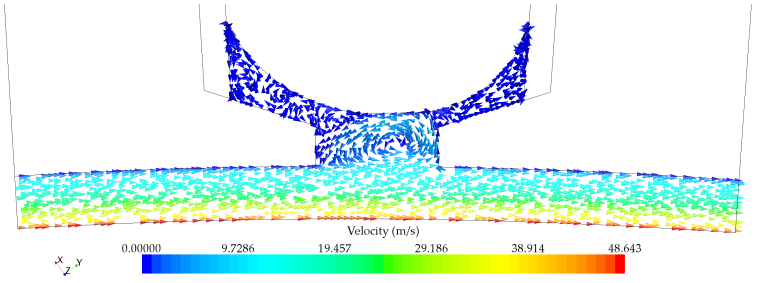

(c) Velocity vectors at $n = 9000\ \frac{1}{\text{min}}$

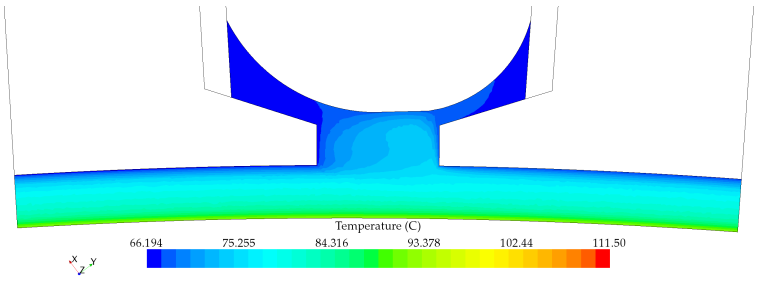

(d) Temperature distribution at $n = 9000\ \frac{1}{\text{min}}$

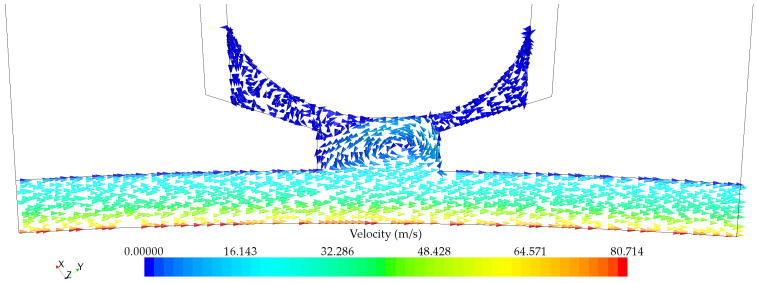

(e) Velocity vectors at $n = 15\,000\ \frac{1}{\text{min}}$

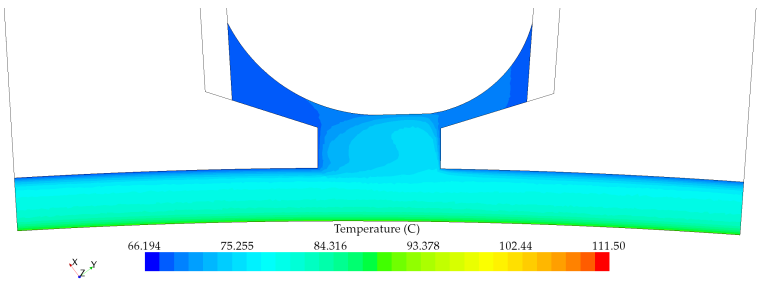

(f) Temperature distribution at $n = 15\,000\ \frac{1}{\text{min}}$

Figure 2.17: Velocity vector plots and temperature fields in the air gap at different rotational speeds.

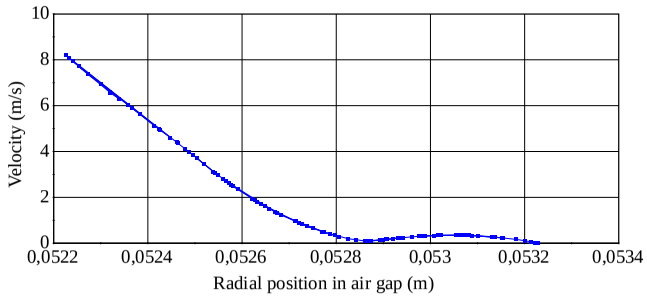

(a) Velocity plot at $n = 1500\ \frac{1}{\text{min}}$

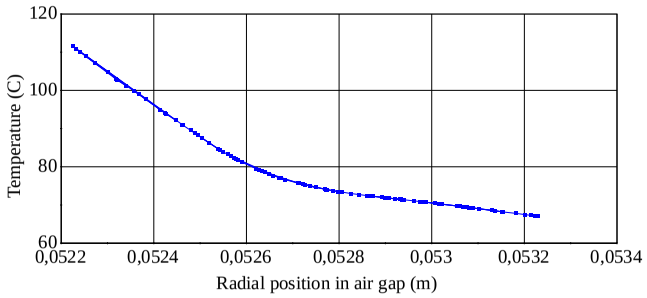

(b) Temperature plot at $n = 1500\ \frac{1}{\text{min}}$

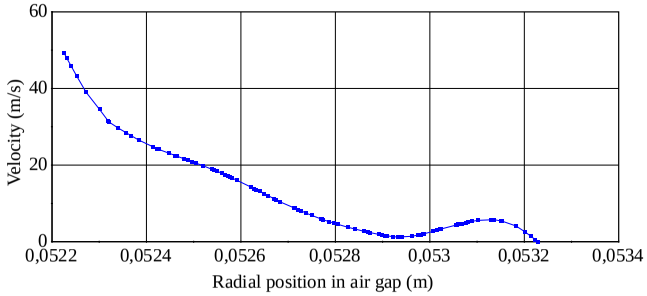

(c) Velocity plot at $n = 9000\ \frac{1}{\text{min}}$

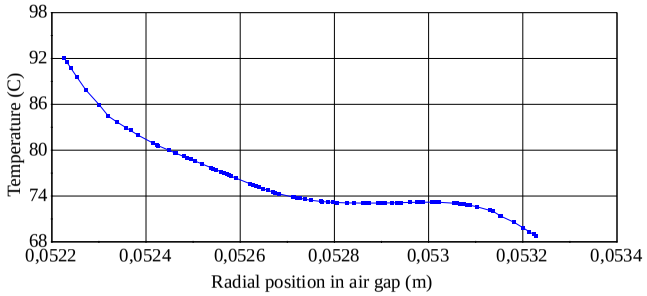

(d) Temperature plot at $n = 9000\ \frac{1}{\text{min}}$

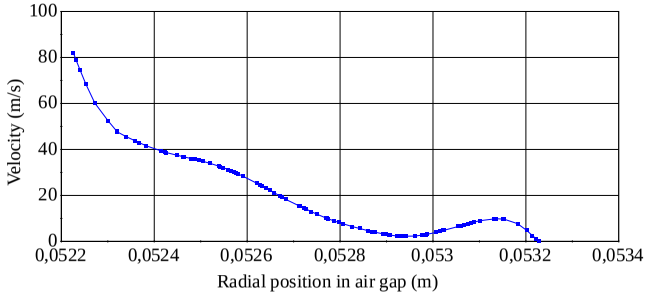

(e) Velocity plot at $n = 15\,000\ \frac{1}{\text{min}}$

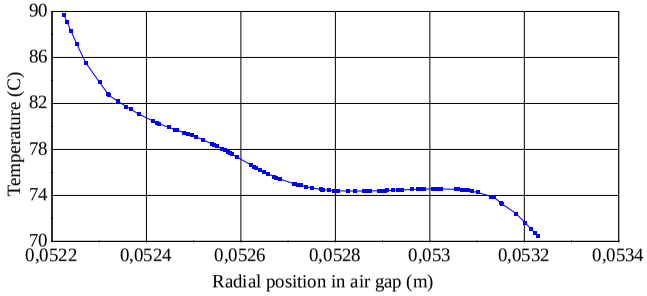

(f) Temperature plot at $n = 15\,000\ \frac{1}{\text{min}}$

Figure 2.18: Velocity and temperature across the air gap along the axis of symmetry.

Table 2.10: Average rotor-to-air gap (ϑ_1) and air gap-to-stator (ϑ_2) interface temperatures, equivalent thermal resistances and generated losses in the air gap.

n / min^{-1}	ϑ_1 / °C	ϑ_2 / °C	$\Delta\vartheta$ / K	$R_{\mathrm{th}}l$ / ($\frac{\mathrm{K\,m}}{\mathrm{W}}$)	P'_{airGap} / $\frac{\mathrm{W}}{\mathrm{m}}$
1 500	111.5	66.6	44.9	2.25	0.02
9 000	92.1	67.2	24.9	1.25	1.61
15 000	89.7	68.8	20.9	1.05	6.14

It may be seen in Table 2.10 that the average temperature at the interface to the rotor decreases from 112 °C to 90 °C with increasing rotational speed. The average temperature difference between the interfaces consequently also decreases from 45 °C to 21 °C. The corresponding thermal resistances $R_{\mathrm{th}}l$ decrease accordingly.

It may be noted, however, that ϑ_2 increases despite the decrease of both, the thermal resistance and ϑ_2. This may be explained by additional frictional losses that are generated in the air gap. In the simulations the additional losses are 0.1 % ($n = 1\,500\,\frac{1}{\mathrm{min}}$), 8 % ($n = 9\,000\,\frac{1}{\mathrm{min}}$) and 30 % ($n = 15\,000\,\frac{1}{\mathrm{min}}$) of the injected heat from the rotor. It is obvious from the frictional losses, which are also provided in Table 2.10, that the frictional losses may become a significant loss source at higher rotational speeds.

It may also be noted that the calculation of the thermal resistance (the temperature drop across the air gap divided by the heat injected from the rotor) is, strictly speaking, not correct because of the additional internally generated losses, particularly at 15 000 $\frac{1}{\mathrm{min}}$ with an additional 30 % of the injected losses being generated. The calculated thermal resistances are still provided in order to allow for a comparison with the analytically calculated values in Sec. 2.5.2.

Furthermore, eddies may be seen clearly in the tooth tip regions in the detailed velocity vector plots in Figs. 2.17(a), 2.17(c), and 2.17(e), even in the laminar case. The eddies have a noticeable effect on the corresponding temperature distributions (Figs. 2.17(b), 2.17(d), and 2.17(f)).

The effect of the eddies on the velocity, and the reverse current in particular, may be seen clearly in Figs. 2.18(a), 2.18(c), and 2.18(e) by the increasing velocity (in reverse direction) above the radial position at 0.0529 m. Similarly, the effect of the counter-clockwise swirling of the comparably hotter air in this region leads to an approximately nearly constant temperature over a certain radial distance. This may be seen particularly in Figs. 2.18(d), and 2.18(f). However, the air movement, which seemed comparable in Figs. 2.18(a), 2.18(c), and 2.18(e), leads to a rather lin-

ear temperature profile in Fig. 2.18(b) compared with the profiles at $n = 9\,000\,\frac{1}{\text{min}}$ and $n = 15\,000\,\frac{1}{\text{min}}$.

2.5.2 Analytic air gap modelling

Numerous experimental test have been carried out by several authors to study the transfer of heat in the annular flow between concentric cylinders, which are in relative motion to each other, and several correlations have been developed to describe the heat transfer analytically. A review of the heat transfer in a fluid between concentric rotating cylinders may be found in [78]; a more recent review of convection in the air gap of electric machines is provided in [79].

The thermal modelling of the air gap in [36, 49, 72] is based on the sources mentioned in [78, 79]. The results published in [80] are, amongst other sources, used in [71, 81]. The authors in [82–85] determine the thermal resistance with the correlation developed in [86]. Most likely, the different factors in [82, 83] (compared with [84–86]) are due to a chosen value for the thermal conductivity of air (presumably $0.0275\,\frac{\text{W}}{\text{m K}}$) in order to convert the local equivalent thermal conductivity (ratio of the heat transfer by convection to by conduction only), given in [86], into an equivalent thermal conductivity.

The thermal resistance of the air gap in the slot model (specified in Tables 2.6 and 2.8) is computed with the equations provided in [36, 49, 71, 72, 82–85]. The computation of the thermal resistance of the same air gap with the different correlations and equations allows for a comparison of the modelling approaches which is typically not carried out in the frame of thermal studies of electric machines. Furthermore, the computed values are compared with the simulated values (Table 2.10) in Sec. 2.5.3 by comparing the temperature drop resulting from the injected heat at the interface to the rotor. The calculated values are summarised in Table 2.11.

The difference between the computed values according to [84, 85] and [82, 83] is related to the different thermal conductivities that are used.

Using the criterion stated in [49], the flow in may be assumed to be laminar for $n = 1\,500\,\text{min}^{-1}$, turbulent for $n = 15\,000\,\text{min}^{-1}$ and in the transition regime for $n = 9\,000\,\text{min}^{-1}$.

In the laminar case ($n = 1\,500\,\frac{1}{\text{min}}$), the calculated thermal resistances are fairly similar. [36] gives a slightly lower value, while using the thermal conductivity of air at 25 °C results in a higher value with [84, 85].

A notable difference may be seen between [82–85] and the other sources at higher rotational speeds: The thermal resistances determined with [82–85] are significantly lower than the thermal resistances according to [36, 49, 71, 72].

Table 2.11: Computed air gap resistances and temperature drops across the air gap.

Source	$R_{\mathrm{th}} l$ / $(\frac{\mathrm{K\,m}}{\mathrm{W}})$			$\Delta\vartheta$ / K		
	$\frac{n}{\mathrm{min}^{-1}}$: 1 500	9 000	15 000	1 500	9 000	15 000
[49]	2.22	1.30	0.95	44.5	26.1	18.9
[72]	2.22	1.25	0.95	44.5	25.0	19.1
[36]	2.02	1.20	—	40.4	24.1	—
[84, 85]	2.36	0.88	0.66	47.2	17.6	13.2
[82, 83]	2.24	0.83	0.63	44.8	16.7	12.6
[71]	2.20	1.38	—	44.0	27.5	—

2.5.3 Summary

It has been shown that the explicit modelling of the air gap—in contrast to modelling heat flow between the rotor surface and the tooth surfaces to the air gap and implicitly defining an adiabatic boundary at the slot (wedge)—has a noticeable effect on the temperature distribution. Despite the comparably low thermal conductivity of air and the comparably slow air movement near the slot-to-air contact, the existence of the hot spot could not be verified in the model with air gap.

Nonetheless, from the comparison of the average temperatures in Table 2.9 and from Fig. 2.15 it may be concluded that the slight differences in the average slot and stator temperatures may be acceptable depending on the study context, particularly when considering the significant reduction of complexity by reducing the physical problem to an analysis of solely heat conduction in solids.

The numerically determined thermal resistances of the air gap and the analytic calculations according to [36, 49, 71, 72], which are based on experimentally determined correlations, match fairly well, with a maximum relative deviation of $\pm 10\,\%$.

The determined thermal resistances of the studied air gap, which are calculated with [82–85], differ significantly from the numerical results. As [82–85] all use the same underlying correlation published in [86], the developed correlation for transfer in a vertical annulus may not be applicable to the model studied in this work.

The internally generated frictional losses may be calculated directly with CFD software. In analytic models or numerical models, which model only heat conduction, the frictional losses need to be estimated (Sec. 1.3.5) and combined with the thermal resistance of the air gap. In [46] half the windage losses are fed into each terminal of the thermal resistance of the air gap, an alternative might be to break the thermal resistance into sub-resistances and assign the total windage losses to

the new node between the stator and the rotor surface. As illustrated in Sec. 2.5.1, the windage losses may become a significant loss source at higher rotational speeds. It may therefore be advisable to verify the applicability of empirical correlations in conjunction with concentrated loss injections particularly at higher rotational speeds as the relevance of the windage losses and the air gap resistance increases.

2.6 Bearings

2.6.1 Experimental determination of the thermal bearing resistance

The machine bearings link the stator housing and the rotor thermally in that they provide a heat flow path from the rotor stack and the shaft to the machine housing. Attempts to determine the thermal resistance of bearings (installed in electric machines) experimentally may be found in [50, 71].

If the internal heat generation is neglected, the thermal resistance of a bearing $R_{\mathrm{th,be}}$ may generally be calculated in terms of the temperature drop across the bearing $\Delta\vartheta$ and the heat flow across the bearing $\dot{Q}$ with

$$R_{\mathrm{th,be}} = \frac{\Delta\vartheta}{\dot{Q}}. \tag{2.55}$$

In practice, an accurate experimental determination of the thermal resistance is not trivial as the exact value of $\dot{Q}$, which corresponds to the temperature drop $\Delta\vartheta$, is difficult to identify precisely in a machine assembly.

Not only are also losses generated inside the bearings and detailed information of the specific bearings would be required to estimate the losses with higher accuracy (Sec. 1.3.5). The fact that heat is not solely transferred from the rotor across the shaft and the bearings but also from the rotor (i) across the air gap, (ii) to the inner air by convection and (iii) maybe even to a load machine that may be connected to the shaft complicates matters further. Furthermore, the thermal resistance itself varies with speed and load, as shown in [87].

In [50] analytic thermal machine models are calibrated by DC tests at standstill and the thermal resistances are evaluated by subsequent locked-rotor tests. The presented results for three different bearing types are given as equivalent, air-filled interface gaps that range from 0.23 mm to 0.40 mm, which may be expressed as interface conductances h_{intf} (Sec. 1.4.4) between 65 $\frac{\mathrm{W}}{\mathrm{m^2\,K}}$ and 113 $\frac{\mathrm{W}}{\mathrm{m^2\,K}}$. The resulting thermal resistances would be calculated with the interface area A according to Eq. (1.28).

In [71] the thermal resistances of bearings of two different machines are determined by matching the measured temperatures with the calculated temperatures

by adjusting the thermal resistances of the bearings. Values are presented for different load points, namely for the no-load point as well as for 50 %, 100 %, and 150 % of the rated machine power. The matched values for $R_{\mathrm{th,be}}$ range between 0.71 $\frac{\mathrm{K}}{\mathrm{W}}$ and 2.34 $\frac{\mathrm{K}}{\mathrm{W}}$.

2.6.2 Calculation of the thermal bearing resistance

As an alternative to an experimental determination, the thermal resistances of the bearings may be calculated. In [81] the thermal resistance is modelled as the sum of the thermal resistances of both bearing races, the rolling elements and the lubricating film. The thermal resistance of the film is calculated by the film thickness divided by the product of lubricant thermal conductivity and the area of the contact zone. The film thickness in this simplified approach would, however, need to be determined with the theory of elastohydrodynamic lubrication. The accurate calculation, which is not shown explicitly in [81], requires detailed information, including details about the lubricant, the surface velocity and pressure in the contact region [88]. It may even be argued that the film thickness itself is not even constant as assumed in this approach.

In [72] a simple equation for the thermal resistance of bearings in TEFC machines is derived from measurements and the same equation is used in [42]:

$$R_{\mathrm{th,be}} = k_1 \left(0.12 - k_2 \, \bar{d}_{\mathrm{b}}\right) \left(33 - k_3 \, \omega \, \bar{d}_{\mathrm{b}}\right), \tag{2.56}$$

where
$k_1 = 0.45 \, \frac{\mathrm{K}}{\mathrm{W}}$, $k_2 = 1 \, \frac{1}{\mathrm{m}}$, $k_3 = 1 \, \frac{\mathrm{s}}{\mathrm{m}}$,
valid if
$46\,\mathrm{mm} \leq \bar{d}_{\mathrm{b}} \leq 77.5\,\mathrm{mm}$ and $\omega \, \bar{d}_{\mathrm{b}} \leq 14.5 \, \frac{\mathrm{m}}{\mathrm{s}}$.

In Eq. (2.56) linear correlations between the thermal bearing resistance and the rotational speed and the mean bearing diameter $\bar{d}_{\mathrm{b}}$ are assumed. This equation is said to be only applicable to a limited range of bearing diameters and a maximum rotational speed of 3000 $\frac{1}{\mathrm{min}}$. Furthermore, the fact that only the diameter of the bearing and not the bearing width is used and that the equation includes a simple linear speed dependency—without, for instance, considering the effect of the bearing load—indicates that this equation may be used to give rough approximations of the thermal bearing resistance. The determined bearing resistances in [72] range between 0.48 $\frac{\mathrm{K}}{\mathrm{W}}$ and 0.88 $\frac{\mathrm{K}}{\mathrm{W}}$.

An approach that does not rely on detailed information about the lubrication regime and which is yet applicable to a wide range of different bearings is based on typical values of the heat flow density at the bearing seating surfaces A (or the

heat transfer coefficient k_q) for radial and axial roller bearings. Such values have been published by bearing manufactures and may even be extracted from ISO standard 15312 [21,22,24] (Fig. 2.19).

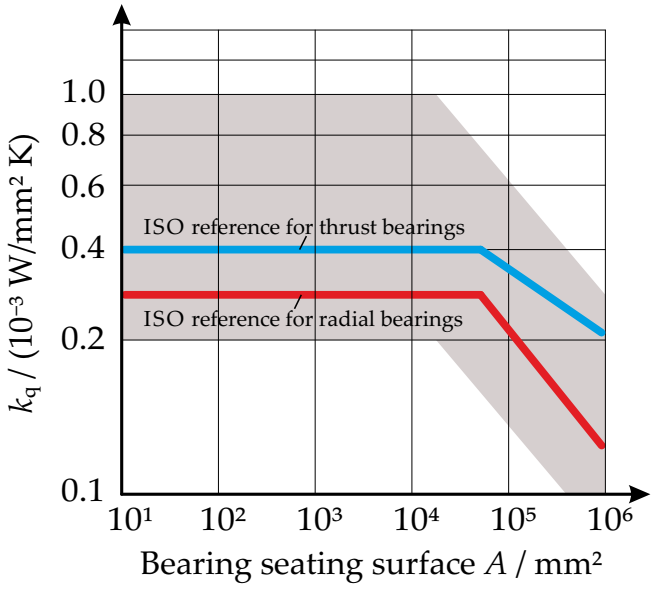

Figure 2.19: Ranges for the heat transfer coefficient and the reference values according to ISO standard 15312, adapted from [21,22,24,25].

The standard specifies the calculation of the thermal speed rating of bearings under defined reference load, temperature, and lubrication conditions. The thermal speed rating is calculated using the heat balance between the internally generated losses and specified reference heat flow densities.

Fig. 2.19 differs from the figures provided in [21,24,25] in that the heat flow densities are related to the temperature difference of 50 °C, which is defined in ISO 15312, thereby converting the heat flow densities into equivalent heat transfer coefficients. The two functions in Fig. 2.19 are the equivalent reference heat transfer coefficients for radial and thrust bearing, as defined in ISO 15312. The shaded area illustrates typical ranges of k_q that are identical with the equivalent heat flow densities provided in [21].

The heat flow rate $\dot{Q}$ across the bearing seating surface A is connected with the temperature difference between the mean bearing temperature and the ambient temperature $\Delta\vartheta$ and the heat transfer coefficient k_q as follows [22]

$$\dot{Q} = k_q \, A \, \Delta\vartheta. \tag{2.57}$$

The bearing seating surface of radial bearings is [22]

$$A = \pi \, b_b \, d_b + \pi \, b_b \, D, \tag{2.58}$$

where

d_b bore diameter,

b_b bearing width,

D bearing outer diameter.

Combining Eqs. (2.57) and (2.58) yields

$$\frac{\Delta\vartheta}{\dot{Q}} = \frac{1}{k_q A} = \frac{1}{k_q\left(\pi\, b_b\, d_b + \pi\, b_b\, D\right)} = R_{th,be} \quad \text{and} \tag{2.59}$$

$$R_{th,be} = \frac{1}{\frac{1}{1/\left(k_q \pi\, b_b\, d_b\right)} + \frac{1}{1/\left(k_q \pi\, b_b\, D\right)}} = \frac{1}{\frac{1}{R_{th,beIn}} + \frac{1}{R_{th,beOut}}}\,. \tag{2.60}$$

The heat transfer coefficients k_q in Fig. 2.19 therefore allow to calculate thermal resistances $R_{th,be}$ of bearings that correspond to the ISO standard (values deemed typical) as well as minimum and maximum values. Eq. (2.60) furthermore illustrates the thermal bearing modelling in [71], which is shown in Fig. 2.20.

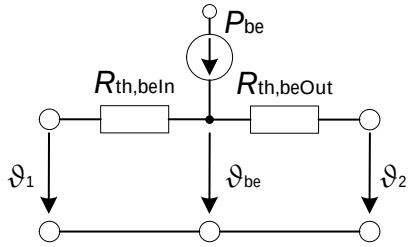

Figure 2.20: Thermal bearing model, adapted from [71].

As can be seen from Eq. (2.60), $R_{th,be}$ may be split into two thermal resistances $R_{th,beIn}$ and $R_{th,beOut}$ modelling the heat flux across the inner and the outer bearing seating. ϑ_{be} in Fig. 2.19 denotes the mean bearing temperature, ϑ_1 and ϑ_2 the temperature at the inner and at the outer bearing seating respectively. The frictional losses P_{be}, which are generated in the bearing, are modelled by a heat source.

It may be noted that heat might be dissipated by the lubricant in the case of oil lubrication. The dissipated heat would then be modelled by an additional loss source with negative loss values. The loss magnitude is calculated with Eq. (2.10), using the flow rate of the lubricant, the temperature elevation, the mass density and the specific heat.

2.6.3 Summary

It has been shown in Secs. 2.6.1 and 2.6.2 that the thermal resistance of bearings may be determined (approximately) by measurements or by computation. The bearings are mostly modelled as contact resistances.

The detailed bearing modelling is still subject to ongoing research and even approaches that try to find simpler ways to model thermal aspects in elastohydrodynamic contacts are rather complex studies, e.g. [89]. When including bearings into an overall thermal machine model, the aim is to correctly identify the heat transferred across the bearing and the heat generated in the bearing. Therefore, modelling the bearing phenomenologically on a macroscopic scale seems to be a more effective approach. Particularly if only limited data is available, the approach presented in Sec. 2.6.2 provides ranges that allow for the estimation of typical values and even best and worst case estimations.

The resulting equivalent thermal heat transfer coefficients in [50], which range between 65 $\frac{\mathrm{W}}{\mathrm{m^2\,K}}$ and 113 $\frac{\mathrm{W}}{\mathrm{m^2\,K}}$, are in accordance with the range from 200 $\frac{\mathrm{W}}{\mathrm{m^2\,K}}$ to 1000 $\frac{\mathrm{W}}{\mathrm{m^2\,K}}$ given in [22] and implicitly in [21]. This is because the factor 2 needs to be considered when comparing [50] and [21, 22] as the total thermal resistance $R_{\mathrm{th,be}}$, which is related to a combined average seating surface, is determined in [50].

In [71] the comparison between the calculated thermal resistances and the *matched* measured values are also in close agreement with the values provided by [21,22,24].

In **analytic machine models** the thermal bearing model shown in Fig. 2.20 may be connected directly between the shaft and the machine housing or an end cap model.

Considering the above mentioned aspects and the typical role of bearing models in a **numerical thermal machine model**, detailed (microscopic) bearing models, which may even aim at modelling the local effects in the contact area, typically lie beyond the scope of the thermal machine modelling. Therefore, approaches modelling the macroscopic behaviour or even the behaviour at the model interfaces—for instance similarly to the analytic modelling by one or two contact resistances and a boundary heat flux—may be an efficient and yet fairly accurate choice.

2.7 Axial heat flow

2.7.1 Shaft

A significant heat flow path in axial direction is present in the shaft of electric machines, which permits conductive heat transfer between the rotor stack and the stator (through the bearings).

The numerical modelling of heat transfer through a shaft is illustrated in Fig. 2.21. Simple boundary conditions are used in order to allow for a comparison between the results obtained from the numerical simulation and an analytic calculation. The bearing seats on both sides of the shaft are set to fixed temperatures (60 °C), $\dot{Q} = 100\,\mathrm{W}$ are injected (uniformly) at the surface that would be in contact with the rotor

stack. The thermal conductivity $\lambda = 237 \frac{\mathrm{W}}{\mathrm{m\,K}}$ is chosen for the shaft.

The geometry and the boundary conditions may be seen in Fig. 2.21(a), the temperature distribution on the surface of the shaft is shown in Fig. 2.21(b). The temperatures on the cutting plane and along the axis of symmetry in the centre of the shaft are shown in Figs. 2.21(c) and 2.21(d) respectively.

It can be seen from the temperature profile in Fig. 2.21(d) that the heat flow problem is complex despite the comparably simple geometry. The radial loss injection and the radial temperature as well as the diameter step lead to significant deviations from a one-dimensional temperature profile.

The average temperature of the surface where the heat is injected is 71.9 °C, the (volumetric) average temperature of the wider inner shaft part is 71.6 °C. The difference between both temperatures is comparably small and they are modelled by a common temperature ϑ_1.

The analytic modelling is based on the assumption of solely axial heat flow. Two parallel heat flow paths are assumed between ϑ_1 and the two bearing seats (Fig. 2.22).

The first heat flow path consists of the thermal resistance $R_{\mathrm{th},1}$ between the left bearing seat and the diameter step and $R_{\mathrm{th},3}$, which models the effective thermal resistance between the diameter step and ϑ_1. The second heat flow path is modelled by $R_{\mathrm{th},2}$ (thermal resistance between right bearing set and the diameter step) and $R_{\mathrm{th},3}$.

$R_{\mathrm{th},1}$ and $R_{\mathrm{th},2}$ as well as the 80 mm-long axial thermal resistance of the thicker section ($R_{\mathrm{th},4}$) can be calculated directly with the dimensions of the shaft and λ

$$R_{\mathrm{th},1} = 2.49 \cdot 10^{-1} \frac{\mathrm{K}}{\mathrm{W}}, \tag{2.61}$$

$$R_{\mathrm{th},2} = 8.95 \cdot 10^{-2} \frac{\mathrm{K}}{\mathrm{W}}, \tag{2.62}$$

$$R_{\mathrm{th},4} = 2.98 \cdot 10^{-1} \frac{\mathrm{K}}{\mathrm{W}}. \tag{2.63}$$

In [71] $R_{\mathrm{th},3}$ is approximated by using 50 % of the relevant flow path length from the diameter step to the average temperature node, which is 25 % (20 mm) of the complete length of the wider inner shaft part (80 mm). With this assumption $R_{\mathrm{th},3}$ and ϑ_1 are

$$R_{\mathrm{th},3} = \frac{R_{\mathrm{th},4}}{4} = 7.45 \cdot 10^{-2} \frac{\mathrm{K}}{\mathrm{W}}, \tag{2.64}$$

$$\vartheta_1 \quad = 71.1\,^{\circ}\mathrm{C}. \tag{2.65}$$

(It may be noted that using the complete flow path, i.e. half the complete length (40 mm), would be an overestimation as this would translate into the assumption that all injected heat enters exactly in the centre.)

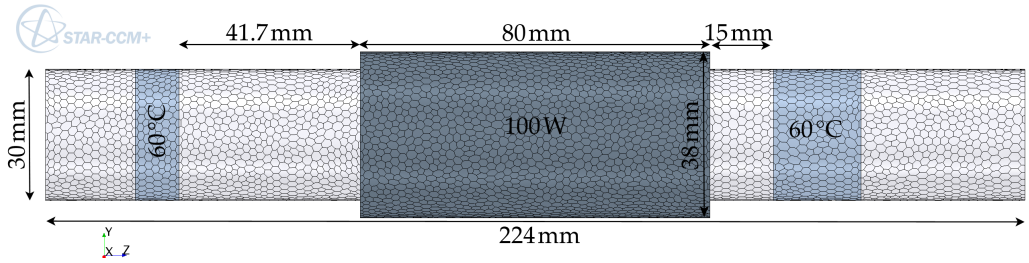

(a) Geometry & boundary conditions of the shaft.

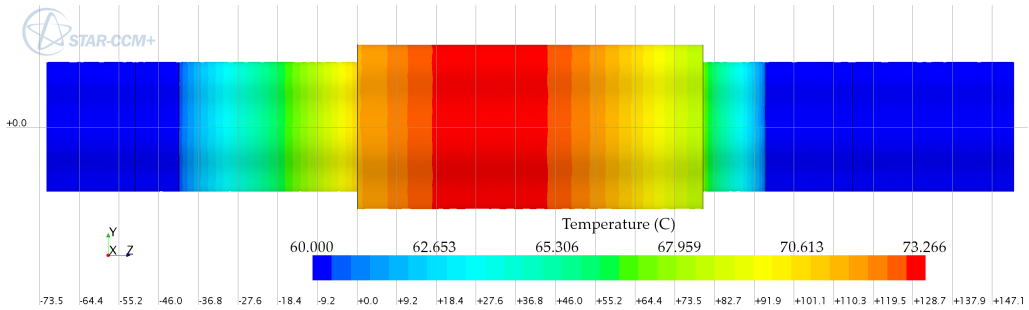

(b) Temperature distribution on the surface.

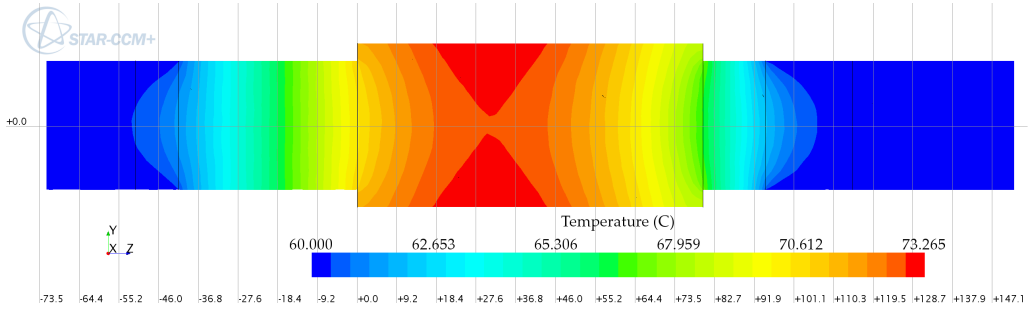

(c) Temperature distribution on cutting plane through centre of shaft.

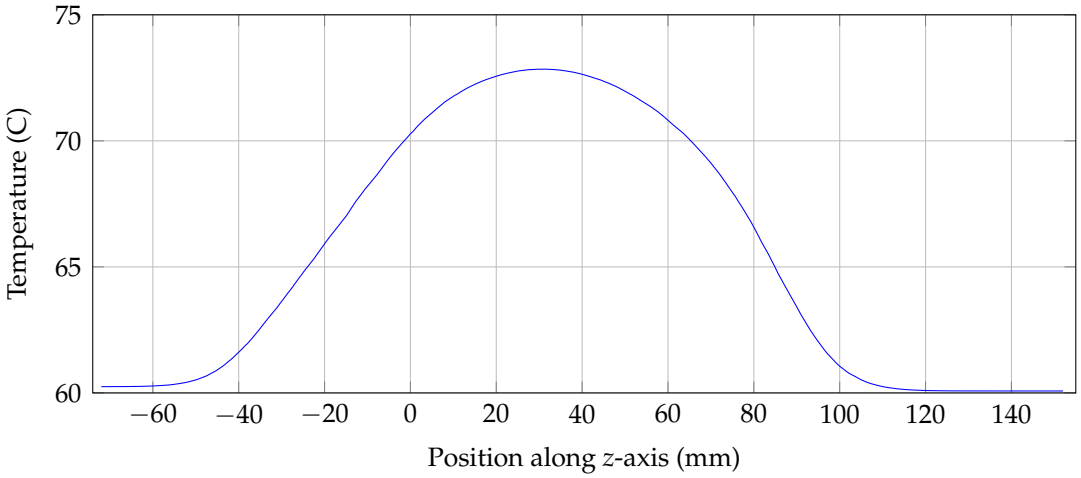

(d) Temperature plot along the axis of symmetry in the shaft.

Figure 2.21: Exemplary study of heat flow through a shaft.

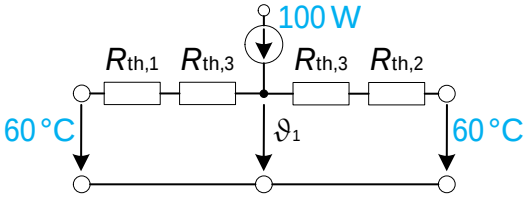

Figure 2.22: Lumped parameter model of the shaft in Fig. 2.21(a).

The quadratic temperature profile in the wider part (Fig. 2.21) resembles a quadratic temperature profile caused by one-directional heat conduction with spatially uniform internal heat generation (Sec. 1.5.3, [33, 35, 37]). If the heat conduction in this part is treated as one-dimensional heat transfer with internal uniform heat generation, $R_{\mathrm{th},3}$ and ϑ_1 are

$$R_{\mathrm{th},3} = \frac{R_{\mathrm{th},4}}{6} = 4.97 \cdot 10^{-2}\,\frac{\mathrm{K}}{\mathrm{W}}, \tag{2.66}$$

$$\vartheta_1 \quad = 69.5\,^{\circ}\mathrm{C}. \tag{2.67}$$

Comparing Eqs. (2.65) and (2.67) with the average temperature of the inner shaft (71.6 °C) shows that estimating the average temperature by using half the complete flow is more suitable than treating the radially injected heat as a one-dimensional heat transfer problem with spatially uniform internal heat generation.

2.7.2 Other heat flow

Following Sec. 2.3.3, axial heat transfer is neglected in the stacked electrical steel sheets. Due to the significantly lower thermal conductivity of the insulating material compared with the copper wires, axial heat transfer in the stator is only considered for the copper wires. In the rotor, heat is transferred axially in the aluminium bars.

Axial heat flow in the copper wires and in the bars is modelled as one-directional heat transfer with internal heat generation (Sec. 1.5.3).

2.8 Convection in the end winding region

The analysis of convection in the end winding region is generally very demanding due to the complex shapes and the resulting non-trivial fluid flow.

In analytic models, correlations are typically used for the modelling of convective heat transfer. A general correlation, which is also used in this study, is (e.g. [46, 90, 91])

$$\overline{h} = k_{\mathrm{cc},1}\left[1 + \left(k_{\mathrm{cc},2}\,v\right)^{k_{\mathrm{cc},3}}\right], \tag{2.68}$$

where

$k_{cc,i}$	convection correlation parameters,
v	reference velocity.

The correlation in Eq. (2.68) is used to determine the average heat transfer coefficients of the different surfaces at which convective heat transfer is present. Different sets of correlation parameters $[k_{cc,1}, k_{cc,2}, k_{cc,3}]$ have been determined experimentally and an overview of different correlations may be found in [46].

v, the reference velocity in Eq. (2.68), is the velocity of the rotating surface (which may be given as a function of the rotational speed), or the velocity of the surrounding air if the surface is stationary (e.g. the end windings).

The analytic modelling of convection in [36] is shown in Fig. 2.23(a). Even though a TEFC induction machine is modelled, the general modelling approach may be used similarly for the modelling of water-cooled machines. Node 8 in Fig. 2.23(a) represents the inner air in the end winding region, nodes 1 to 7 are the surfaces (interfaces to the inner air) of the end cap (1), the stator stack (2), the stator teeth (3), the end winding (4), the end ring (5), the rotor stack (6), and the rotor cooling holes (7). Each thermal resistance is determined with Eq. (1.22), using the corresponding average heat transfer coefficient and the corresponding interface area.

In order to gain a higher degree of adaptability, in particular if significant differences of the reference velocity exist on one and the same interface to the inner air, thermal resistances may be split into several sub-resistances as illustrated in Fig. 2.23(b). In this exemplary model from [46], the thermal resistance between the end winding and the inner air in the end winding region is composed of four sub-resistances. The interface to the inner air is split into an inner and an outer end winding interface as well as into an interface at the axial end of the end winding and an interface to the air gap between the end winding and the stator stack (depending on how much the winding extends beyond the stack end before merging into the end winding).

It may be noted that a common average temperature is modelled at all four interfaces in Fig. 2.23(b) (at node 2) and that heat transfer is consequently modelled between this temperature level and one common temperature level of the inner air in the end winding region. Therefore, the parallel paths only allow to adjust the convection parameters separately but do not yield a higher resolution of the temperature distribution. Furthermore, the reference velocities need to be estimated, which is difficult if non-trivial geometries are present. Additionally, the most suitable convection correlation parameters need to be chosen, which requires experience in this field or requires experimental tests in order to adjust the parameters appropriately.

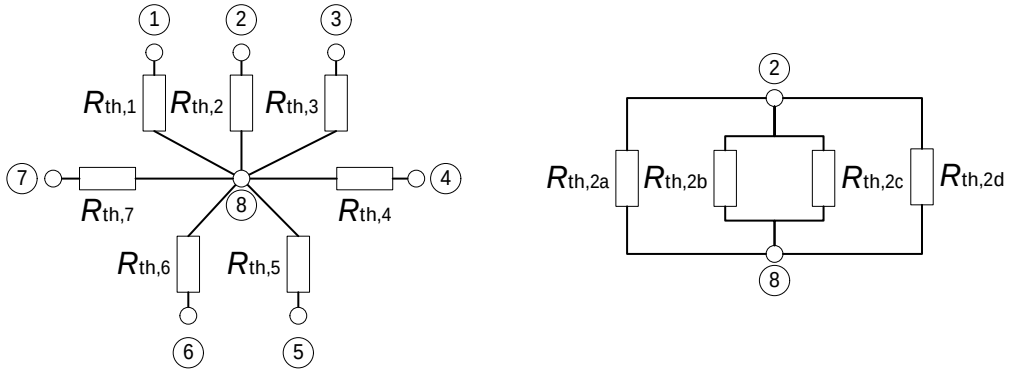

(a) Modelling of convection in the end winding region in [36].

(b) Modelling of convection at the end winding in [46].

Figure 2.23: Analytic modelling of convection in the end winding region.

The numerical modelling of convection in the end winding region requires a comparably precise CAD model at the solid-fluid interface (including e.g. cavities) and a fine mesh in order to capture those geometric features and to allow for the modelling of flow near the interface.

In [92, 93] CFD simulations are carried out with particular focus on the analysis of heat transfer in the end winding region. The simulations are compared with the measured heat fluxes as heat flux sensors are attached near the end winding tips of the form-wound windings of the studied induction machine.

Smaller electric machines typically consist of random-wound windings. The end windings therefore consist of (to a certain extent) randomly placed thin wires, insulating sheets (between the coil sides of different phases and, optionally, also for tightening the loose wires), and impregnating resign which is supposed to fill most air pockets.

The explicit modelling of all wires and the insulating material in the winding heads would drastically increase the model complexity (CAD model, meshed representation and resulting mathematical problem). While the detailed modelling may be feasible in very specific detailed studies focussing on just a particular part of the end winding region (similar to the detailed slot model in Sec. 2.3.5 but with significantly increased complexity due to the explicit three-dimensional nature of the problem), geometric simplifications of the end winding regions are indispensable in the frame of complete machine models. Since the shape of the end winding varies due to the (to some degree) random placement of the wires that are covered with impregnating resign, envelopes may be used to define the outer dimensions of the end windings. A similar approach is used in the CFD machine study in [94], in which the end windings are modelled by envelopes.

The results of an exemplary CFD study are provided in Fig 2.24 which shows the resulting boundary heat flux at the interface between the inner air and the air cap. The interface is clipped in axial direction in order to allow for a direct view on the interface. Additionally, a vector plot of the velocity of the inner air is shown on the cutting plane which also shows the semi-transparent contours of the solids. The air volume in the foreground is the air between the side of the rotor stack and the end shield which is narrowed down in radially outward direction because of the end rings. The cutting plane is not clipped and the contours as well as the velocity vectors in the air gap therefore span further out than the heat flux boundary. The envelope of the end winding may be seen in the background.

Such a CFD study allows, to give one example, to investigate the effect of the ribs of the end cap in Fig 2.24 which cause high heat flux gradients at the interface. The envelope-like modelling of the end winding reduces the modelling complexity and the calculation time, it is, however, a significant simplification that forbids to consider or investigate the effect of the imperfect end winding shape and impregnation.

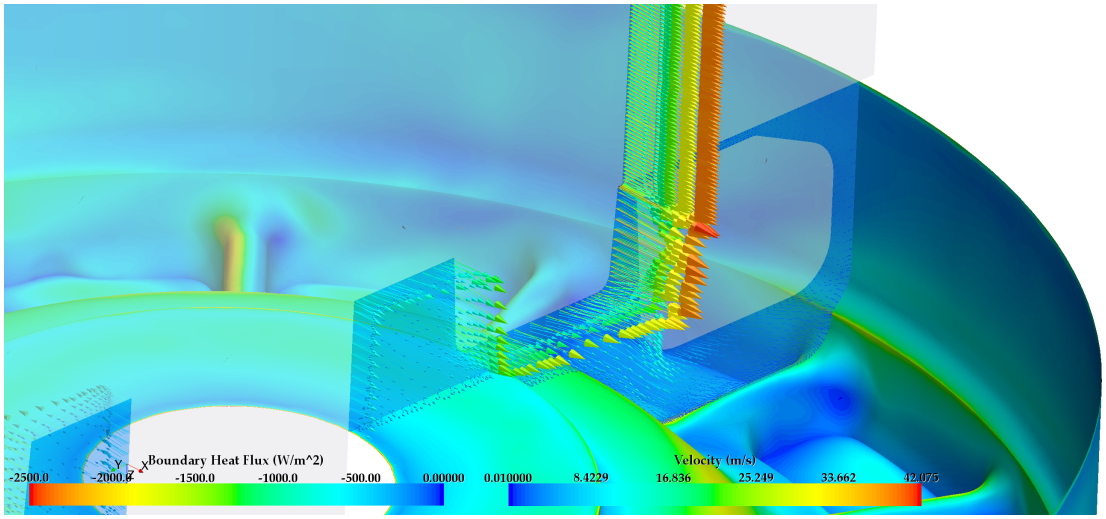

Figure 2.24: Exemplary CFD study of heat transfer in the end winding region.

2.9 Effect of adjacent components

The thermal behaviour of electric machines may be influenced by adjacent components to such an extent that modifications of the thermal model itself may be required.

To give an example, the induction machine in [36] is modelled by a simplified symmetrical thermal model with sufficient accuracy (Fig. 1.4). If the same motor is, for instance, fixed to a test bench (heat sink) or if a gear train is connected (heat

source), the motor may show significant temperature differences between the DE and the NDE side. In such cases, not only one or more additional boundary conditions need to be set but the model of the machine itself needs to be extended to adequately model the non-symmetrical heat flow and temperature distribution (compare Figs. 1.4 and 3.4).

Furthermore, special attention may be required if a thermal model is adjusted and validated by experimental tests, using an experimental (lab) set-up which differs significantly from the standard environment the machine is typically operated in, such as a vehicle environment. Significant deviations may consequently lead to incorrectly calibrated models or the validation may yield misleading results.

The effect of a connected loss source is exemplified by two simple experimental tests. During theses tests, the device under test (DUT), a squirrel-cage induction machine, is driven by a connected motor, using the test bench illustrated in Fig. 3.2. The resulting temperatures over time are given in Fig. 2.25.

The generated losses of the connected gear train are the main loss source in this experimental set-up. Comparably small additional loss sources are the frictional losses in the bearings and the sealing rings as well as the windage losses. The temperature of the motor is controlled by a circulating water temperature control unit which controls the temperature at the inlet of the water jacket cooled DUT.

In the first test (Fig. 2.25(a)), the inlet temperature of the machine at stand-still is set to 48.7 °C. When the temperatures reach steady states (at $t = 666\,\text{min}$), the DUT is accelerated to $n = 6000\,\frac{1}{\text{min}}$. At $t = 920\,\text{min}$, the target inlet temperature is reduced to 30 °C while the DUT is kept at the constant rotational speed $n = 6000\,\frac{1}{\text{min}}$.

At stand still the measured rotor temperatures are slightly lower than the measured temperatures of the coolant at the inlet, the stator and the housing. The rotor (and the gear oil reservoir) are expected to be colder than the inlet temperature in this passive test since some of the heat is transferred from the cooling channels to the side surfaces of the housing and also to the rotor and the shaft to the surrounding. The heat flow causes temperature drops across the thermal resistances of the heat flow paths.

During rotation, the rotor heats up from 48 °C to around 61 °C at the NDE side and to 65 °C at the DE side. The rotor temperature at the DE side is thus notably higher. The measured temperature in the stator slot and the temperature of the oil in the gear oil reservoir are well below the rotor temperatures and reach around 51 °C. The temperature differences remain in similar ranges even during the cooling down phase.

As the gear oil reservoir remains fairly cold (temperature in the range of the stator winding), the thermal behaviour may be modelled by heat injections into the rotor.

During the second test (Fig. 2.25(b)) the DUT is kept at the constant rotational speed $n = 6000\,\frac{1}{\text{min}}$ and the inlet temperature at 78.6 °C. At $t = 735\,\text{min}$ the temperature control unit is switched off and at $t = 1079\,\text{min}$ the DUT is brought to a standstill.

The temperature dependency of the gear losses (which are lower at higher temperatures) may be seen in Figs. 2.25(a) and 2.25(b) when comparing the temperature differences between the rotor and the stator and also the temperature differences between both rotor temperatures.

In general, such experimental tests may also be used to estimate the split of the injected gear losses as only a fraction of the total gear losses is injected into the rotor. Some losses are also directly transferred to the motor (gear) housing.

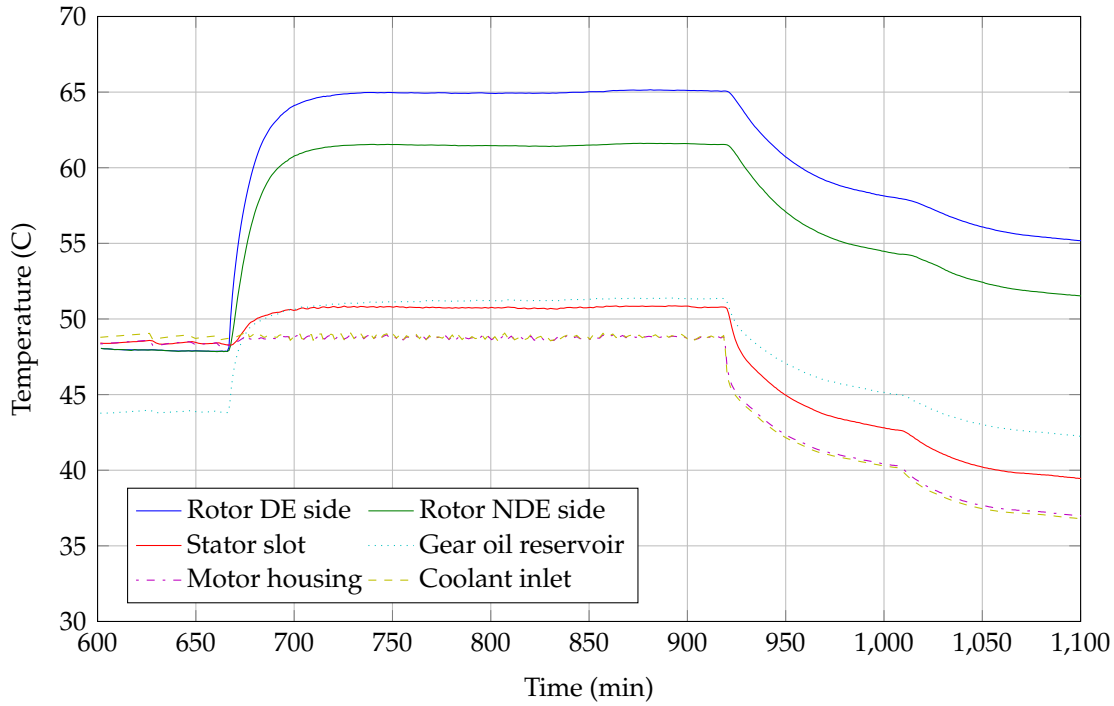

(a) DUT accelerated by connected motor from stand-still to constant rotational speed, subsequent active cooling down by circulating water temperature control unit.

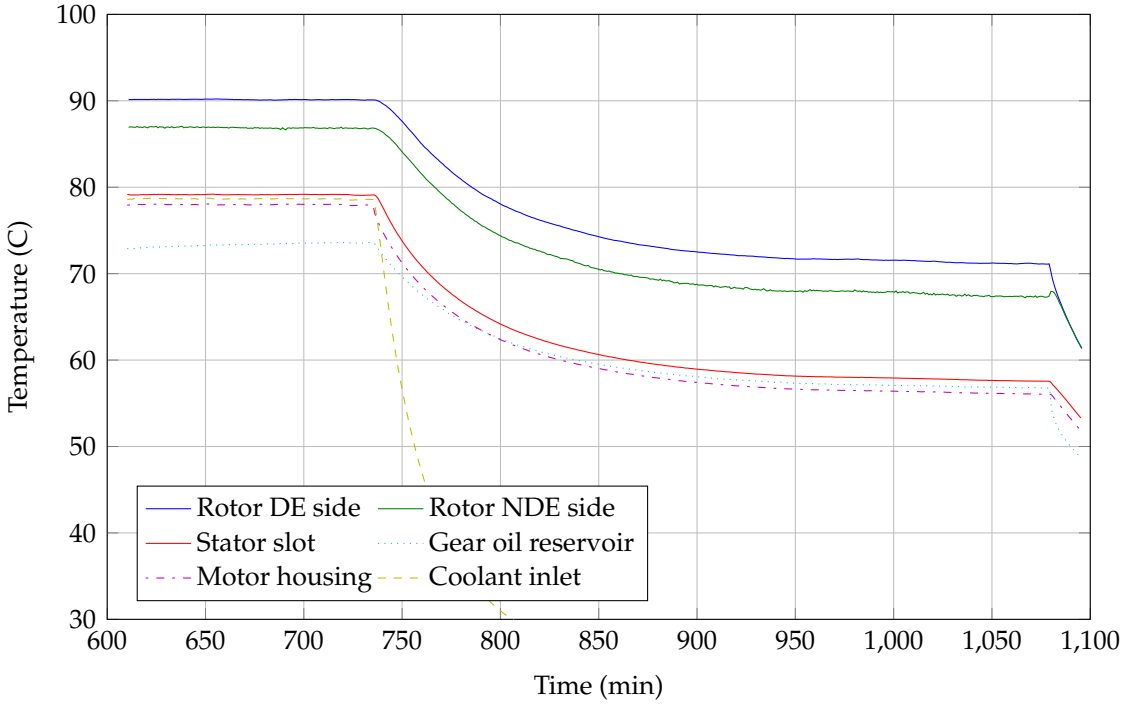

(b) DUT driven by connected motor at constant rotational speed, cooling down at constant speed (coolant flow rate set to zero) and cooling down at stand-still.

Figure 2.25: Temperature increase due to gear losses when DUT is driven by a connected motor.

Chapter 3

Case study

Both modelling approaches, the analytic and the numerical modelling, are applied to a squirrel-cage induction (traction) motor and assumptions and simplifications in each strategies as well as similarities and differences are highlighted.

The experimental set-up is presented in Sec. 3.1 and the experimental tests which are used to calibrate and to verify the thermal models are given in Sec. 3.2.

The analytic and the numerical modelling frameworks of the induction machine are introduced in Sections 3.3 and 3.4 respectively.

The analytic and the numerical thermal component models are provided in Sec. 3.5. The evaluation of the thermal models (and modelling frameworks), i.e. the comparison of the simulations with the measurements, may be found in Sec. 3.6.

3.1 Experimental set-up

3.1.1 Test bench

Experimental tests that permit to adjust, verify and interpret the simulation results are carried out on the test bench in Fig. 3.1(b)[1]. The DUT, a squirrel-cage induction machine, which is underneath a protective cover, is shown in Fig. 3.1(a). A schematic diagram of the experimental set-up is shown in Fig. 3.2.

As can be seen in Fig. 3.1(a), the tested induction machine (IM 1) is connected to a gear train and coupled to a second induction machine (IM 2). The rotational speed and the torque are measured by a torque transducer which is placed in between. Both induction machines are generally fed by an inverter. For operational reasons, certain tests (including the DC test) require the use of power amplifiers in conjunction with a function generator as power supply of the DUT instead.

[1] The experimental tests on the test bench in Fig. 3.1 were carried out in the main laboratory of the Electric Drives & Machines Institute at Graz University of Technology, Austria (EAM), by Dr. Roland Seebacher, Assistant Professor at the EAM.

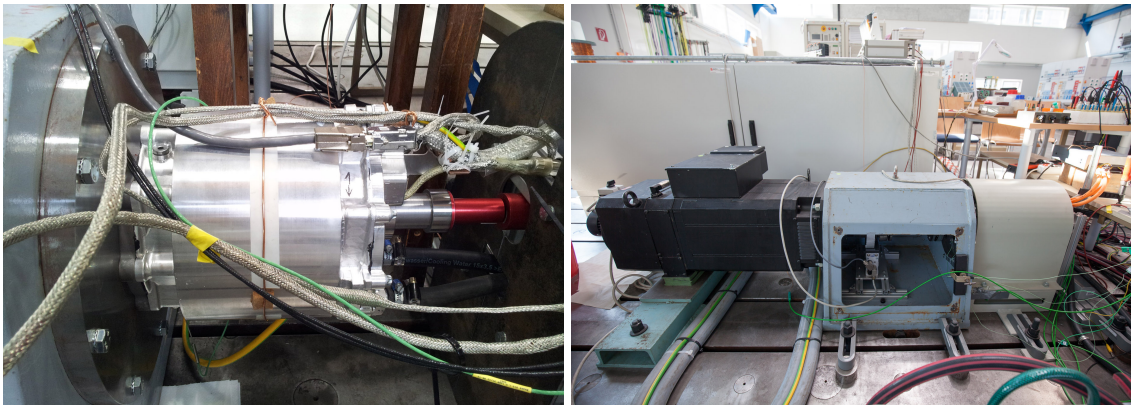

(a) Induction machine (DUT)

(b) Test bench (from left to right): Dynamometer, torque measuring shaft and DUT (both underneath protective covers)

Figure 3.1: Experimental set-up.

The temperature control unit allows for an adjustment of the temperature of the coolant and the flow rate. Heat dissipation is ensured by a connected fan-cooled heat sink.

The temperature measurements are handled by two separate data acquisition systems that are connected to a workstation. The first data acquisition system obtains (i) the rotor temperatures $\vec{\vartheta}_{\mathrm{rot}}$ from an inductive temperature measuring device (thermocouples *Type K*) but also processes (ii) the mass flow rate of the coolant $\dot{m}$ (strictly speaking the volume flow rate), (iii) the output torque M and the rotational speed n as well as (iv) the input power of each phase $\vec{P}$, the voltages $\vec{V}$, the currents $\vec{I}$, and the supplied frequency f_1.

The temperature probes in the inlet and the outlet of the cooling jacket (*Pt100* resistance temperature detectors) as well as the sensors that are attached to the stator of the machine and its surrounding (thermocouples *Type K*) $\vec{\vartheta}_{\mathrm{stat}}$ are connected to the second data acquisition system.

3.1.2 Thermal sensors

Two thermocouples (TC) are placed in the stator slots (approximately in the centre in axial direction), one at the bottom of the slot on the slot liner and therefore in the immediate vicinity of the wires at slot bottom (TC 1), the second sensor is placed directly on top of the copper wires (TC 2) and thus below the slot wedge. Further thermocouples are placed in the middle of the end windings on each machine side (TC 3 at the non-drive end side (NDE) and TC 4 at the drive end side (DE)). The two thermocouples in the rotor (TC 5 at the NDE side and TC 6 at the DE side) are

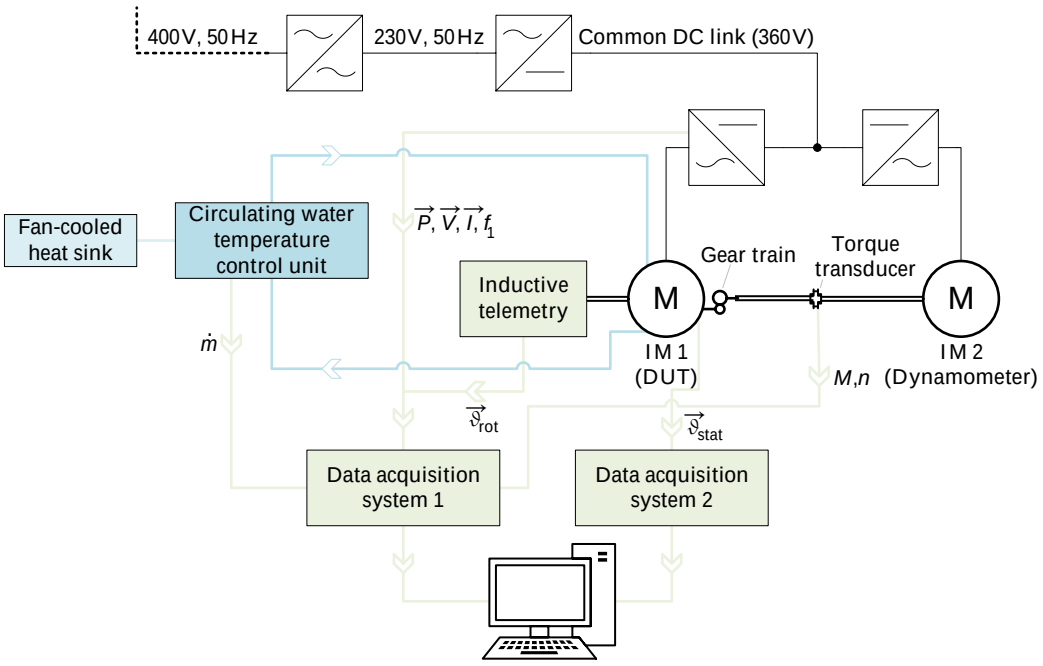

Figure 3.2: Schematic diagram of the test bench.

inserted into the rotor stack (a few millimetres from both stack ends) and the temperatures are read by an inductive temperature measuring device. An additional thermocouple (TC 7) is placed in the gear oil reservoir.

The resistance temperature detectors (RTD) are placed directly in the flow in the inlet region (RTD 1) and in the outlet region (RTD 2) of the cooling jacket. Additional thermocouples are placed in the (directly attached) gear train and on the outer surface of the cooling jacket.

Furthermore, the temperature of the air underneath the protective cover, the temperature of the cover, and the ambient air temperature are measured by further thermocouples in order to correctly set and verify the boundary conditions of the thermal model. The sensors and their position in the electric machine are summarised in Table 3.1.

Table 3.1: Sensor identifiers and positions.

Sensor	Sensor position
TC 1	slot bottom
TC 2	slot top
TC 3	end winding NDE side
TC 4	end winding DE side
TC 5	rotor stack end NDE side
TC 6	rotor stack end DE side
TC 7	gear train (oil reservoir)
RTD 1	cooling jacket inlet
RTD 2	cooling jacket outlet

3.2 Experimental tests

Typical ranges of certain thermal resistances, particularly the thermal contact resistances (Sections 1.4.4 and 2.1), the effective thermal resistance between the winding and the electrical steel stack because of a non-ideal impregnation (Sec. 2.3) and the wide range of heat transfer coefficients of bearings (Sec. 2.6), introduce potential uncertainties, particularly in case a thermal model is developed without any experimental adjustment or validation or without reliable information based on similar machines (preferably the same machine design with identical manufacturing processes).

In order to be able to correctly adjust the thermal resistances of the induction machine, it is advisable to not solely rely on one or more typical load points for the model verification as this may lead to incorrectly adjusted parameters due to the complex overall heat flow along the different flow paths.

Consequently, a DC (during which the Joule losses in the stator winding dominate) and a locked rotor (with high Joule losses in the rotor bars in addition to the Joule losses in the stator winding) are used for a first verification of the thermal models. The reduced complexity with respect to the acting heat sources allows for a more precise identification of the losses and the heat flow paths and thus for a more accurate verification as well as for potentially required targeted parameter adjustments.

Additionally, a passive test is performed to verify the modelling of the gear train and of the mechanical loss sources in general, ensuring that the required simplifications of the gear modelling do not influence the thermal model at higher rotational

speeds.

Finally, a stationary load case is used to validate the analytic and the numerical model and an additional (thermally) transient load case is run to validate the transient analytic model.

The input parameters and the measured temperatures of the transient load case are provided directly in Sec. 3.6.5, the values of all other tests are compiled in separate tables for each test in Sections A.1–A.4 in the appendix.

Selected values are related to the values of the corresponding quantities at the nominal (rated) operating point of the electric machine and are given as *per-unit* values (pu). To give an example, copper losses in the stator winding of 0.1 pu refer to 10 % of the copper losses in the stator winding at the nominal operating point.

The detailed explanation of the experimental tests, the interpretation of the results and the evaluation of the models may be found in Sec. 3.6.

3.3 Analytic modelling framework

The overall analytic modelling framework comprises an electromagnetic machine model, a loss calculation routine and an analytic thermal machine model. The developed models are specific to induction machines and using a different machine type would require the adaptation of machine-specific analytic equations and models.

The electromagnetic model and the loss calculation routine depend, however, on the actual temperature, such as the resistivity of the copper wires and of the aluminium bars. The same applies to the numerical modelling where the correct values need to be set in the material database.

The measured temperatures are used to set the correct values for the temperature-dependent material coefficients instead of results from coupled analytic models.

As will be shown by the experimental tests, the analytically and the numerically determined losses as well as the measured losses differ significantly, leading to significant temperature differences. In order to avoid that a potentially inaccurate loss calculation, which would lead to potentially inaccurate simulated temperatures, feeds back into the loss calculation by the adjustment of the temperature-dependent coefficients, the measured temperatures are used to set the temperature-dependent coefficients correctly. A coupled model would increase the complexity associated with the verification of the thermal model itself.

3.3.1 Electromagnetic machine model

The electromagnetic lumped parameter model, which is used to model the electromagnetic behaviour of the induction machine and which consequently serves to determine the electromagnetic losses, is shown in Fig. 3.3. The model is based on a fundamental frequency lumped parameter modelling approach, which means that e.g. the effect of higher harmonics on torque production and energy conversion is not considered. Higher harmonics are treated as stray phenomena instead and thus included in the stray inductances.

The components of the lumped parameter model are explained in the following sections.

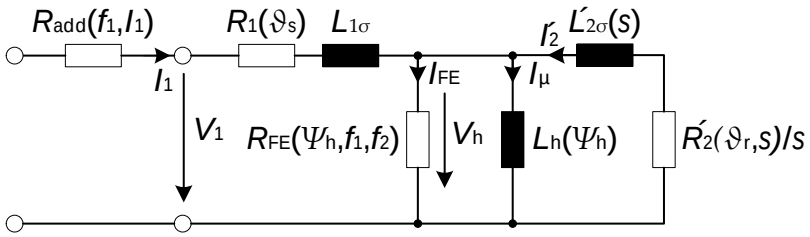

Figure 3.3: Electromagnetic lumped parameter model of the induction machine.

Leakage inductances

Several different leakage fluxes are present in electric machines which are, for example, caused by the placement of the winding in slots and by the presence of coil sides in the end winding region. The stator leakage inductance $L_{1\sigma}$ and the rotor leakage inductance $L_{2\sigma}$ therefore comprise several leakage inductances that are related to the different leakage fluxes, including e.g. the slot leakage fluxes.

Values for the slot permeance factor, which is used to calculate the slot leakage inductance, may be found in the literature for standard slot shapes and for single and double layer windings (e.g. in [7, 14, 95]). Similarly, equations and permeance factors to determine both the end winding leakage inductance and the tooth tip leakage inductance may be found in the literature [3, 7, 14, 95–97].

As the effect of higher harmonics is treated as stray phenomena in the fundamental frequency model, corresponding harmonic (differential) leakage inductances are included in the stator and in the rotor stray inductances in Fig. 3.3.

The stator slot leakage inductance for the double layer winding, the stator tooth tip leakage inductance and the end winding leakage inductance are calculated according to [7,95]. The value for the harmonic (differential) stator inductance is based on data from the motor manufacturer.

The rotor slot leakage inductance and the end ring leakage inductance are computed according to [7,98] and the value for the harmonic (differential) rotor leakage inductance is, similar to the harmonic stator inductance, based on data from the motor manufacturer.

The rotor stray inductance is referred to the stator by the conversion factor ζ_{conv} ($L'_{2\sigma} = \zeta_{\text{conv}}\, L_{2\sigma}$), which is a function of the winding factors, the number of slots and the number of phases of the rotor and the stator.

Under normal operating conditions ($s \ll 1$), the influence of the slip on the rotor resistance and on the rotor leakage inductance is negligible. Only during the locked rotor test, the rotor slot leakage inductance is reduced in accordance with the increased effective rotor bar resistance.

Winding resistances

The resistance of the stator winding R_1 is calculated with the coil turn length, the number of turns per coil, the connection of the coils, the number of parallel connected wires in one coil, the wire diameter and the resistivity of copper. As the resistivity of copper changes with the temperature (Sec. 1.3.1), the temperature of the winding is used to adjust its value using a linear temperature coefficient for copper.

The resistance of the rotor winding R_2 ($R'_2 = \zeta_{\text{conv}}\, R_2$) comprises the resistance of a rotor bar R_{bar} and of a corresponding section of the end ring resistance R_{er} [3,7]

$$R_2 = R_{\text{bar}} + \frac{R_{\text{er}}}{2\sin^2(\frac{\pi p}{Q_{\text{r}}})}, \tag{3.1}$$

where

p	number of pole pairs,
Q_{r}	number of rotor slots.

The value of the rotor resistance is also adjusted with the rotor temperature by using the linear temperature coefficient of aluminium.

At high slip rates, in particular during the locked rotor test, the skin effect has a noticeable effect on the resulting rotor resistance and an additional factor, which is a function of the slip [7], is used for the modelling of the rotor (bar) resistance in such cases.

Calculation of the magnetic circuit and determination of the magnetising inductance

The non-linear behaviour of the electrical steel (non-linear BH-curve) requires the iterative calculation of the magnetic circuit in order to calculate the magnetising

inductance L_h, which is determined as a function of the magnetising current I_μ ($L_\mathrm{h} = f(I_\mu)$). The required MMFs in the tooth and yoke regions of stator and rotor and across the air gap, which correspond to given magnetic flux densities in the air gap, are therefore to be computed.

For each chosen value for the magnetic flux density in the air gap, the required MMF across the air gap is determined. The effect of the slotting of the stator and the rotor is considered by virtually increasing the air gap length (by *Carter factors* for the stator and the rotor). Similarly, the MMF in the stator and the rotor teeth is computed with the help of the actual BH-curve of the electrical steel.

The effect that a part of the flux bypasses the teeth across the slots in highly saturated teeth is included by treating both paths as parallel magnetic reluctances and adding both fluxes (iterative calculation, see e.g. [99]). The MMF in the yokes is estimated according to [14] by assuming a sinusoidal magnetic flux density and by integrating the corresponding values of the magnetic field strength over one pole pitch.

The distribution and the pitching of the double-layer winding are included by scaling the computed induced voltage with a combined winding factor.

The implemented calculation of the magnetic circuit and the magnetising inductance is consequently a combination of the methods provided in [7, 14, 96, 100].

3.3.2 Iron losses

Solving the magnetic circuit for a given operating point yields the peak values of the magnetic flux densities in the yoke and teeth regions of both, the stator and the rotor, which allows to determine the iron losses according to Sec. 1.3.2.

In accordance with [7,14], correction coefficients of 1.8 and 1.5 (Sec. 1.3.2, accounting for manufacturing effects, i.e. burrs, stresses as well as stray no-load losses) are chosen for the tooth and the yoke regions respectively.

It may be noted—with respect to the complexity of the non-fundamental loss determination and also with reference to the additional load losses in Sec. 3.3.4—that there are no exact rules but (differing) guidelines concerning how to differentiate between the different loss sources according to their causes and their spatial occurrence. The implemented loss calculation and (spatial) loss separation is a combination of [3, 7, 14, 20].

The equivalent resistance of iron losses R_FE in Fig. 3.3 can be determined from the resulting overall iron losses.

3.3.3 Joule losses

The Joule losses in the stator winding and in the rotor (cage) winding are calculated with the currents through the windings (I_1 & I_2) and their resistances (R_1 & R_2). The linear temperature coefficients $\alpha_{20,\mathrm{Co}}$ and $\alpha_{20,\mathrm{Al}}$ are used to account for the temperature dependency of the resistivity of copper and aluminium and thus of the Joule losses.

Following the thermal model (Fig. 3.4) with average stator slot, rotor bar, end winding, and end ring nodes, the Joule losses in the stator and in the rotor are separated into Joule losses in the slots and the bars and Joule losses in the end windings and in the end rings at the NDE and DE sides. The different losses are determined with the corresponding parts of the winding resistances (adjusted by the local temperatures) and the currents.

3.3.4 Additional load losses

The **additional load losses** P_{add} are calculated according to IEC 60349-3 [6] with

$$P_{\mathrm{add}} = 0.01\, P_{\mathrm{ra}}\, \frac{50\,\mathrm{Hz}}{f_{\mathrm{ra}}} \left(\frac{I_1}{I_{\mathrm{ra}}}\right)^2 \left(\frac{f_1}{50\,\mathrm{Hz}}\right)^{3/2}, \tag{3.2}$$

where

P_{ra}	rated input power,
f_{ra}	rated stator frequency,
I_1	stator current,
I_{ra}	rated stator current,
f_1	stator frequency.

Using $P_{\mathrm{add}} = 3R_{\mathrm{add}}\, {I_1}^2$, an equivalent resistance R_{add} (see Fig. 3.3) may be defined similarly to the additional losses in [12]

$$R_{\mathrm{add}} = \frac{P_{\mathrm{ra}}}{300\, {I_{\mathrm{ra}}}^2}\, \frac{50\,\mathrm{Hz}}{f_{\mathrm{ra}}} \left(\frac{f_1}{50\,\mathrm{Hz}}\right)^{3/2}. \tag{3.3}$$

Based on [3, 20], 70 % of the additional load losses are assigned to the rotor (50 % to the bars & 20 % to the rotor teeth) and 30 % to the stator (20 % to the stator winding & 10 % to the stator teeth).

3.3.5 Mechanical losses

Bearing losses

The frictional losses in the bearings are determined according to Sec. 1.3.5, using Eq. (1.9). Good lubrication and normal operating conditions (according to [21, 22,

25]) are assumed and the corresponding single coefficients of friction are taken from the bearing catalogues [21, 22].

Sealing losses

The generated losses in both sealing rings are estimated with Eq. (1.8). Values for k_{s1}, k_{s2}, β_s, and d_s for similar sealing types are taken from bearing catalogues [21, 22].

Ventilation losses

The calculation of the ventilation losses is based on Eq. (1.10). The friction coefficient c_{fr} is determined with the correlations provided in [7] for different rotational speeds (Reynolds numbers).

The results, which may be regarded as very rough first estimates show, however, that the ventilation losses are comparably small due to the moderate rated rotational speed of the tested motor.

3.3.6 Losses from adjacent components

A planetary gear set is connected to the electric machine on the drive-end side. The measured frictional losses are included as three-dimensional arrays (loss variation with load, rotational speed and temperature) in the corresponding data container of the input structure array.

3.3.7 Thermal machine model

Mathematical problem

The mathematical description of an analytic thermal machine model with n nodes and

- the corresponding average temperatures $(\vartheta_1, \vartheta_2, ...\vartheta_n)$,
- the loss injections at each node $(P_1, P_2, ...P_n)$,
- the lumped thermal capacitances connected to each node $(C_{th,1}, C_{th,2}, ...C_{th,n})$, and
- the thermal conductances $(G_{1,1}, G_{1,2}, ...G_{1,n}, G_{2,1}, ...G_{2,n}, ...G_{n,1}, ...G_{n,n})$

is

$$\frac{d\vec{\vartheta}(t)}{dt} = \mathbf{C}^{-1}\vec{P} - \mathbf{C}^{-1}\mathbf{G}\,\vec{\vartheta}(t), \tag{3.4}$$

where

$$\mathbf{C} = \begin{pmatrix} C_{\mathrm{th},1} & 0 & \cdots & 0 \\ 0 & C_{\mathrm{th},2} & \ddots & \vdots \\ \vdots & \ddots & \ddots & 0 \\ 0 & \cdots & 0 & C_{\mathrm{th,n}} \end{pmatrix}, \tag{3.5}$$

$$\mathbf{G} = \begin{pmatrix} G_{1,1} & G_{1,2} & \ldots & G_{1,\mathrm{n}} \\ G_{2,1} & G_{2,2} & \ldots & G_{2,\mathrm{n}} \\ \vdots & \vdots & \ddots & \vdots \\ G_{\mathrm{n},1} & \ldots & \ldots & G_{\mathrm{n,n}} \end{pmatrix}, \tag{3.6}$$

$$\frac{d\vec{\vartheta}(t)}{dt} = \begin{pmatrix} \frac{d\vartheta_1(t)}{dt} \\ \frac{d\vartheta_2(t)}{dt} \\ \vdots \\ \frac{d\vartheta_\mathrm{n}(t)}{dt} \end{pmatrix}, \tag{3.7}$$

$$\vec{\vartheta}(t) = \begin{pmatrix} \vartheta_1(t) \\ \vartheta_2(t) \\ \vdots \\ \vartheta_\mathrm{n}(t) \end{pmatrix}, \tag{3.8}$$

$$\vec{P} = \begin{pmatrix} P_1 \\ P_2 \\ \vdots \\ P_\mathrm{n} \end{pmatrix}. \tag{3.9}$$

In the stationary case $\left(\frac{d\vec{\vartheta}(t)}{dt} = 0\right)$, Eq. (3.4) reduces to

$$\vec{\vartheta} = \mathbf{G}^{-1}\,\vec{P}. \tag{3.10}$$

The elements of the conductance matrix are calculated from the thermal conductances between the nodes as follows

$$\begin{aligned} P_1 &= g_{1,2}\,(\vartheta_1 - \vartheta_2) + g_{1,3}\,(\vartheta_1 - \vartheta_3) + \ldots + g_{1,\mathrm{n}}\,(\vartheta_1 - \vartheta_n) \\ &= \underbrace{(g_{1,2} + g_{1,3} + \ldots + g_{1,\mathrm{n}})}_{G_{1,1}}\,\vartheta_1 \underbrace{-g_{1,2}}_{G_{1,2}}\,\vartheta_2 \underbrace{-g_{1,3}}_{G_{1,3}}\,\vartheta_3 - \ldots \underbrace{-g_{1,\mathrm{n}}}_{G_{1,\mathrm{n}}}\,\vartheta_n. \end{aligned} \tag{3.11}$$

The elements of the main diagonal of the conductance matrix have positive values, while the entries outside the main diagonal are either zero (no direct thermal connection) or have negative values (direct thermal flow path between nodes).

The heat flow path between the coolant (node 0) and e.g. node 1 with the corresponding thermal conductance $g_{1,0}$ is modelled by adding $(\vartheta_1 - \vartheta_0)\, g_{1,0}$ to the right side of Eq. (3.11), leading to additional terms for $G_{1,1}$ ($+g_{1,0}$) and P_1 ($+g_{1,0}\, \vartheta_0$).

Induction machine model

The thermal lumped parameter model of the induction machine is shown in Fig. 3.4. The complete model consists of 20 nodes (an additional node implemented for possible consideration of loss injections into the shaft at the DE side). The numbering of the nodes and the naming of the thermal resistances directly follows the naming in the MATLAB code.

The model, including the thermal resistances as well as the underlying modelling concepts and assumptions, is explained in detail in Sec. 3.5.

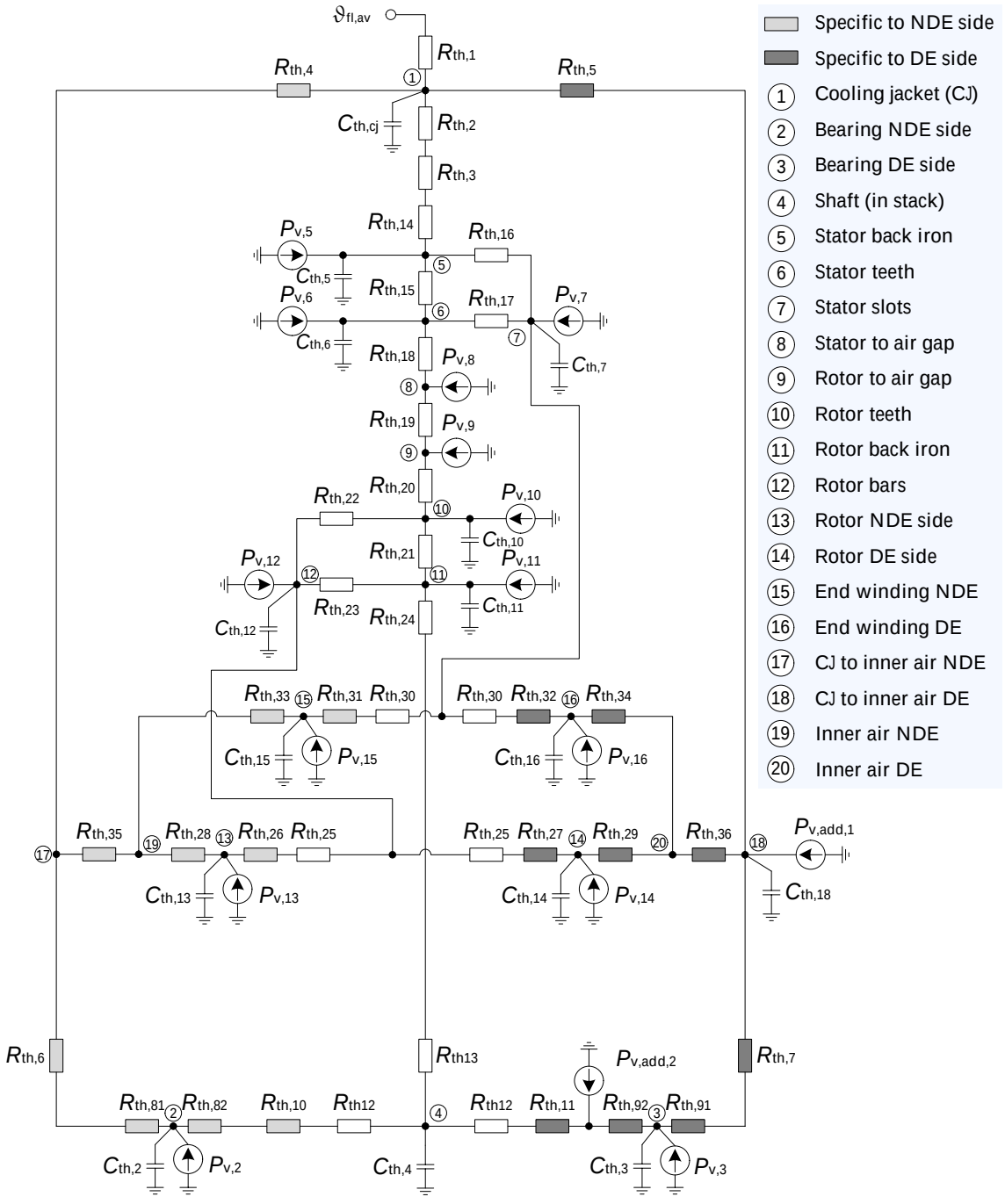

Figure 3.4: Thermal lumped parameter model of the induction machine in Fig. 3.1.

3.4 Numerical modelling framework

The CAD model of the electric machine assembly, which is used for the thermal simulation, is given in Fig 3.5. The model comprises (i) the rotor (with the rotor stack, the rotor bars and two end rings), (ii) the shaft, (iii) the stator (with the stator stack, the windings in the slots and the two end windings) and (iv) the cooling jacket. Additionally, the thermal model consists of two layered air gap parts in the air gap regions, two air parts in the end winding regions and a parts for the fluid in the channels of the cooling jacket.

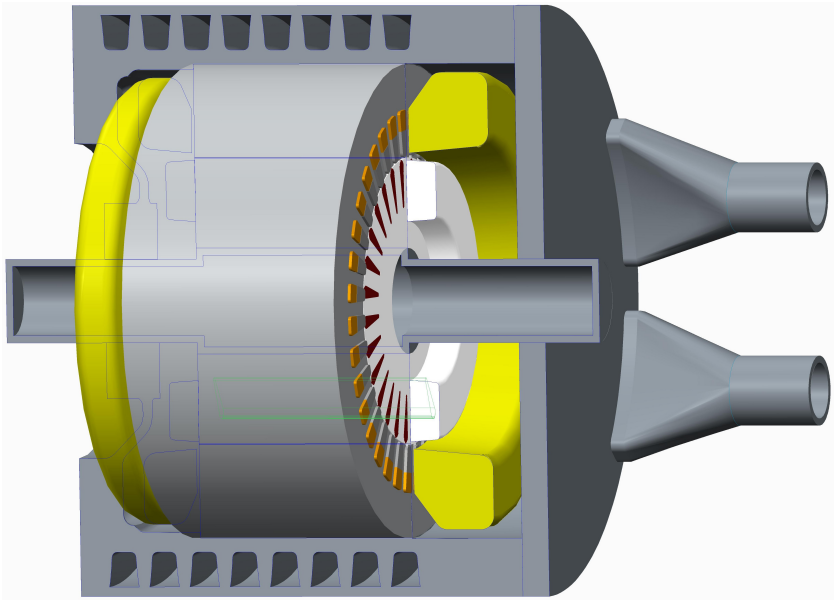

Figure 3.5: Cut-open view of the 3D CAD machine assembly.

The required steps and the software tools needed to build the 3D CAD model and the workflow to analyse its thermal behaviour are illustrated in Fig. 3.6. The electromagnetic simulations are carried out with a 2D CAD model of the electric machine with the software JMAG. The 2D CAD model and the calculated loss distribution are extruded to the axial machine length. The extruded CAD model is exported to an ACIS SAT file (.sat), extruded mesh and the associated losses are written to a Nastran file (.nas).

The shaft, the end windings, the end rings and the housing are created or edited in CREO and the complete machine model is assembled and exported to an IGES file (.igs). The bearings are not explicitly modelled but considered in the thermal simulation by equivalent contact interfaces (Sec. 2.6).

The assembly is first imported into the CAD modeller of STAR-CCM+. The bodies are then imprinted and invalid surfaces repaired. The inner air body and the

coolant body are extracted and the interfaces between all contacting bodies are created. The surface mesh and the volume mesh are generated subsequently during the preprocessing. The extruded mesh and the associated losses from JMAG are finally imported into STAR-CCM+ and—because of the different meshes—mapped onto the 3D mesh in STAR-CCM+.

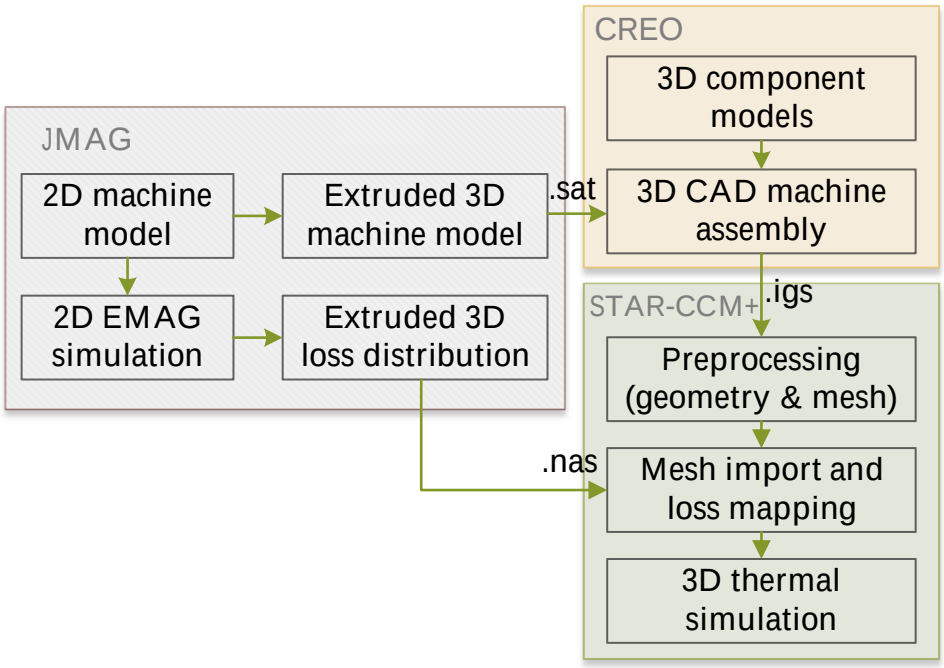

Figure 3.6: Software framework and file-based coupling.

3.4.1 Electromagnetic modelling and loss modelling

Transient electromagnetic (EMAG) simulations of a 2D $\frac{1}{4}$ machine model are used to determine the iron losses in the electrical steel. The implemented iron loss calculation routine of the EMAG FEM software determines the iron losses in a post-processing operation of the magnetic field analysis, using the calculated time series values of the magnetic flux density for each element and the specific iron losses from the material database. The determined total iron losses are the sum of the hysteresis losses and the eddy current losses in the electrical steel. Details on the actual implementation may be found in [44]. An exemplary iron loss simulation may be seen in Fig. 3.8(a).

The loss distribution of the $\frac{1}{4}$ model is then converted (copied) and extruded to a full 3D model. The losses in the stator winding and in the end rings are directly modelled by loss sources (spatially uniform loss distributions) in the thermal 3D model due to their three-dimensional shapes.

The skewing of the rotor is not modelled since this would require building and solving a 3D EMAG model. The calculation of the iron losses in the rotor in the 3D model would lead to comparably long computation times (at least several days) because of the required number of time steps (short time steps over one period of the slip frequency).

3.4.2 Thermal modelling

The thermal machine model comprises all components of the CAD model of the machine assembly in Fig. 3.5 as well as the extracted bodies of the inner air and of the coolant in the cooling jacket, which are generated during the pre-processing.

After the import of the CAD model into the CFD software, several pre-processing steps are required. The imported bodies are imprinted and overlapping faces, free edges and other errors in the surface topology are corrected. Different so-called *physics continua* are defined, which include the specification of material properties and the solver modules. The different bodies are then associated with *regions*, which include the link to the related physics continuum. To give an example, the different aluminium bar bodies are linked to the same *bar region* and thus also to the same physics continuum. Boundary conditions (e.g. loss input and flow rates) as well as all interfaces are defined on the *region level*.

Since completely different *meshers* are generally available, each region is linked to a *mesh continuum*, which specifies the used meshing modules and specific meshing parameters. One and the same mesh continuum is used for all regions in the following in order to generate a conformal mesh. Particular attention is required for the meshing of the air gap as several element layers are needed to resolve the air flow in the comparably very small air gap. Yet, if the element size is simply reduced uniformly, the number of elements would be very high (tens of millions of elements for the complete model). Therefore, thin elements are grown from the contacting solids (stator and rotor stack and stator winding and rotor bars) into the air gap, yielding thin layered elements and reducing the number of required elements.

The generated conformal volume mesh with a total of $8.6 \cdot 10^6$ elements is shown in Fig. 3.7. The prismatic layers in the cooling channels and in the air volume in the end winding region may be seen clearly at the boundaries to the contacting solids.

The imported losses from the EMAG calculation (with a mesh consisting of uniform triangular prisms) are mapped onto the polyhedral mesh, as shown in the example in Fig. 3.8. The mapped imported loss distributions are then assigned to the corresponding regions as volumetric heat sources.

The losses in the stator winding and in the end rings are directly modelled in

STAR-CCM+ by volumetric heat sources.

The rotation is modelled by a moving reference frame approach in the air gap and by tangential velocity specifications at the interfaces to the rotating solids outside the air gap (for more details see [39, 94]).

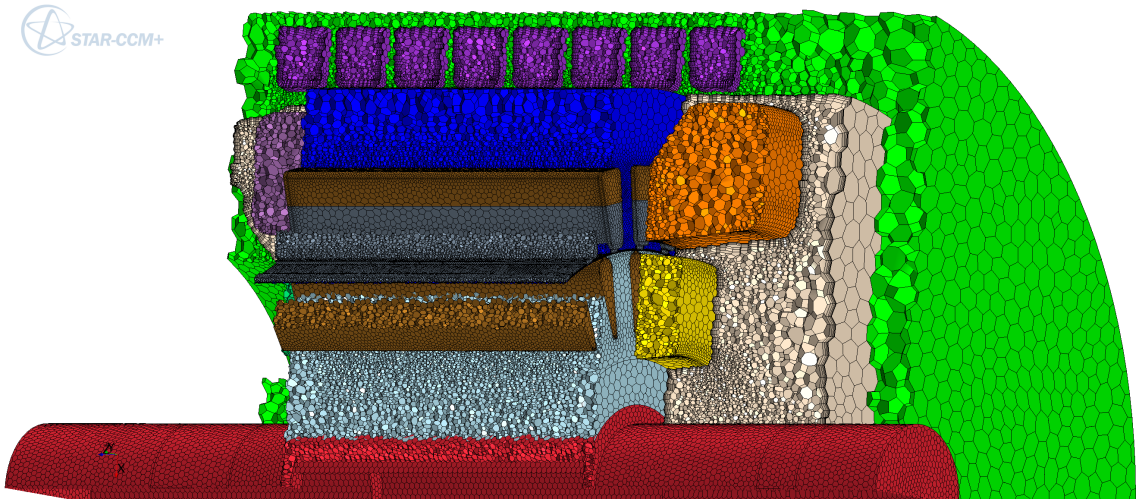

Figure 3.7: Cut-open view of mesh of complete machine assembly.

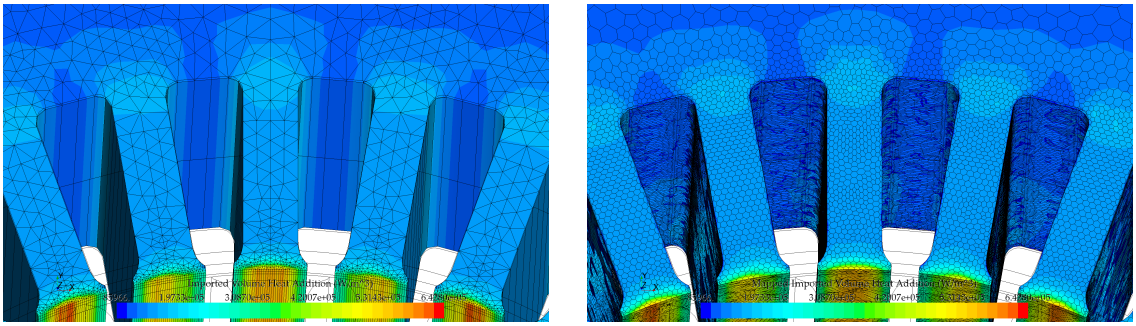

(a) Imported losses

(b) Mapped losses

Figure 3.8: Exemplary loss mapping.

The electric machine is placed under a protective cover during the experimental tests, limiting the temperature difference between the surrounding air underneath the cover and the outer housing surface and thus also the convective heat transfer. Considering the fact that the average convective heat transfer is well below 10 $\frac{\mathrm{W}}{\mathrm{m^2\,K}}$ (Sec. 2.2 and also [34]) and that the temperature difference does not exceed a few degrees Celsius, convective heat transfer between the outer housing surface and the surrounding air is negligible (compared with convective heat transfer to the coolant) in the studied case and it is consequently neither modelled in the analytic nor in the numerical model. Exemplary numerical simulations (in conjunction with the mea-

sured temperatures) proved that no significant effect on the temperature distribution could be observed when modelling convection from the outer housing surface to the enclosed air. Since the temperature of the enclosed air is slightly higher than the outer surface of the cooling jacket during the experimental testing on the test bench, heat would in fact be transferred from the air to the housing.

Radiation is neglected in the analytic model but the locked-rotor test is simulated numerically with and without radiation in Sec. 3.6.2. This experimental test with its comparably high rotor temperature and the reduced complexity with regard to the acting heat sources is a good example for studying how much radiative heat transfer may affect the heat transfer and the temperatures in the electric machine.

3.5 Thermal component models

In the following, the thermal models of the analytic model in Fig. 3.4 as well as of the numerical model in Fig. 3.5 are explained jointly for each component. As stated in Sec. 3.2, certain thermal resistances may require adjustments based on measurements. Therefore, typical values are used as initial estimations in these cases. The experimental tests in Sec. 3.2 are then used to validate or adjust the estimated values in Sec. 3.6.

The approach to present and review the obtained simulation results with the initial parameters before making any adjustments targets at illustrating possible causes and effects, which would not be possible if only final results were presented.

In addition to certain thermal resistances, which may require adjustments, the losses (being the input of the simulations) have a direct and very significant influence on the temperature output. In case the analytically estimated and the numerically determined losses differ significantly—which is expected to lead to different results in such cases—the results are presented and discussed prior to any adjustments.

3.5.1 Cooling jacket

The cooling jacket is comparable with the analysed cooling jacket in Sec. 2.2. During the experimental test, significantly lower flow rates (around 11 $\frac{\mathrm{l}}{\mathrm{min}}$) are used, leading to laminar flow in certain regions in the cooling channels. Using empirical correlations for the non-circular channels may therefore lead to significant inaccuracies. Consequently, the heat transfer coefficient is not determined from correlations but the thermal resistance is directly derived from CFD simulations.

The thermal resistance between the interface to the coolant and the coolant $R_{th,1}$ as well as the thermal resistance between the inner surface of the cooling jacket (which is in contact with the back iron of the stator) and the interface to the coolant $R_{th,2}$ are determined from the corresponding temperature drops divided by the transferred heat. $R_{th,2}$ may, of course, be estimated analytically but is instead derived from numerical simulations for reasons of simplicity (same simulation that is used to determine $R_{th,1}$). The thermal capacitance of the cooling jacket $C_{th,cj}$ is determined with the specific heat of the aluminium housing and the mass density.

$R_{th,1}$, $R_{th,2}$ and the thermal capacitance of the housing $C_{th,cj}$ in the lumped parameter model in Fig. 3.4 are

$$R_{th,1} = 3.12 \cdot 10^{-3} \frac{\mathrm{K}}{\mathrm{W}}, \tag{3.12}$$

$$R_{th,2} = 3.78 \cdot 10^{-3} \frac{\mathrm{K}}{\mathrm{W}}, \text{ and} \tag{3.13}$$

$$C_{th,cj} = 7560 \frac{\mathrm{J}}{\mathrm{K}}. \tag{3.14}$$

If the thermal resistance due to convection is determined with the correlation used in [46], the resulting value would be $0.0127 \frac{\mathrm{K}}{\mathrm{W}}$, which is more than four times as high as the value in Eq. (3.12), which is derived from the numerical simulation. This confirms that standard correlations for circular channels are not applicable in this case.

The conductive thermal resistances between the interface to the coolant and the bearings on the NDE side ($R_{th,4}$ for the axial flow path, $R_{th,6}$ for the radial flow path) and the DE side ($R_{th,5}$ for the axial flow path, $R_{th,7}$ for the radial flow path) are determined with the geometry of the flow paths and the thermal conductivity of the water jacket

$$R_{th,4} = 1.95 \cdot 10^{-2} \frac{\mathrm{K}}{\mathrm{W}}, \tag{3.15}$$

$$R_{th,5} = 2.69 \cdot 10^{-3} \frac{\mathrm{K}}{\mathrm{W}}, \tag{3.16}$$

$$R_{th,6} = 3.03 \cdot 10^{-1} \frac{\mathrm{K}}{\mathrm{W}}, \text{ and} \tag{3.17}$$

$$R_{th,7} = 2.69 \cdot 10^{-1} \frac{\mathrm{K}}{\mathrm{W}}. \tag{3.18}$$

The convective heat transfer at the interfaces between the inner air in the end winding regions and the inner surfaces of the cooling jacket at both machine ends is modelled by the two thermal resistances $R_{th,35}$ (NDE side) and $R_{th,36}$ (DE side) in the analytic model. Similar to the modelling of convection at the end windings in [46] (Fig. 2.23(b)), the interfaces of the cooling jacket at both sides are split into

two sub-interfaces in order to account for the expected significantly different reference velocities. The interface in Fig. 2.24 may be split into an interface that corresponds to the straight housing surface (along the motor axis) and into an interface that corresponds to the finned end cap surface (perpendicular to motor axis).

The convective heat transfer coefficients and the corresponding thermal resistances are determined separately with Eqs. (2.68) and (1.22) for both sub-interfaces and combined to one resulting thermal resistance per motor sides.

Generally, the heat transfer coefficients and consequently the thermal resistance depend on the motor speed.

$$R_{\mathrm{th},35} = R_{\mathrm{th,conv}}(n) \text{ and} \tag{3.19}$$

$$R_{\mathrm{th},36} = R_{\mathrm{th,conv}}(n). \tag{3.20}$$

With the default parameter set from [46] ($k_{\mathrm{cc},1} = 15$, $k_{\mathrm{cc},2} = 0.4$, $k_{\mathrm{cc},3} = 0.9$), the values of the thermal resistances are at rated speed

$$R_{\mathrm{th},35} = 0.476 \, \frac{\mathrm{K}}{\mathrm{W}} \text{ and} \tag{3.21}$$

$$R_{\mathrm{th},36} = 0.511 \, \frac{\mathrm{K}}{\mathrm{W}}. \tag{3.22}$$

3.5.2 Bearings

The thermal resistances of the bearings are estimated with the approach presented in Sec. 2.6.2, which is based on ISO standard 15312 [24]. As explained in Sec. 2.6.2, an experimental determination would also only be an approximation due to the numerous side effects. An experimental determination of the bearing resistances would anyway not be possible with the studied electrical machine for practical reasons (no temperature sensors at the bearing seats).

The standard reference heat flow density for radial bearings given in ISO standard 15312 (Fig. 2.19) is used to calculate the thermal resistances that are related to both (the inner and the outer) bearing seating surfaces of both bearings in the analytic model. The thermal resistances of both bearings are consequently modelled by sub-resistances according to the seating surfaces in the analytic models (NDE: $R_{\mathrm{th},81}$ & $R_{\mathrm{th},82}$, DE: $R_{\mathrm{th},91}$ & $R_{\mathrm{th},92}$).

In order to simplify the mesh generation and the analysis, the bearings are not modelled explicitly in the numerical model. The housing with its comparably high thermal conductivity is extruded to cover the volume of the bearings, which hardly affects the thermal behaviour due to the comparably high thermal conductivity of the aluminium housing compared with the bearings. The resistances of the bearings

are modelled by equivalent contact resistances between the housing and the shaft on both machine sides. Consequently, only half the reference heat flow density of the analytic model is used since the bearings are modelled by one contact resistance with the contact area being approximately the average of the inner and the outer seating surface.

The thermal capacitances are determined with the specific heat and the masses of the bearing components.

$$R_{\mathrm{th},81} = 2.83\,\frac{\mathrm{K}}{\mathrm{W}} \tag{3.23}$$

$$R_{\mathrm{th},82} = 3.89\,\frac{\mathrm{K}}{\mathrm{W}} \tag{3.24}$$

$$R_{\mathrm{th},91} = 2.35\,\frac{\mathrm{K}}{\mathrm{W}} \tag{3.25}$$

$$R_{\mathrm{th},92} = 3.68\,\frac{\mathrm{K}}{\mathrm{W}} \tag{3.26}$$

$$C_{\mathrm{th},2} = 6.65\,\frac{\mathrm{J}}{\mathrm{K}} \tag{3.27}$$

$$C_{\mathrm{th},3} = 23.3\,\frac{\mathrm{J}}{\mathrm{K}} \tag{3.28}$$

3.5.3 Shaft

The shaft is simplified geometrically in both the numerical and the analytic model as the comparably small details, e.g for the fixation of the rotor stack, do not significantly influence the thermal behaviour. For modelling reasons (problems with the interface definition), the thickness of the hollow shaft is smaller in the CAD model than the average thickness of the used shaft. This is corrected by an increased value of the thermal conductivity in the numerical model.

As shown in Sec. 2.7, the thermal resistance of the shaft is split into three subresistances in the analytic model, namely $R_{\mathrm{th},10}$, $R_{\mathrm{th},11}$ and $R_{\mathrm{th},12}$ in Fig. 3.4.

$R_{\mathrm{th},10}$ and $R_{\mathrm{th},11}$ are the thermal resistances of the shaft between the bearings and the rotor stack. The thermal resistances are calculated from the axial length of the flow paths and the thickness of the shaft. $R_{\mathrm{th},12}$ is the thermal resistance of the shaft inside the rotor stack to the average temperature level.

The mathematical problem of modelling the asymmetric, multi-dimensional heat transfer in the shaft analytically is complicated further by the connected rotor stack, the slight convective heat transfer from the shaft and the uncertainty related to the thermal resistance of the bearings. The length of the thermally conductive path in the rotor stack to each stack end is consequently simply modelled by one half of

the axial flow path, i.e. one quarter of the stack length in both directions (similar to Eq. (2.64)). This choice showed relatively good agreement with the numerical results in Sec. 2.7.1.

The thermal capacitance $C_{\text{th},4}$ is connected to the average temperature node in the stack. Depending on the temperature gradients of the shaft, it may be advisable to investigate the effect of splitting up the single capacitance into three capacitances (one in the rotor stack and one connected between the rotor stack and the bearings on each side).

$$R_{\text{th},10} = 0.897 \frac{\text{K}}{\text{W}} \tag{3.29}$$

$$R_{\text{th},11} = 0.657 \frac{\text{K}}{\text{W}} \tag{3.30}$$

$$R_{\text{th},12} = 0.470 \frac{\text{K}}{\text{W}} \tag{3.31}$$

$$C_{\text{th},4} = 597 \frac{\text{J}}{\text{K}} \tag{3.32}$$

3.5.4 Contact resistances

The thermal contact resistance between the water jacket and the stator stack $R_{\text{th},3}$ is calculated with $h_{\text{intf}} = 1500 \frac{\text{W}}{\text{m}^2\,\text{K}}$, an average value according to the ranges given in Table 2.1. The contact resistance is modelled similarly in the numerical model.

$$R_{\text{th},3} = 1.56 \cdot 10^{-2} \frac{\text{K}}{\text{W}} \tag{3.33}$$

It may be noted that the thermal contact resistance between the stator stack and the cooling jacket has a very significant influence on the temperatures inside the electric machine since by far most of the internally generated heat is transferred across this thermal resistance. It is therefore highly recommended to verify the chosen value (and also the other contact resistances) by experimental tests such as DC tests. The verification by experimental tests is illustrated in Sec. 3.6.

The thermal contact resistance between the shaft and the rotor stack $R_{\text{th},13}$ is calculated with an average value for h_{intf} from Table 2.1 ($h_{\text{intf}} = 1800 \frac{\text{W}}{\text{m}^2\,\text{K}}$)

$$R_{\text{th},13} = 5.82 \cdot 10^{-2} \frac{\text{K}}{\text{W}}. \tag{3.34}$$

It is obvious from the comparison between Eq. (3.34) and the thermal resistances of the shaft (Eqs. (3.29)–(3.31)) and the bearings (Eqs. (3.23)–(3.26)) that the contact resistance between the rotor stack and the shaft only has a very limited influence on the thermal behaviour.

$h_{\text{intf}} = 2000\,\frac{\text{W}}{\text{m}^2\,\text{K}}$ is chosen for the thermal interface conductance between the rotor stack and the rotor bars, resulting in the contact resistance

$$R_{\text{th}} = 5.93 \cdot 10^{-3}\,\frac{\text{K}}{\text{W}}, \tag{3.35}$$

which is, analogous to the extended model in Sec. 2.3.6, split into two (parallel) sub-resistances in Sec. 3.5.7 for inclusion in $R_{\text{th},22}$ (thermal resistances between the rotor bars and the rotor teeth) and $R_{\text{th},23}$ (thermal resistance between the rotor bars and the rotor back iron).

3.5.5 Stator stack and stator slots

The stator slots are modelled by a single body representation with uniform properties (in both the numerical as well as in the analytic model), similar to the simplified model in Sec. 2.3.5. The voids in the impregnation are accounted for by an adjusted (reduced) value of the thermal conductivity according to the impregnation goodness provided by the machine manufacturer. Since no detailed slot model is available, which would allow to correctly determine an equivalent average thermal conductivity, the average thermal conductivity is approximated based on the results in Sec. 2.3.5 by using the mean value of the volumetric average and the value obtained with Eq. (2.27) ($\lambda_{\text{av}} = 0.786\,\frac{\text{W}}{\text{m}\,\text{K}}$).

The analytic modelling of the stator stack and the stator slots is based on the extended model introduced in Sec. 2.3.6, which showed relatively good agreement with the numerical results.

$R_{\text{th},14}$ is consequently the (radial) thermal resistance of the stator back iron, $R_{\text{th},15}$ and $R_{\text{th},18}$ are half the (radial) thermal resistance of the stator teeth each. $R_{\text{th},16}$ and $R_{\text{th},17}$ denote the thermal resistances between stator back iron and the stator slots and between the stator teeth and the stator slots respectively.

In the analytic model, axial heat flow in the stator slots is modelled according to Sec. 2.7 by thermal conduction in the copper wires with internal heat generation. The thermal resistance $R_{\text{th},30}$ models the conductive path between the slot node and the stack end at each motor side.

Anisotropic material properties are used for the electrical steel in the numerical model, accounting for the insulating coating in the heat flow path in axial direction in the stator (and in the rotor) stack.

The thermal capacitances $C_{\text{th},5}$ (stator back iron), $C_{\text{th},6}$ (stator teeth) and $C_{\text{th},7}$ (stator slot, i.e. copper and insulation materials) are calculated with the volumes, the mass densities and the specific heat of each component.

$$R_{\text{th},14} = 1.55 \cdot 10^{-2} \frac{\text{K}}{\text{W}} \tag{3.36}$$

$$R_{\text{th},15} = 2.26 \cdot 10^{-2} \frac{\text{K}}{\text{W}} \tag{3.37}$$

$$R_{\text{th},16} = 1.72 \cdot 10^{-1} \frac{\text{K}}{\text{W}} \tag{3.38}$$

$$R_{\text{th},17} = 3.11 \cdot 10^{-2} \frac{\text{K}}{\text{W}} \tag{3.39}$$

$$R_{\text{th},18} = 2.26 \cdot 10^{-2} \frac{\text{K}}{\text{W}} \tag{3.40}$$

$$R_{\text{th},30} = 2.48 \cdot 10^{-2} \frac{\text{K}}{\text{W}} \tag{3.41}$$

$$C_{\text{th},5} = 2250 \frac{\text{J}}{\text{K}} \tag{3.42}$$

$$C_{\text{th},6} = 900 \frac{\text{J}}{\text{K}} \tag{3.43}$$

$$C_{\text{th},7} = 716 \frac{\text{J}}{\text{K}} \tag{3.44}$$

3.5.6 Air gap

In the numerical model, fluid flow and heat transfer are directly calculated by the CFD solver. In the analytic model, the air gap is modelled by the thermal resistance $R_{\text{th},19}$. The required Nusselt number (Eq.(1.24)) is calculated with the correlations provided in [50]

$$Nu = \begin{cases} 2 & \text{if } Ta < 41, \\ 0.212\, Ta^{0.63}\, Pr^{0.27} & \text{if } 41 \leq Ta < 100, \\ 0.386\, Ta^{0.5}\, Pr^{0.27} & \text{if } 100 \leq Ta. \end{cases} \tag{3.45}$$

where

$Ta = Re\sqrt{\frac{\delta}{r_{\text{r,o}}}}$	Taylor number,
$r_{\text{r,o}}$	outer radius of the rotor,
δ	length of air gap (in radial direction).

Pr is determined with Eq. (1.19), Re is determined with Eq. (1.11) and $R_{\text{th},19}$ with Eq. (1.22). $R_{\text{th},19}$ is a function of the rotational speed but its value also depends on the temperature as the thermal conductivity, the specific heat, the kinematic viscosity and the dynamic viscosity vary with temperature [34]. Using the correct material properties that match the temperature is ensured by interpolation since all material

properties, which vary significantly with temperature, are saved as look-up tables in the input structure.

The thermal capacitance of the air gap is neglected as its value is well below 1 $\frac{\mathrm{J}}{\mathrm{K}}$.

3.5.7 Rotor stack, rotor bars and end rings

The modelling of the rotor follows the stator modelling in Sec. 3.5.5, with the exception that the rotor winding, which consists of solid bars, does not require the definition of an equivalent thermal conductivity. Similarly, the extended analytical modelling approach in Sec. 2.3.6 is also used for the rotor bars.

Axial heat flow is neglected in the rotor stack in the analytic model (Sec. 2.3.3). In the numerical model, however, anisotropic material properties (thermal conductivity) of the electrical steel allow to account for axial heat flow in the rotor stack.

$R_{\mathrm{th},24}$ is the (radial) thermal resistance of the rotor back iron, $R_{\mathrm{th},20}$ and $R_{\mathrm{th},21}$ are each half the (radial) thermal resistance of the rotor teeth. $R_{\mathrm{th},22}$ and $R_{\mathrm{th},23}$ denote the thermal resistances between the rotor bars and the rotor teeth and between the rotor bars and the rotor back iron.

The thermal capacitances $C_{\mathrm{th},10}$ (rotor teeth), $C_{\mathrm{th},11}$ (rotor back iron) and $C_{\mathrm{th},12}$ (rotor bars) are calculated with the volumes, the mass densities and the specific heat of each component.

$$R_{\mathrm{th},20} = 2.24 \cdot 10^{-2}\,\frac{\mathrm{K}}{\mathrm{W}} \tag{3.46}$$

$$R_{\mathrm{th},21} = 2.24 \cdot 10^{-2}\,\frac{\mathrm{K}}{\mathrm{W}} \tag{3.47}$$

$$R_{\mathrm{th},22} = 4.77 \cdot 10^{-2}\,\frac{\mathrm{K}}{\mathrm{W}} \tag{3.48}$$

$$R_{\mathrm{th},23} = 6.86 \cdot 10^{-3}\,\frac{\mathrm{K}}{\mathrm{W}} \tag{3.49}$$

$$R_{\mathrm{th},24} = 4.19 \cdot 10^{-2}\,\frac{\mathrm{K}}{\mathrm{W}} \tag{3.50}$$

$$C_{\mathrm{th},10} = 696\,\frac{\mathrm{J}}{\mathrm{K}} \tag{3.51}$$

$$C_{\mathrm{th},11} = 903\,\frac{\mathrm{J}}{\mathrm{K}} \tag{3.52}$$

$$C_{\mathrm{th},12} = 298\,\frac{\mathrm{J}}{\mathrm{K}} \tag{3.53}$$

The contact resistance between the bars and the stack (Sec. 3.5.4) presents 99 % of the thermal resistance in the heat flow path between the bars to the rotor stack. Therefore, heat conduction in the aluminium in non-axial direction may be neglected.

The axial thermal resistance $R_{\text{th},25}$ between the average rotor bar node and each stack end is modelled according to Sec. 2.7. Axial heat transfer is only modelled through the aluminium bars as a one-dimensional heat transfer problem with spatially uniform heat generation.

Due to the fact that the thermal resistance of the end rings is significantly smaller than the thermal resistance of the rotor bars (the combined axial thermal resistance of both end rings is less than 8 % of the axial thermal resistance of the rotor bars) and even smaller compared with the thermal resistances for convection to the inner air (at $n = 0.1\,\text{pu}$ and with $k_{\text{cc},1} = 15$, $k_{\text{cc},2} = 0.4$, $k_{\text{cc},3} = 0.9$ (Sec. 2.8), the ratio between the complete axial end ring resistance and the resistance of convection to the inner air is 0.9 %), the simplified modelling of the end rings, which will be explained in the following, is not expected to have a noticeable effect on the overall accuracy.

Heat transfer in the end rings is modelled as one-directional heat transfer with internal heat generation between the end ring interfaces to the inner air and the interfaces to the rotor bars ($R_{\text{th},26}$ and the conductive part of $R_{\text{th},28}$ at the NDE side as well as $R_{\text{th},27}$ and the conductive component of $R_{\text{th},29}$ at the DE side).

$R_{\text{th},26}$ and $R_{\text{th},27}$ are the thermal resistances between the rotor stack ends (at the NDE and the DE side respectively) and the end ring nodes of the corresponding side.

$R_{\text{th},28}$ and $R_{\text{th},29}$ combine heat conduction from the end ring nodes to the end ring surfaces and convection to the inner air. The general correlation in Eq. (2.68) (with the parameter set $k_{\text{cc},1} = 15$, $k_{\text{cc},2} = 0.4$, $k_{\text{cc},3} = 0.9$) is used to determine the average heat transfer coefficient. The thermal resistances for both motor sides are then calculated with Eq. (1.22). The convective resistance varies with rotational speed, which is indicated by $R_{\text{th,conv}}(n)$ in Eqs. (3.57) and (3.58). At rated rotational speed, the convective components are $0.958\,\frac{\text{K}}{\text{W}}$. Considering the different orders of magnitude compared with the conductive components in Eq. (3.57) and (3.58), the conductive components may be omitted without affecting the overall accuracy.

$$R_{\text{th},25} = 3.95 \cdot 10^{-2}\,\frac{\text{K}}{\text{W}} \tag{3.54}$$

$$R_{\text{th},26} = 2.99 \cdot 10^{-3}\,\frac{\text{K}}{\text{W}} \tag{3.55}$$

$$R_{\text{th},27} = 2.99 \cdot 10^{-3}\,\frac{\text{K}}{\text{W}} \tag{3.56}$$

$$R_{\text{th},28} = 2.99 \cdot 10^{-3}\,\frac{\text{K}}{\text{W}} + R_{\text{th,conv}}(n) \tag{3.57}$$

$$R_{\text{th},29} = 2.99 \cdot 10^{-3}\,\frac{\text{K}}{\text{W}} + R_{\text{th,conv}}(n) \tag{3.58}$$

$$C_{\text{th},13} = 149\,\frac{\text{J}}{\text{K}} \tag{3.59}$$

$$C_{\text{th},14} = 149\,\frac{\text{J}}{\text{K}} \tag{3.60}$$

3.5.8 End windings

The end windings are modelled by lumped bodies with the (smooth) envelope of the end winding defining the geometry as explained in Sec. 2.8. In contrast to the end rings (Sec. 3.5.7), the interface to the inner air is split into sub-interfaces as shown in Sec. 2.8 (Fig. 2.23(b), [46]). The convective heat transfer coefficients and the corresponding thermal resistances are determined separately for the inner, the outer and the side surface of both end windings that contact the inner air, which allows to consider the significantly different reference velocities at the interfaces, as e.g. present in Fig. 2.24.

Similar to the end rings, the heat transfer in the end windings is modelled as one-directional heat transfer with internal heat generation. The heat transfer path at the NDE side is modelled by $R_{\text{th},31}$ (flow path between stack end and end winding node) and $R_{\text{th},33}$ (end winding node and inner air). The DE side is modelled similarly by $R_{\text{th},32}$ (flow path between stack end and end winding node) and $R_{\text{th},34}$ (end winding node and inner air). $R_{\text{th},33}$ and $R_{\text{th},34}$ comprise heat conduction in the end windings and also the thermal resistances due to convection to the end winding spaces at the NDE and the DE side respectively.

In [71], $\frac{1}{4}$ of the coil length in the end winding is used to determine the thermal resistance between the end of the stator stack and the end winding node ($R_{\text{th},31}$ at the NDE side, $R_{\text{th},32}$ at the DE side). As the impregnated end windings form solid bodies and heat transfer between the different wires is expected as soon as the coil sides enter the end winding region, the axial length of the end windings is used instead of the coil length in the end windings.

At rated speed and using the parameter set $k_{\text{cc},1} = 15$, $k_{\text{cc},2} = 0.4$, $k_{\text{cc},3} = 0.9$, the convective components of $R_{\text{th},33}$ and $R_{\text{th},34}$ are 0.576 $\frac{\text{K}}{\text{W}}$ and 0.747 $\frac{\text{K}}{\text{W}}$ respectively. The convective components therefore have a dominant influence in the heat flow path from the stator slots via the end windings to the end cap air.

The thermal capacitances of the end windings at the NDE side ($C_{\text{th},15}$) and at the DE side ($C_{\text{th},16}$) are calculated using the mass and the specific heat of the copper and the insulating material.

$$R_{\text{th},31} = 1.91 \cdot 10^{-2}\,\frac{\text{K}}{\text{W}} \tag{3.61}$$

$$R_{\text{th},32} = 1.30 \cdot 10^{-2}\,\frac{\text{K}}{\text{W}} \tag{3.62}$$

$$R_{\text{th},33} = 1.91 \cdot 10^{-2} \frac{\text{K}}{\text{W}} + R_{\text{th,conv}}(n) \tag{3.63}$$

$$R_{\text{th},34} = 1.30 \cdot 10^{-2} \frac{\text{K}}{\text{W}} + R_{\text{th,conv}}(n) \tag{3.64}$$

$$C_{\text{th},15} = 395 \frac{\text{J}}{\text{K}} \tag{3.65}$$

$$C_{\text{th},16} = 395 \frac{\text{J}}{\text{K}} \tag{3.66}$$

3.5.9 Mounting to test bench

The housing of the electric machine is fixed to a robust metal construction at the DE side. The thermal capacitance of the directly connected fixation is modelled by $C_{\text{th},18}$

$$C_{\text{th},18} = 11\,200 \frac{\text{J}}{\text{K}}. \tag{3.67}$$

3.6 Model evaluation

3.6.1 DC test

Methodology

During DC tests the stator windings are fed with DC currents, the electric machine is at stand-still and no losses are generated in the rotor. Consequently, Joule losses in the stator windings are the only loss source. Such tests are therefore generally suitable to verify or adjust the thermal resistance of the heat flow path between the coil sides in the stator slots and the cooling jacket and, in particular, the slot modelling with the numerous components.

The DC test in this study differs slightly from a pure DC test in that the stator windings are fed with symmetric three-phase currents at a very low frequency ($f_1 = 0.01$ pu, further parameters are given in Table A.1 in the appendix).

This quasi-DC test—which is a work-around since the star-point connection is not accessible and constant equal DC currents in all three phases are thus not possible—may therefore also be regarded as a no-load test at a very low frequency and with a high magnetising current. The rotor is consequently rotating at the very low synchronous speed (no-load). The symmetric three-phase supply permits to generate comparably high and identical average losses in each phase.

The copper losses in the stator windings (1.06 pu), which are the only main loss source in the DC test, are determined using the measured current and the resistivity of copper at the average winding temperature. The losses are directly assigned to

the corresponding nodes in the analytic model and to the corresponding solids in the numerical model.

Analysis of test results and conclusions

The measured temperatures as well as the simulated values are tabulated in Table 3.2. Additionally, the temperature distributions in the slots and in the end windings in the numerical model are shown in Fig. 3.9.

Table 3.2: Measured and simulated temperatures during the DC test.

Part	**Temperature / °C**				
	Measured	Analytic model	Numerical model		
	(local)	(av.)	(av.)	(min.)	(max.)
Slot bottom	**75.7**	—	69.6	56.5	76.4
Slot top	**64.9**	—	69.2	62.6	75.5
Slot	—	**69.3**	**69.4**	56.5	76.4
End winding at NDE side	**63.6**	74.0	74.8	**66.3**	81.0
End winding at DE side	73.9	73.5	75.1	66.4	84.3

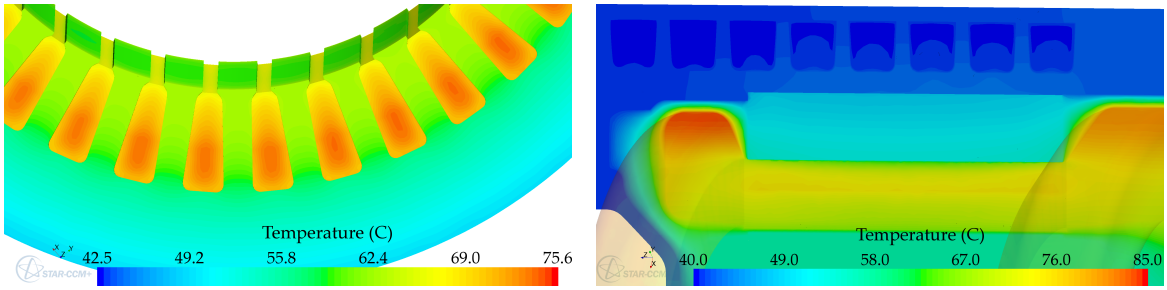

(a) Slots and stator back iron

(b) End windings

Figure 3.9: Simulated temperature in the slots and in the end windings during the DC test.

The calculated ratio of the measured losses to the calculated copper losses of 1.01 pu confirms that there is no significant mismatch between the experimental test and the simulation.

It may be seen that—without any parameter adjustments with respect to the default choices as given in Sec.3.5—the numerical and the analytic model give nearly

same average **slot** temperature (analytic: 69.3 °C, numerical: 69.4 °C). This temperature differs significantly from the measured temperatures at the slot bottom (75.7 °C) and at the slot top (64.9 °C), indicating that parameter adjustments may be indispensable at first sight.

If the measured local temperatures are, however, compared with the minimum and the maximum temperatures in the inner winding layer (slot top) and in the outer winding layer (slot bottom) of the numerical model, it may be seen that the measured temperatures lie within the temperature range of 20 °C which is present in the numerical model. Even though only a simplified slot model is used in the numerical analysis, similar temperature differences are also expected in the slots of the tested motor, based on the analyses in Sections 2.3.5 and 2.5.1 (Figs. 2.9 and 2.15) and depending on the actual positions of the sensors between the randomly placed wires.

Due to the good agreement between the numerical and the analytic model and due to the fact that the locally measured temperatures are within the expected range of the slot temperatures in the numerical model, the parameters are left unchanged in both models. The tested motor with the limited number of sensors and only approximate information on the sensor position does not allow for a more precise model adjustment. More sensors and a better knowledge about the exact placement of the sensor would allow for a more precise adjustment.

Large variations of the temperature may also be seen in the **end windings** in Table 3.2 and in Fig. 3.9(b), which also generally forbid to simply adjust the relevant parameters in order to achieve the best match between the measured local temperatures and e.g. the average temperatures in an analytic model.

Interestingly, the measured end winding temperature at the NDE side is significantly lower than the average temperatures in both models and even lower than the minimum temperature in the numerical model. Concluding also from the following experimental tests, the simplified envelope-based modelling of the end winding at the NDE side leads to a noticeable effect on the accuracy of the simulations (in particular during this extreme test with respect to the relevance of the winding losses on the resulting temperature distribution), with the measured temperature being 2.7 K below the minimum simulated temperature. A more accurate description of the end winding shape and modifications of the CAD model of the end winding at the NDE side, including also the coil connections, would be required in order to improve the accuracy.

3.6.2 Locked rotor test

Methodology

Comparably high losses are generated in the rotor during locked rotor tests and, generally, during tests at high slip rates. Such tests are therefore suitable to analyse the transfer of heat from the rotor and, with the measured temperatures and the computed losses, to adjust the thermal model resistances of the main flow paths.

An experimental test with a high slip rate is used in this case study to verify the default choices values of the thermal contact resistance between the shaft and the rotor stack, between the rotor stack and the rotor bars and the thermal resistances of the bearings. For easier referencing, the experimental test is referred to as locked rotor test in the following even though the rotor is, strictly speaking, not locked but rotating at a very low rotational speed.

The locked rotor test is carried out at $s = 99\,\%$, further details on the test parameters may be found in Table A.2 in the appendix.

In the numerical model, the iron losses in the stator and in the rotor are calculated using JMAG. The losses are then mirrored in order to allow for a mapping onto a full 2D model, the 2D loss distribution is extruded, exported and finally mapped onto the three-dimensional bodies in STAR-CCM+.

The induced losses in the rotor bars are also derived from the electromagnetic simulation. In order to investigate if the non-uniform loss distribution with the high local loss density at the bar tops has an effect on the temperature, the simulation is carried out with the mapped sources and, additionally, the results are briefly provided resulting from an analysis with an equivalent uniform loss density which gives the same total bar losses. If large temperature variations existed, this would, in turn, require adjustments of the conductivity in the EMAG model. The imported and the mapped iron losses in the stator and the rotor stack as well as the Joule losses in the rotor bars are shown in the two sub-figures (Figs. 3.10(a) and 3.10(b) respectively). The imported loss distribution in the rotor bars and the equivalent mapped uniform losses in the bars may also be seen in the figures.

The time series of the calculated Joule losses per end ring section (between two bars) is exported from JMAG, post-processed in MATLAB (calculation of the RMS value of the losses per end ring segment and calculation of the total end ring losses) and the determined end ring losses are used as uniform loss sources in the numerical model.

The Joule losses in the stator slots cannot be mapped directly as the computed slot losses in the 2D JMAG model also include the losses in the end winding (the entered winding scheme and the winding resistance are used in JMAG to calculate

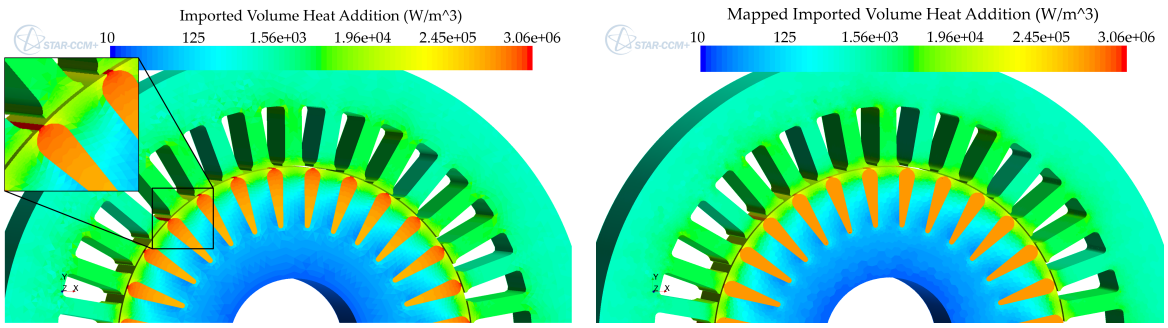

(a) Imported Joule and iron losses.

(b) Mapped Joule and iron losses with equivalent uniform bar losses.

Figure 3.10: Imported and mapped losses used for the numerical simulation of the locked rotor test (logarithmic scales)

the losses). Therefore, the Joule losses from JMAG are exported to MATLAB and the losses are split between the slots and the end windings based on the stack length and the coil length.

In the analytic model, the iron losses in the stator stack and in the rotor stack as well as the Joule losses in the stator and the rotor winding are calculated using the developed analytic modelling framework (Sec. 3.3) which also directly outputs the temperatures.

Analysis of test results and conclusions

The losses and the temperatures resulting from both models with the default parameters are provided in Table 3.3 (columns *Analytic* and *Numerical default*). The component losses are always related to the same, total measured losses during the test in order to allow for a direct comparison.

The numerical simulations with the mapped bar losses and with the spatially uniform loss density show practically no difference at all, the maximum effect on the rotor temperature does not exceed 0.1 K, the stator temperature is not affected at all. Consequently, the results from the study with uniform losses are not listed separately in Table 3.3. As can be seen in this table, the calculated losses of the analytic and the numerical model differ significantly, in particular the losses in the rotor bars. This difference consequently leads to different rotor temperatures.

In order to allow for a comparison of the thermal models, which is the primary target of this work, the numerical simulation is also carried out with the losses obtained from the analytic model in order to eliminate the effect of different losses in both models. The corresponding results are provided in the column *'Numerical mod.'* (modified).

Table 3.3: Losses and corresponding simulated and measured temperatures during the locked rotor test (component losses related to same total measured losses).

	Analytic	**Numerical** (default)	(mod.)	**Measured** (local)
Losses / total measured losses	%	%	%	—
Stator Joule losses	38.8	36.8	38.8	—
Rotor Joule losses	41.2	33.1	41.2	—
Stator iron losses	1.9	0.5	1.9	—
Rotor iron losses	2.6	0.3	2.6	—
Simulated/measured losses	0.85	0.71	0.85	—
Temperatures	°C	°C	°C	°C
Rotor end NDE side	**148.2**	139.0	**157.0**	156.2
Rotor end DE side	**148.2**	138.2	**156.1**	154.8
Stator slot	**80.9**	77.8	**80.1**	75.2 | 79.8
End winding NDE	**83.0**	81.2	**83.1**	78.2
End winding DE	**82.7**	81.6	**83.5**	79.8

The losses from the analytic model are chosen for the comparison of both models since the total losses in the analytic model are closer to the measured losses (85 %) than the numerical model (71 %). The remaining gap of 15 % between the losses from the analytic model and the measured losses may be regarded as still sufficient for an analytic model. Moreover, the gap is expected to be mostly due to increased frictional losses in the gear train (with respect to the originally measured gear losses which are used to calculate the gear losses) because of notable, increased noise levels of the gear train during operation. As most of the gear losses are directly dissipated by the cooling jacket and do not enter the electric machine, the gear losses are more relevant at higher rotational speeds and the influence is investigated in more detail in Sec. 3.6.3.

Contributing facts to the comparably big gap between the numerically determined and the measured losses are, amongst others, that (a) an ideal, purely sinusoidal current source models the supply and (b) a 2D model with a simple winding model and without skewing is used. Furthermore, the fact that calculated iron losses are significantly different in some teeth in Fig. 3.10 (even with completely different

solver settings the resulting distribution always resulted in an *irregular* loss distribution) and considering the numerical difficulties (convergence) due the very high local loss density in the bars indicate that the loss mismatch might be, at least partly, due to the used software.

In the analytic model, 1 % of the equivalent 50 Hz rated input are added in order to account for additional losses according to IEC standard 60349-3 [6] (Eq. (3.2)) which seems to match the total losses better.

Surprisingly, the numerically determined losses in the rotor are significantly lower than the losses that result from the analytic calculation. The difference between both models is mainly caused by the components of the additional load losses that are assigned to the rotor stack node and, in particular, to the rotor bars node in the analytic model. As a consequence, the numerical model in its current form likely fails to calculate all relevant additional loss phenomena in the rotor.

When using identical loss sources in both models, the simulated temperatures match rather well. The most significant difference is the calculated rotor temperature which is 8.4 K higher in the numerical model (+5.7 %).

Since the above mentioned thermal resistances (bearing and contact resistances in the rotor), which are to be verified with the locked rotor test, are modelled similarly in both models, the difference is caused by a different thermal resistance.

The comparison of both models shows that the temperature differences in the air gap between the stator and the rotor interface are 61 K in the analytic and 75 K in the numerical model. An increase of the thermal resistance of the air gap by 20 % in the analytic model leads to the temperatures in Table 3.4.

Table 3.4: Analytically calculated temperatures with adjusted air gap resistance (modified R_{th}) compared with original values from analytic and from modified numerical simulation.

Part	**Temperature / °C**		
	Analytic model (modified R_{th})	Analytic model (default)	Numerical model (modified losses)
Rotor end NDE	157.0	148.2	157.0
Rotor end DE	157.1	148.2	156.1
Stator slot	80.7	80.9	80.1
End winding NDE	82.9	83.0	83.1
End winding DE	82.6	82.7	83.5

With this updated choice, the relative difference between the rotor stack temperature in the numerical and the analytic model is now $-0.4\,\%$, while the other relative differences are in the range of $1\,\%$ or less.

Considering the fact that the updated rotor temperature also matches the measured temperature better (nearly identical), the used correlation (Eq. (3.45)) seems to underestimate the thermal resistance of the air gap, at least at low rotational speed. Even though adjustments of the thermal resistance of the air gap are expected to be required also at higher rotational speeds, it is not possible to draw the general conclusion that the thermal resistance is generally around $20\,\%$ off with respect to the correlation at all rotational speeds. The non-linearity alone already forbids to assume that the ratio is constant. A series of tests at different rotational speeds with a modified experimental set-up would be required (e.g. no connected gear set in order to avoid varying injected losses) in order to validate this assumption.

With the adjusted air gap resistance and with identical losses, there is a good agreement between both models. The comparison between the simulated temperatures and the measured temperatures is, however, complicated because of the mismatch between the analytically determined losses and the simulated values and neither value matching the measured losses. Additionally, the measured temperatures are only local temperatures and are not necessarily equal to the average temperature as shown in Table 3.9 by the measured temperature at the slot bottom and the comparison with the temperature range in the numerical model.

Concluding from the previous analysis, there is no clear indication from the locked rotor test that the contact resistances and the thermal resistances need to be adjusted. According to the analytic model, the end winding is warmer on the NDE side than on the DE side, whereas the numerical model and the measurements indicate that the end winding is generally slightly warmer on the DE side.

The review of the analytic model shows that a too high value had been chosen for the length of the conductive heat flow path from the end winding to the stator slot node on the NDE side. When the value (relevant axial coil length) is set to the value of the DE side, the end winding temperatures at the NDE and at the DE side are $82.7\,^{\circ}\mathrm{C}$ and $82.8\,^{\circ}\mathrm{C}$ respectively (difference of $-0.1\,\mathrm{K}$ compared with $+0.3\,\mathrm{K}$ prior to the adjustment and a difference of $-0.4\,\mathrm{K}$ in the modified numerical model). This adjustment of the analytic model is used in all following tests and furthermore leads to a correction of the DC test results with the end winding on the NDE now being colder than on the DE side with the correction (temperature reduction from $74.0\,^{\circ}\mathrm{C}$ in Table 3.2 to $73.3\,^{\circ}\mathrm{C}$) which is now consistent with the measurement and the numerical simulation.

The measurements and the numerical model also show that the rotor is slightly

warmer on the NDE side. The analytic model, which uses the simplification of one node per rotor side, i.e. there is no distinction between the end ring and the rotor stack side for convection and axial heat transfer is only modelled by the rotor bars, does not allow to reflect this comparably fine difference between both rotor sides.

Radiation

Radiation is generally neglected in the analytic model and also not analysed in the numerical model. Only minor radiative heat transfer is expected between the outer motor surface and the environment, due to the minor temperature differences.

The locked rotor test with its comparably high rotor temperature and the high temperature gradients is, however, used to get an understanding of what effect can be expected with respect to radiation in the inner of the electric machine. A numerical simulation is carried out using the numerical model with the modified loss input.

Radiation is modelled by a surface-to-surface radiation module (view factors are consequently calculated when enabling the radiation module), the air is modelled as non-participating medium and the bodies are modelled as grey bodies (Sec. 1.4.3).

The temperature distribution on a 2D cross-section in the inner of the electric machine is shown in Fig. 3.11 for both numerical studies, the numerical model without radiation (Fig. 3.11(a)) and with radiation (Fig. 3.11(b)). The temperatures of both simulations are, furthermore, tabulated in Table 3.5.

Table 3.5: Results of numerical simulation with and without radiation.

Part	**Temperature / °C**	
	With radiation	Without radiation
Rotor end NDE	155.5	157.0
Rotor end DE	154.5	156.1
Stator slot	80.0	80.1
End winding NDE	82.9	83.1
End winding DE	83.3	83.5

As expected, the inclusion of radiation in the numerical model leads to a slight reduction of the end winding temperatures (−0.2 K) and, more notably, of the rotor temperatures (−1.6 K at the DE side, −1.5 K at the NDE side). The locked rotor test is, at the same time, an extreme case with respect to radiative heat transfer from the rotor to the surrounding bodies. The temperature difference of 1.6 K may therefore

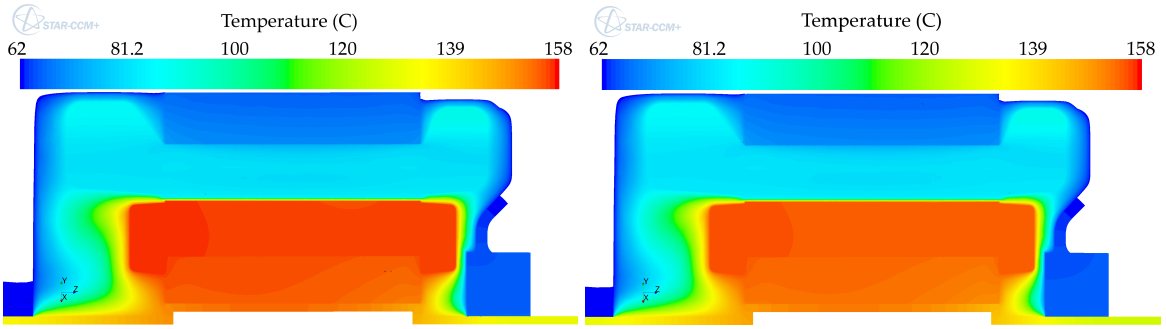

(a) Temperature distribution without radiation (b) Temperature distribution with radiation

Figure 3.11: Temperatures on cross-section during locked rotor test (a) without and (b) with radiation (clipped below 62 °C).

be regarded as the maximum effect on the rotor of the motor used for this case study, while radiation even hardly affects the temperatures in the stator.

3.6.3 Passive test

Methodology

The DC test and the locked rotor test are carried out at comparably very low rotational speeds. The mechanical losses of the bearings and the sealing rings, the windage losses as well as the losses in the gear train are typically negligible at low rotation speeds and thus during those tests.

At higher (typical) rotational speeds, these loss sources become more significant and may have to be considered in the thermal model.

A passive test—similar to the tests in Sec. 2.9—is carried out in order to check the significance of the mechanical losses and, in case of significant contributions, to allow for a verification of the modelling of the mechanical losses.

During the test, the induction motor under test is accelerated to twice the rated speed by the connected load motor. The parameters of the test and the measured temperatures are provided in Table A.3 in the appendix.

The mechanical losses in the bearings and in the sealing rings are calculated analytically with the formulas presented in Sec. 1.3.5, the gear losses are interpolated from a three-dimensional loss map (losses as function of torque, speed and temperature) which is based on experimental loss measurements. The determined gear losses are then modelled as loss injection into the motor housing and into the shaft at the DE side with 90 % of the losses being injected into the housing and 10 % into the shaft in both models. The bearing and bearing sealing losses are also modelled

as loss injections in both models.

Analysis of test results and conclusions

The stator heats up by approximately 2 K while the rotor temperatures increase by more than 10 K. The simulated temperatures are summarised in Table 3.6 and compared with the measured temperatures, the temperature distribution across the machine is illustrated in Fig. 3.12.

Table 3.6: Measured and simulated temperatures during the passive test.

Part	**Temperature / °C**		
	Analytic model	Numerical model	Measured
Rotor end NDE	59.2	58.5	61.6
Rotor end DE	59.3	62.0	65.1
Stator slot	51.6	51.6	50.2 | 50.8
End winding NDE	51.7	51.0	51.4
End winding DE	51.8	51.9	51.0

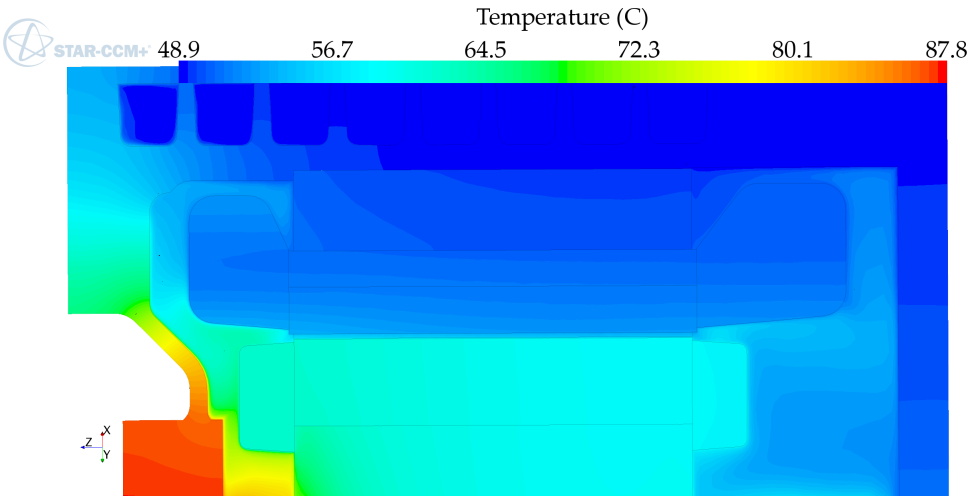

Figure 3.12: Temperature distribution during the passive test.

Similar to the locked rotor test, the analytic model only gives very similar temperatures at the rotor ends on both sides (0.1 K difference), while the numerical simulation and the measurement both show a difference of 3.5 K between both sides. As can be seen in Fig. 3.12, the heat injected on the DE side leads to high temperature gradients particularly in the rotor stack with its comparably low thermal conductivity in axial direction. The analytic model, which only models axial heat flow in axial

direction, is not able to resolve this temperature profile. A separation of the end ring surface and the stack end surface and an explicit modelling of axial heat flow in the rotor stack would be required.

At the same time, the high temperature gradients in the rotor stack indicate why the differences between the numerically simulated and the measured temperatures of the rotor but also of the stator are not necessarily caused by an incorrect simulation or incorrect measurements. The simulated 62 °C at the DE side and the 58.5 °C at the DE side (Table 3.6), for instance, are volumetric average temperatures in the rotor end regions which also include the end rings. The measured temperatures are 3.1 K higher. Considering that the temperature in the rotor stack reaches up to 70.1 °C and comparing the measured temperatures with the plotted temperatures in Fig. 3.12, it is possible and likely that the measured local temperatures match the simulated local temperature at the sensor position with a better accuracy than the 3.1 K.

Table 3.7 also lists the minimum, the maximum and the average temperatures from the numerical simulation and the comparison with the measured temperatures confirms that the measured rotor temperatures are within the ranges of the numerical simulation. Generally, it may be concluded that even the simplified modelling of the mechanical losses in the bearings and in the gear train leads to a model which still matches the measured temperatures with sufficient accuracy. The split factor 90/10 has also been verified at rated speed and is used in the following cases.

Table 3.7: Minimum, maximum and average simulated temperatures compared with measured temperatures during passive test.

Part	**Temperature / °C**			
	Measured	Numerical model		
	(local)	(av.)	(min.)	(max.)
Stator slot	50.2 | 50.8	51.6	50.3	54.1
Rotor stack	61.6 | 65.1	60.1	58.2	**70.1**
Rotor bars	—	59.0	58.5	**62.1**
End winding, NDE	51.4	51.0	50.3	52.9
End winding, DE	51.0	51.9	51.1	54.6

3.6.4 Stationary load case

Methodology

The stationary load case is a load case at nearly rated values and therefore serves to verify the thermal models at typical operating conditions. Similar to the passive test in Sec. 3.6.3, the mechanical losses (gear losses, bearing and sealing losses) are calculated analytically and are used in both models. Due to the symmetrical 3-phase current source in the JMAG model, the slot losses are identical in both models. The Joule losses in the end windings as well as in the end rings are taken from the analytic model since the end windings and the end rings are not modelled in the 2D JMAG model. Due to the comparably high rotor temperature and an only moderately hot stator winding, radiation is enabled in the numerical model.

Consequently, differences in the calculated losses between both models may be due to the numerically determined iron losses in the stator and the rotor as well as the bar losses which are calculated in JMAG and mapped onto the numerical 3D model. The additional losses which are calculated according to Sec. 3.3.4 in the analytic model may lead to further differences.

Analysis of test results and conclusions

Similar to the locked rotor test in Sec. 3.6.2, the losses used in both models and the resulting temperatures are summarised in Table 3.8 and compared with the measured temperatures. The component losses are again related to the same, total measured losses during the test.

The difference of the Joule losses in the stator is due to the additional losses that are partly added to the slot losses in the analytic model, whereas only the losses caused by the ideal, symmetrical current source are used in the numerical model. Also the iron losses are significantly higher in the analytic model due to additional factors accounting for degradation due to manufacturing and processing the electrical steel. The numerical model uses standard data from the material database which is based on Epstein frame tests. The Joule losses in the rotor of the analytic model are, by contrast, only 61 % of the losses in the numerical model.

The total losses in the analytic model are 89 % of the total measured losses, the losses in the numerical model are 90 % of the total measured losses. In the analytic model, the rotor losses are expected to be underestimated, while the Joule losses and the iron losses are expected to be underestimated in the numerical model. Additionally, the gear losses, which are identical in both models, are expected to be higher than the calculated gear losses (interpolated from experimentally determined loss

Table 3.8: Losses and corresponding simulated and measured temperatures during the stationary load case (component losses related to same total measured losses).

	Analytic	**Numerical**			**Measured**
Losses / total measured losses	%	%			—
Stator Joule losses	**30.3**	**28.6**			—
Rotor Joule losses	**13.7**	**22.4**			—
Stator iron losses	**18.4**	**11.9**			—
Rotor iron losses	1.8	2.2			—
Mechanical losses	24.7	24.7			—
Simulated/measured losses	**0.89**	**0.90**			—
Temperature / °C	(av.)	(av.)	(min.)	(max.)	(local)
Stator slot	78.3	80.3	64.0	89.6	74.4 | 83.8
Rotor stack	114.6 | 115.5	163.2	153.8	164.4	133.1 | 134.3
Rotor bars	115.7	164.2	163.3	164.8	—
End winding NDE	81.2	86.8	78.1	95.8	77.8
End winding DE	81.4	88.5	78.1	103.0	84.3

map, Sec. 3.6.2).

The numerical thermal model and the analytic thermal model show good agreements in the previous tests. However, the very significant difference between the rotor losses in the numerical and in the analytic model leads to differing rotor temperatures. In the analytic model, the rotor temperature is around 115 °C, while it is around 164 °C in the numerical model. The measured values are approximately 134 °C and, thus, lie between the values of the numerical and the analytic model.

Using the same losses in both models leads to comparable results, which confirms that the thermal models themselves are not incorrect. Instead, corrections of the analytic loss calculation routine and also an in-depth analysis why the rotor losses in the numerical are overestimated are required in order to obtain more accurate results. The fact that differing losses lead to significant deviations confirms the introductory remark in Chapter 1 that the analysis of the motor losses forms a vital and integral part of an overall thermal study. Accurately determined losses are consequently the prerequisite for accurately predicted temperatures by a thermal model.

In order to illustrate the sensitivity of the simulated temperatures with varying

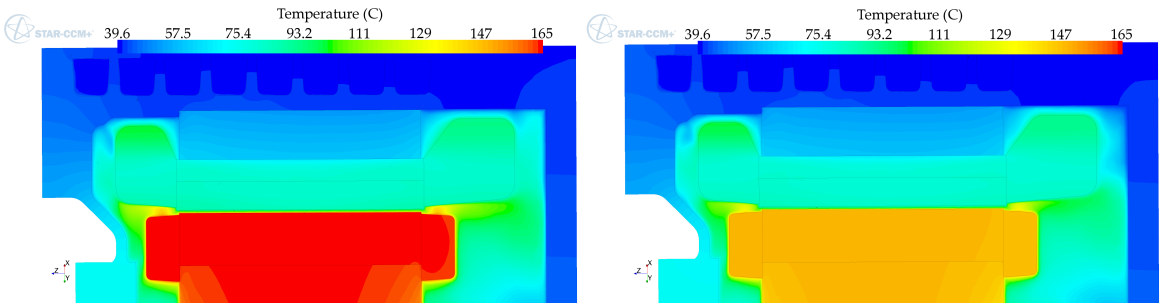

(a) Temperature distribution with default losses (b) Temperature distribution with modified losses

Figure 3.13: Temperatures on cross-section during stationary load case (a) with default losses and (b) with increased iron losses (+20 % related to default iron losses) and reduced losses in the rotor winding (−20 % related to default rotor Joule losses).

losses, the iron losses of the numerical model are increased by 20 % (roughly estimated increase due to manufacturing-related effects) and decrease of the rotor losses by 20 % (estimation). The resulting temperature distribution is compared with the base simulation (default losses) in Fig. 3.13 and in Table 3.9. With the simulated losses being only slightly lower than in the base case (88 % instead of 90 %), the average rotor temperature decreases by 16 K, the temperature of the stator winding decreases by just 1 K. This illustrates the particularly high sensitivity of the rotor temperature to the rotor losses.

It may also be noted that the lowest rotor temperatures are expected to be at the stack ends (Figs. 3.11 and 3.13), which is where the rotor temperatures are measured in this experimental set-up. Significant differences may therefore exist between the measured temperatures and the actual average and maximum rotor temperatures. Certain inaccuracies are introduced due to the fact that the measured rotor temperatures are assumed to be the average temperatures, which are then used to adjust the electric resistivity. The resistivity directly influences the simulated losses and the simulated temperatures.

3.6.5 Transient load case

Methodology

The transient analytic thermal model (Fig. 3.4) is verified by a transient load case. The calculated time series of the input losses (related to the total measured losses at $t = 0\,\text{min}$, the start of the transient load case) and the measured temperatures are provided in Figs. 3.14(a) and 3.14(b) (dashed lines) respectively. Separate graphs for

Table 3.9: Minimum, maximum and average simulated temperatures compared with measured temperatures during stationary load case.

Part	**Temperature / °C**						
	Measured	Default losses			Modified losses		
	(local)	(av.)	(min.)	(max.)	(av.)	(min.)	(max.)
Stator slot	74.4 | 83.8	**80.3**	64.0	89.6	**79.0**	63.5	86.5
Rotor stack	133.1 | 134.3	163.2	153.8	164.4	147.0	138.8	148.0
Rotor bars	—	**164.2**	163.3	164.8	**147.8**	146.8	148.4
End winding, NDE	77.8	86.8	78.1	95.8	85.9	77.4	94.4
End winding, DE	84.3	88.5	78.1	103.0	87.5	77.5	102.2

each load step and for both the rotor and the stator temperature are provided in the appendix (Sec. A.5).

The transient load case consists of a first step from stand-still to a stationary load point, resulting in temperature increases from the initial temperature of 40 °C (achieved by heating up the motor by the coolant in the cooling jacket) to the resulting steady state temperatures. The current is kept constant at the target value leading to an increase in the Joule losses as the stator winding heats up and the electrical resistivity of the copper increases.

Starting from the stationary load point, the stator current is then set to a constant and higher value at the same rotational speed in a second step. The resulting second transient heat-up of the DUT is carried out until the temperatures reach steady states again. During the complete test, the inlet temperature of the coolant is kept at constant 40 °C. The test is carried out at the same rotational speed, thus with practically constant mechanical losses, reducing the complexity of the test for an easier model verification.

Following the analysis of the stationary load case, in which the calculated Joule losses in the rotor are lower than the real rotor losses, the Joule losses in the rotor are increased by 30 % in the loss model. This modification targets at reducing the offset between the measured and the simulated temperatures, thus allowing for an easier comparison of the transient characteristics.

The transient analytic calculation routine reads the time series of the input parameters. Electromagnetic loss calculations are carried out at fixed time steps (every few seconds), the losses are then assumed constant in the time intervals and the transient thermal problem is then solved with the constant loss input.

Analysis of test results and conclusions

The calculated loss input in Fig. 3.14(a) shows drops in the losses in both the stator and the rotor winding at $t = 52\,\text{min}$, which are caused by problems with the control of the DUT. Interestingly, the short period of slightly reduced losses leads to a noticeable decrease in the simulated temperature (solid lines in Fig. 3.14(b)). This drop is, however, not visible in the measured temperatures (dashed lines in Fig. 3.14(b)), most likely because the expected only very slight effect is overshadowed by the existing ripples (noise) in the recorded signals.

More significant loss oscillations exist during the transition between the two load points and they are also related to problems with the control of the DUT. While such oscillations are generally undesirable during machine operation, the comparison of the oscillating input with the simulated and the measured temperatures actually allows to study how the fast variations of the electromagnetic (loss) input are reflected in the temperature responses.

Generally (and similar to the stationary load cases), the simulated temperatures in the rotor are still lower than the measured temperatures, despite the increase of the rotor losses by 30 %. Moreover, the sum of the calculated losses is still significantly lower than the total measured losses. When the losses increase during the test ($t > 100\,\text{min}$), the offset between the simulated and the measured rotor temperatures decreases and the loss model seems to match better during the second part of the transient load case (see also Figs. A.1 and A.2 in Sec. A.5 in the appendix). The stationary and the transient thermal model are practically identical, with the exception of the additional connected thermal capacitances. The permanent offset between the measured and the simulated rotor measurements is therefore expected to be also caused by inaccuracies of the loss models.

Irrespective of the expected differences in the rotor, the simulated temperatures in the stator as well as the simulated transient behaviour show a good agreement with the measurements. Slight differences exist around $t = 0\,\text{min}$ because of the different initial conditions between the actual machine, in which slight temperature differences exist, whereas all temperatures are set to the coolant inlet temperature at $t = 0\,\text{min}$ in the analytic model (see also Fig. A.1 in the appendix).

Additionally, it may be seen clearly that the thermal time constant of the rotor is larger than the time constant of the stator as it requires more time for the rotor to reach its thermal steady state. This result also illustrates that the values of the thermal capacitances of the machine parts as such do not directly reflect the actual behaviour of the machine assembly. In fact, the calculated thermal capacitance of the stator is larger than the thermal capacitance of the rotor. The thermal behaviour

is, however, influenced by how the components are connected to each other, the rotor being connected to the heat sink and the other components by heat flow paths with comparably high thermal resistances.

Furthermore, the increase of the electrical resistivity of the copper is shown implicitly by the plotted losses in the stator winding ($0\,\text{min} < t < 20\,\text{min}$) in Fig. 3.14(b). While the stator current is constant, the rising temperature in the stator winding (Fig. 3.14(a)) causes the resistivity and thus the Joule losses to increase.

The transient oscillations of the losses may be said to be evened out nearly completely due to the larger time constants of the thermal system. Slight temperature drops of the slot and the end winding temperature are visible in the simulation (solid lines) and also very slight drops may be seen in the logged temperatures but with the added signal noise making a clear identification of the extent of the temperature drops more difficult.

A further observation may be made concerning the ripple (noise) of the recorded temperatures. Especially the signals of the sensors in the stator slots and in the end winding on the DE side show higher noise levels than the the sensors in the end winding on the NDE side and in the rotor. As the sensors in the stator slot and in the end winding on the DE side are guided through the slots from the NDE side to approximately the centre of the motor (slot sensors) and the end winding (DE sensor), the electromagnetic fields may influence the measurements.

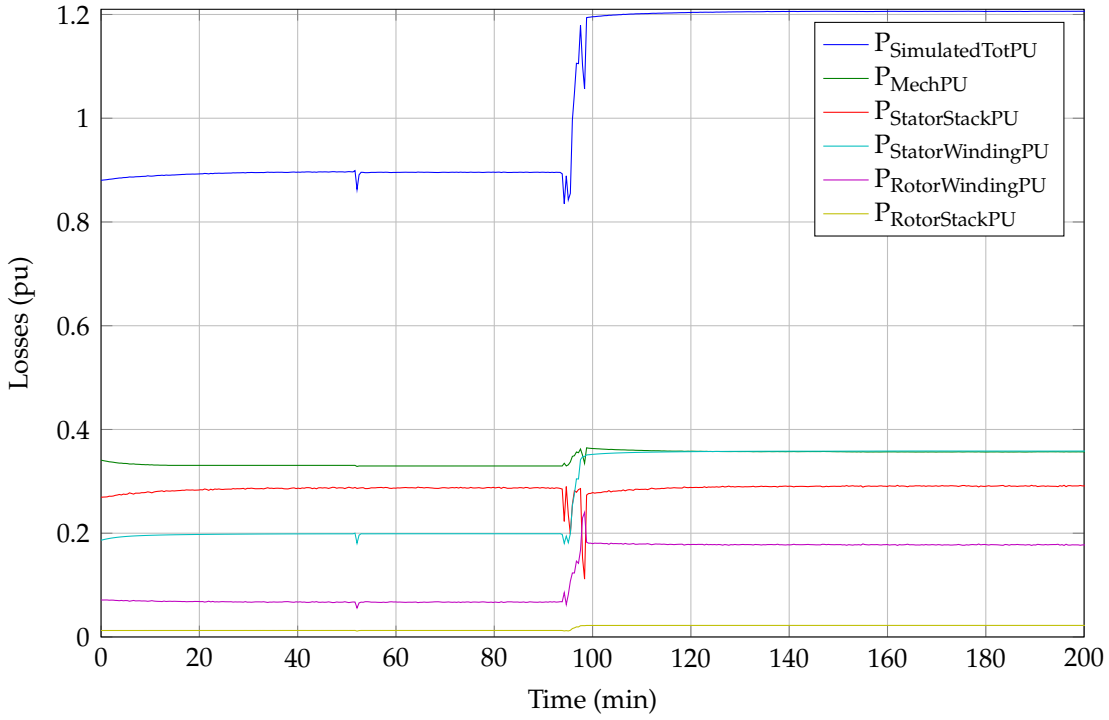

(a) Losses related to the total measured losses at the begin of the transient load case ($t = 0$ min).

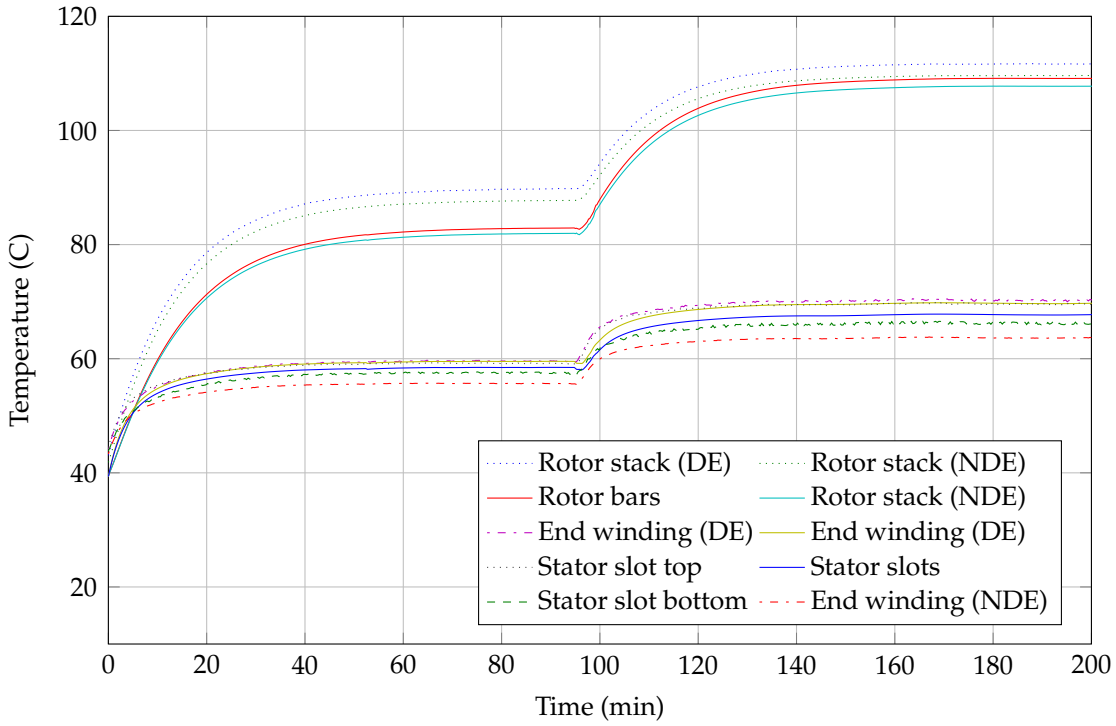

(b) Measured temperatures (dashed lines) and simulated temperatures (solid lines) during transient load case.

Figure 3.14: Loss input and comparison of measured and simulated temperatures during transient load case.

3.7 Review and conclusions

3.7.1 Case study

The primary target of the comparative case study is not to develop models whose output temperatures match the experimental results best but rather to use the results to understand possible limitations and how the different results can be combined in order to gain a better understanding of the thermal behaviour. The limitations of the DUT alone with its limited number of sensors, the not exactly defined sensor positions and the added complexity due to the connected gear train only allow for a study with limited accuracy.

The key conclusions may be summarised as follows:

- The temperature is generally not constant within the different parts, e.g. the end windings, the stator slots, the stator and the rotor stack. Consequently, additional information on the temperature distribution should be used when comparing measured local temperatures with the determined (average) temperatures from an analytic model. In this case study, the results of the numerical simulation are used to determine the expected temperature ranges in the regions, which are then compared with the measured and the analytically determined temperatures. Therefore, the combinations of both modelling approaches and the comparison with the measured temperatures permit to interpret the results adequately.
- If the sensor positions are known more precisely, it is possible to narrow down the expected temperatures at the sensor positions, in contrast to considering all temperatures in the complete region as possible temperatures. The uncertainty concerning the exact sensor positions in this case study leads to significant uncertainties and does not allow for a better parameter adjustment, for instance during the DC test. To give one example, the parameters modelling the convective heat transfer in the end winding regions cannot be adjusted adequately as the parameter adjustments only lead to variations well within the predicted temperature ranges.
- The rotor losses, which may only represent a few percent of the overall losses, have a very significant influence on the rotor temperature. Accurate loss calculations are generally indispensable for more accurate temperature predictions. Special experimental tests (DC tests, locked rotor and no-load tests) may support a more targeted verification of the loss models and the thermal models because of fewer relevant loss sources and heat flow paths.
- The numerical and the analytic model generally show similar results when

the same loss input is used. The analytic model fails, however, to model the unsymmetrical temperature distribution in the rotor stack. As may be seen from the numerical results, the temperature variations in the rotor bars and in end rings are comparably small (around 1 K in the stationary load case). The differences in the rotor stack are, by contrast, far more significant, reaching around 10 K in the stationary load case. The axial heat transfer in the rotor bars and in the rotor stack would need to be separated in the analytic model in order to resolve the temperature distribution in the rotor more accurately.

- The gear train is directly attached to the DE side of the machine and causes the rotor and also the housing to heat up on the DE side at higher rotational speeds (Tables A.3 and A.4, Fig. 3.12). The fact that only the temperature of the oil in the oil reservoir is measured does not allow for a verification of the temperature at the interface between the gear set and the cooling jacket. In the case study, the modelling of the gear losses is verified by comparing the measured and the simulated temperatures during the passive test. It would, nonetheless, be desirable to verify the temperature of around 88 °C at the interface in Fig. 3.12 in order to confirm the validity of the loss modelling.
- Based on the available test results from the transient load case, the transient analytic model seems to model the transient behaviour with sufficient accuracy. As in the case of the stationary experimental tests, inaccuracies of the loss calculation cause deviations between the measured and the simulated rotor temperatures.

3.7.2 Experimental test procedure

The experimental tests typically take more than one hour until the temperatures reach their steady states. The ambient conditions should ideally remain constant during the complete test duration.

During demanding load cases with high heat dissipation, the cooling system with the fan-cooled heat sink is operating at its limits. Therefore, changes of the ambient conditions such as a gradual increase of the ambient air or also sudden temperature decreases due to opened windows or doors affect the coolant temperature, which directly influences the temperatures inside the electric machine. Consequently, special care concerning opening windows or doors is required when carrying out the tests.

Furthermore, the temperature control unit is not able to keep the inlet temperature precisely at the pre-set value in case of significant changes of the generated losses (Fig. 3.15). As may be seen in Fig. 3.15(a), not only the rotor and stator tem-

peratures rise (starting from $t = 1122\,\text{min}$) but also the inlet temperature increases slightly ($1122\,\text{min} < t < 1134\,\text{min}$). At the same time, the temperature difference increases (Fig. 3.15(b)) and thus the dissipated heat since the dissipated heat is directly proportional because of the constant mass flow rate of the coolant.

Consequently, the heat is not transferred quickly enough from the coolant to the ambient air by the fan-cooled heat sink. Additionally, the transient behaviour of the temperature control unit leads to oscillations and a cooling down of the coolant below the set inlet temperature with a resulting permanent overcompensation (offset). The varying coolant temperature directly influences the winding temperature (with a slight delay).

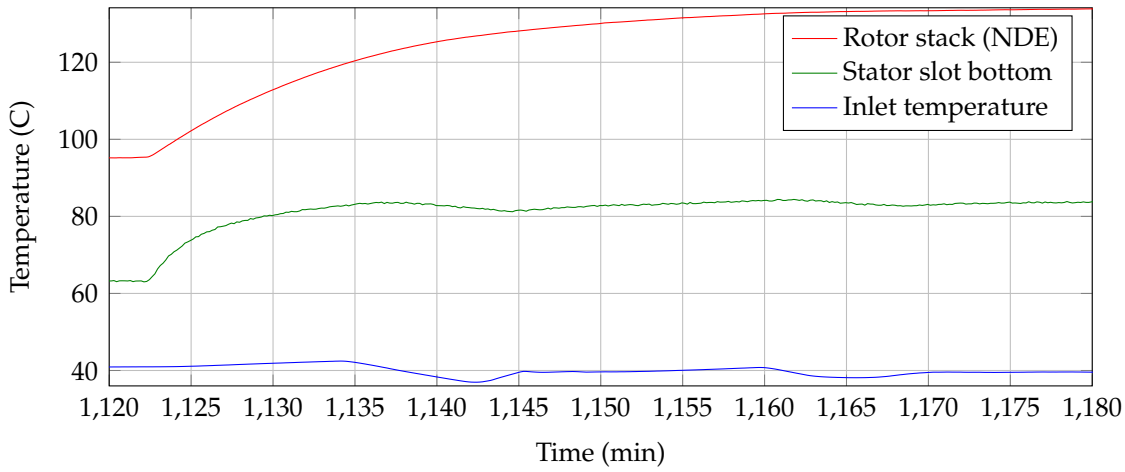

(a) Measured temperatures

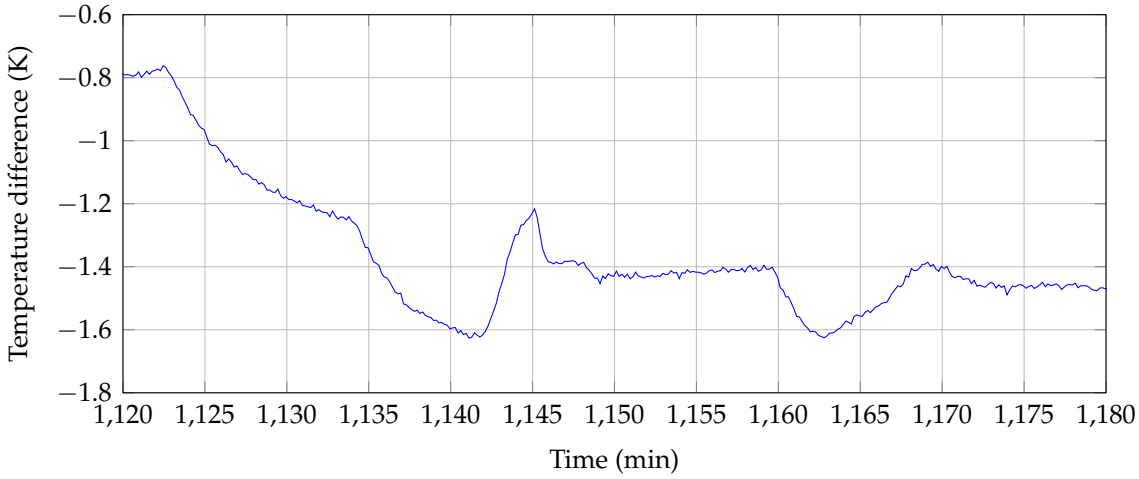

(b) Difference between inlet and outlet temperature

Figure 3.15: Oscillations after sudden loss increase.

In addition to stability problems with respect to the cooling circuit, also the controls of the DUT and the load machine sometimes cause stability problems, for in-

stance during the transient load case (Sec. 3.6.5). In case of stability problems or even shut-downs of the control during the stationary test, the experimental test is continued for a longer time under stable conditions until the thermal steady state is achieved.

Nonetheless, a transient load with stability problems during the transition between different load points is chosen for the analysis of the analytic model. The comparably simple overall transition from one load point to a second load point at the same rotational speed allows for an easier verification. At the same time, the short oscillations during the transitions due to the stability issues allow for an investigation of fast changes. Adjustments of the controllers and modifications of the cooling circuit are, of course, indispensable in order to investigate more complex load patterns in future tests.

3.7.3 Numerical modelling procedure

Model overview

The limited CAD format capabilities of the used tools (JMAG, STAR-CCM+, Creo) lead to a complex workflow with respect to the CAD model creation and the model and loss exchange (import and export) between the software tools.

The transient EMAG simulation in JMAG uses a $\frac{1}{4}$ 2D CAD model of the stator and the rotor. (3D simulations require significantly higher computational effort with only limited additional information e.g. concerning the iron loss calculation. Preliminary 3D simulations with a coarse mesh required 2 weeks of computation time but the results indicated that a finer mesh and more time steps would even be required.) The comparably simple 2D geometry is directly generated by the built-in CAD modeller of JMAG in order to reduce compatibility issues when importing a geometry into the FEM software.

The thermal simulation in STAR-CCM+, however, requires a 3D model of the complete machine. At the same time, developing and building a complete CAD assembly, also including the motor housing, is neither possible in STAR-CCM+ nor in JMAG. Therefore, the CAD tool Creo is used to create and modify the component models and to build the complete assembly.

Furthermore, in order to allow for a loss mapping without complex coordinate transformations, the coordinates of the JMAG geometry and the coordinates of the model in STAR-CCM+ need to be identical. Therefore, a full extruded stator and rotor CAD model is built in JMAG (directly based on the 2D model) and imported into Creo.

The additional component models (shaft, end rings, end windings, cooling jacket)

are built and assembled in Creo. The resulting 3D assembly is eventually imported into the CAD modeller of STAR-CCM+, where further processing is required in order to be able to define all interfaces (between contacting bodies) correctly.

Generating the meshed representation of the 2D geometry in JMAG succeeds with just slight adjustments of the default settings in JMAG. The (conformal) meshing of the complete 3D model in STAR-CCM+ is, by contrast, significantly more complex and time-consuming. Generally, a finer mesh is required in the air gap in order to adequately resolve the fluid flow in the very thin air gap. Therefore, thin layered elements are chosen for the air gap, which are grown from the surrounding solids.

The calculated losses in JMAG are exported to a NASTRAN file. More specifically, the triangular grid with the associated loss values is mirrored and extruded and finally exported. In order to allow for a mapping of the losses onto the model in STAR-CCM+, (i) the grid needs to be imported from the NASTRAN file and bodies (regions) are generated automatically, (ii) the losses need to be imported in a second step, and (iii) data mapper need to be defined which map the losses onto the model in STAR-CCM+ (from extruded triangular mesh to polyhedral mesh).

Conclusions

A complex set-up is required to allow for a mapping of the losses from the used FEM software onto a CFD model. The case study, however, clearly shows that coupling two complex tools, which model complex physical phenomena, requires not only attention to the coupling itself. The simulations of both tools need to be set-up and also interpreted correctly.

Most importantly, the simulated losses in JMAG—which are the direct input for the CFD simulation and therefore directly influence the results of the CFD analysis—do not consider certain losses and loss contributions because of the definition of the simulation (purely sinusoidal supply, iron losses according to data sheet, reduced 2D model). The calculated losses differ significantly from the measured losses and an in-depth analysis of the reasons and, based on the results, refined simulations need to be carried out.

The software tools and also the illustrated coupling generally provide additional means to gain a deeper understanding of the thermal behaviour but they do require (i) a profound understanding of the electromagnetic behaviour of electric machines and of the related loss phenomena, (ii) an understanding of the relevant heat transfer phenomena and, additionally, (iii) experience with the employed software tools.

3.7.4 Analytic modelling procedure

The analytic modelling framework comprises an electromagnetic model of the induction machine—extended by a loss calculation routine—and a thermal model which is coupled to the electromagnetic model. The developed modelling framework allows to carry out stationary simulations within fractions of seconds and transient simulations in several minutes, with the potential to reduce the computation time further by code optimisations.

Similar to the numerical modelling framework, the main shortcoming of the exemplary analytic model in the presented case study is the loss calculation routine, which does not provide the motor losses with the accuracy required to simulate the rotor temperatures, in particular, with sufficient accuracy. Improvements may be achieved by carrying out benchmarks with commercial analytic software and by verification with FEM simulations.

More importantly, the comparative case study illustrates that particular attention is required when building and adjusting an analytic thermal model only with local measurements or without any available measurements for verification purposes at all.

Not only introduce the complex loss phenomena significant challenges with respect to the input of the thermal models. Even with correctly determined losses, certain parameters of the thermal model should be verified and adjusted, if required.

Without any available experimental data, adjustments are not possible, leading to potential inaccuracies. Yet, even if experimental data is available, adjustments need to be carried out carefully as illustrated by the case study. The measured local temperature might be different to e.g. a predicted average temperature. A best-fit target for the simulated temperatures might therefore even be incorrect. More specifically, without detailed experimental data (for instance from several thermal sensors) or without additional results from numerical simulations, it may not even be possible to identify the target values of the simulations.

To give an example, the numerical simulation of the DC test (Sec. 3.6.1) reveals the expected high temperature ranges in the slots and the end windings. Relying on just one local measurement and one value from the analytic model, it may be difficult to judge how well simulated and measured values fit together.

Chapter 4

Conclusions and further research

4.1 General conclusions

The analysis of the component modelling in Chapter 2 and the machine modelling in the frame of the case study in Chapter 3 confirm that **there is no generally superior modelling approach**. Instead, the optimum model, which suits the problem that is to be investigated best, depends on the problem itself and on the desired output of the simulation (e.g. spatial resolution, stationary or transient output, possible constraints with respect to computational time).

To give an example, the analytic and the numerical air gap models in Sec. 2.5 give similar resulting thermal resistances for the air gap. While the numerical model, which requires significant more effort to be developed and run, allows to study the spatial temperature and velocity distributions within the air gap (Figs. 2.17 and 2.18), the analytic model provides the same thermal resistance (maximum relative deviation of $\pm 10\,\%$) almost instantaneously, using a correlation that is available in the literature.

Moreover, it has been shown that **an adequate loss modelling is indispensable**. This, at the same time, makes the thermal analysis rather complex. The case study clearly illustrates that a standard, simplified (analytic as well as numerical) loss modelling does not necessarily provide the required accuracy but more complex and sophisticated loss models may be required instead. In the case study, neither the analytic model nor the numerical model provide the rotor temperatures with sufficient accuracy.

Due to the complexity of both, the loss modelling and the modelling of the heat transfer in electric machines, **it is generally advisable to ensure that studies in the field of thermal modelling are validated adequately**.

For instance, if the analytic models presented in Chapter 2 were used in an analytic modelling framework similar to the one in Chapter 3 and if the presented

analytic loss modelling was employed in order to predict the temperatures of the induction machine in Chapter 3, significant inaccuracies would exist.

The available measurements show that the temperatures are significantly underestimated and the developed numerical model and the analysis of the special experimental tests allow to identify inaccurately determined rotor losses and not a problem with the analytic thermal model to be the root-cause.

Only with the three different elements, (i) the analytic model, (ii) the numerical model, and (iii) the measurements, it is possible to really understand and interpret the results adequately.

The deviation between locally measured temperatures and simulated temperatures is not necessarily the correct criterion for judging the accuracy of a thermal model: The numerical model, for example, reveals that comparably high temperature differences may be expected in the end windings, the slots and even in the rotor stack during the standard stationary load case (Sec. 3.6.4). Depending on where the thermal sensors are located, these local measurements are obviously not identical to averaged temperatures in an analytic model. Identical values may even indicate that the results do not match.

4.2 Future work

Chapter 2 provides a comprehensive overview of the thermal modelling of the key components and, at the same time, in-depth analyses of certain components, such as the stator slots and the air gap. Due to the inherent complexity associated with each single component, even the detailed analyses in this work may be regarded as first steps, which may serve as a basis for further research. Also the developed rather complex modelling frameworks in Chapter 3 may be extended or modified in order to improve their accuracy.

In the following, some areas for future research are suggested based on the models derived in Chapters 2 and 3:

I. Slot modelling (Chapter 2)

(a) *Wires coupled to a circuit simulation*
Uniform average copper losses are assumed and modelled in the wires of the detailed slot model in Sec. 2.3. In electric machinery, the loss phenomena are, however, more complex and the averaged losses are not expected to be perfectly uniformly distributed.
The **detailed numerical slot model** may be coupled to an electromagnetic

FEM tool which correctly models the current flow through the different wires and coils in the slot (treating the slot model as a part of the complete winding model) and which potentially simulates the losses in the winding more accurately. A bi-directional coupling would then also allow to study how a rising temperature affects the electric resistivity and, in turn, the copper losses, which affect the temperature.

Depending on the outcome of such a simulation (the effect on the temperature may be negligible), it may be investigated how a non-uniform loss distribution may be considered in a **simplified numerical** and in an **analytic model**.

(b) *Coupled slot models with mapped iron losses*

A detailed slot model, which is coupled to an electromagnetic model or tool, would also allow to use realistic, simulated iron loss distributions in the **numerical model**. Such a loss study might also consider potential degradation at the edges of the electrical steel sheet, introduced during the manufacturing of the lamination stack. Significant progress is made in this field and, for instance, the most recent release of JMAG (the FEM software employed in this work) now allows to model this effect explicitly.

The **analytic modelling** of the iron losses may then be developed accordingly and it may investigated if one or two point loss sources (total iron losses and separated loss sources for losses in the teeth and in the back iron, respectively) are sufficient or whether more complex iron loss modelling is required in the analytic model.

(c) *The local effects of a non-ideal impregnation*

All models assume an ideal impregnation or consider the effect of air pockets by reducing the effective thermal conductivity. Alternatively, the effect may be modelled by adding a certain contact resistance between the slot and the stack.

The **detailed numerical model** may be used to study how local imperfections of the impregnation affect the local temperatures by explicitly modelling imperfections of the impregnation. Experimental data is, however, required in order to model local imperfections accurately. Such a model may, however, be very specific to a certain machine manufactured in a specific way and the applicability to other machine designs needs to be verified.

II. Detailed validation of the transient lumped parameter modelling

In analytic thermal models, typically one thermal capacitance is used for each

main component, even though significant temperature differences may exist within those bodies. Transient numerical machine models may be used to investigate the effect of using just one or several thermal capacitances for the transient modelling in analytic models and how effects the overall thermal behaviour of the analytic models.

III. Detailed end winding modelling (Chapters 2 and 3)

The end windings of electric machines with random-wound windings are typically modelled by envelope-like representations in **numerical models**, i.e. the outer envelopes define the outer dimensions. The same approach is used in this work because the explicit modelling of all wires proved to be challenging. In order to ensure that the assembly can finally be meshed and simulated, a perfectly accurate modelling (no crossing lines or touching faces) is required.

Further research is therefore proposed with respect to a more detailed end winding modelling of random wound windings, which include the individual wires, the wire insulation in the end winding region and the impregnation (ideally also considering local imperfections). Such a more detailed end winding simulation would allow to validate simplified numerical and analytic models.

Appendix A

Experimental tests

A.1 DC test

Table A.1: Parameters of the DC test and measured temperatures.

Key parameters	**Value**	**Unit**
I_1 (measured phase current)	1.14	pu
f_1 (measured stator frequency)	0.01	pu
$\dot{m}$ (measured coolant mass flow rate)	1	pu
Joule losses (calculated)	1.06	pu
Calculated losses / measured losses	101	%
Measured local temperature (at sensor position)		
TC 1 (stator slot, bottom)	75.7	°C
TC 2 (stator slot, top)	64.9	°C
TC 3 (end winding, NDE)	63.6	°C
TC 4 (end winding, DE)	73.9	°C
TC 5 (rotor, NDE)	51.5	°C
TC 6 (rotor, DE)	51.3	°C
TC 7 (gear train (oil reservoir))	38.8	°C
RTD 1 (coolant, inlet)	40.3	°C
RTD 2 (coolant, outlet)	40.7	°C

A.2 Locked rotor test

Table A.2: Parameters of the locked rotor test and measured temperatures.

Key parameters (measured)	**Value**	**Unit**
I_1 (phase current, RMS)	0.72	pu
f_1 (stator frequency)	1	pu
V_1 (line voltage, RMS)	0.19	pu
M (output torque)	0.04	pu
s (slip)	99	%
$\dot{m}$ (coolant mass flow rate)	0.97	pu
Local temperatures (measured at sensor positions)		
TC 1 (stator slot, bottom)	75.2	°C
TC 2 (stator slot, top)	79.8	°C
TC 3 (end winding, NDE)	78.2	°C
TC 4 (end winding, DE)	79.8	°C
TC 5 (rotor, NDE)	156.2	°C
TC 6 (rotor, DE)	154.8	°C
TC 7 (gear train (oil reservoir))	54.8	°C
RTD 1 (coolant, inlet)	58.9	°C
RTD 2 (coolant, outlet)	59.2	°C

A.3 Passive test

Table A.3: Parameters of the passive test and measured temperatures.

Key parameters	**Value**	**Unit**
Gear losses (interpolated from measured loss map)	1.79	pu
Bearing + sealing losses NDE side (calculated)	2.91	pu
Bearing + sealing losses DE side (calculated)	2.91	pu
$\dot{m}$ (measured coolant mass flow rate)	1.18	pu
n (rotor speed)	2	pu
Local temperatures (measured at sensor positions)		
TC 1 (stator slot, bottom)	50.8	°C
TC 2 (stator slot, top)	50.2	°C
TC 3 (end winding, NDE)	51.4	°C
TC 4 (end winding, DE)	51.0	°C
TC 5 (rotor, NDE)	61.6	°C
TC 6 (rotor, DE)	65.1	°C
TC 7 (gear train (oil reservoir))	51.4	°C
RTD 1 (coolant, inlet)	48.8	°C
RTD 2 (coolant, outlet)	48.9	°C

A.4 Stationary load case

Table A.4: Parameters of stationary load case and measured temperatures.

Parameter	Value	Unit
I_1 (phase current)	0.99	pu
f_1 (stator frequency)	1.02	pu
M (output torque)	0.99	pu
s (slip)	2.32	%
$\dot{m}$ (coolant mass flow rate)	0.96	pu
Measured local temperature (at sensor position)		
TC 1 (stator slot, bottom)	74.4	°C
TC 2 (stator slot, top)	83.8	°C
TC 3 (end winding, NDE)	77.8	°C
TC 4 (end winding, DE)	84.3	°C
TC 5 (rotor, NDE)	133.1	°C
TC 6 (rotor, DE)	134.3	°C
TC 7 (gear train (oil reservoir))	54.7	°C
RTD 1 (coolant, inlet)	39.5	°C
RTD 2 (coolant, outlet)	41.0	°C

A.5 Transient load case

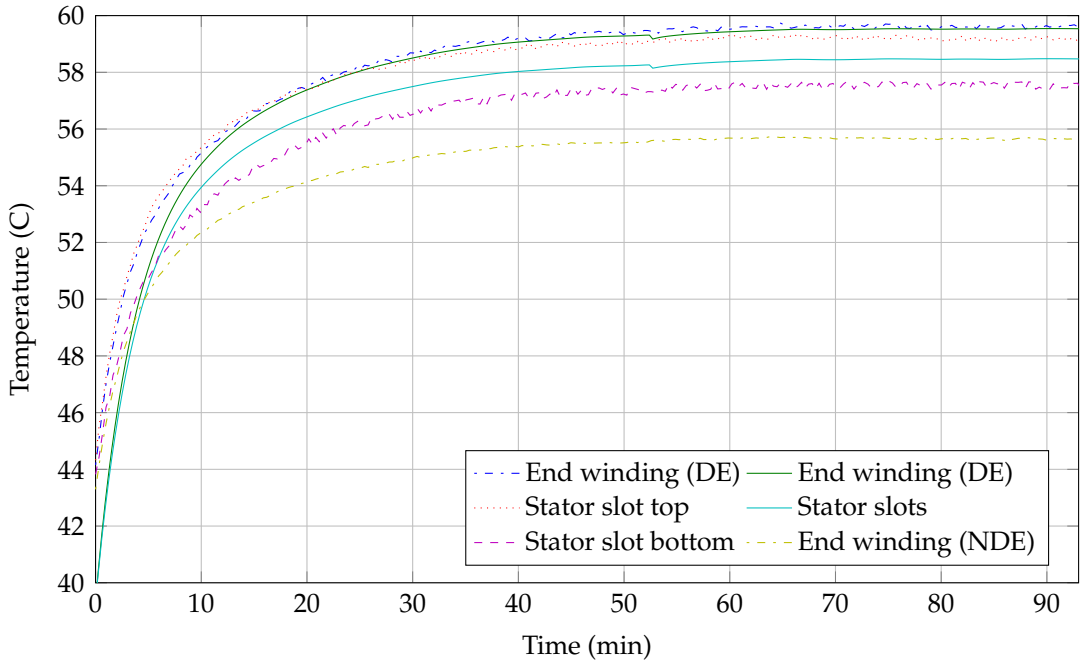

(a) Stator temperatures

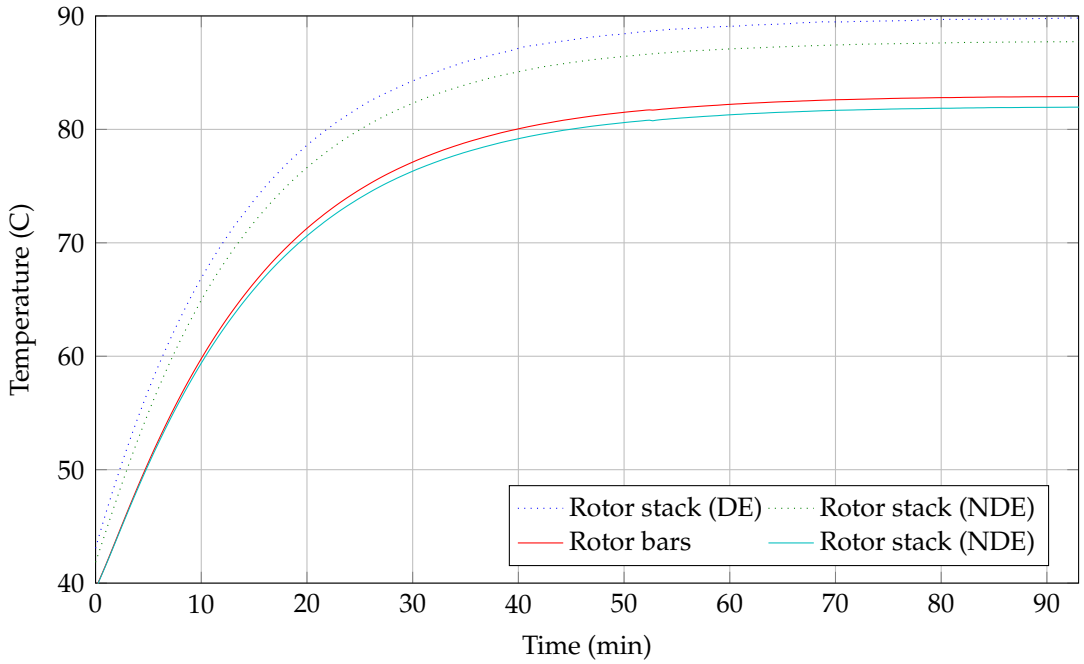

(b) Rotor temperatures

Figure A.1: Measured temperatures (dashed lines) & simulated temperatures (solid lines) during the first part of the transient load case.

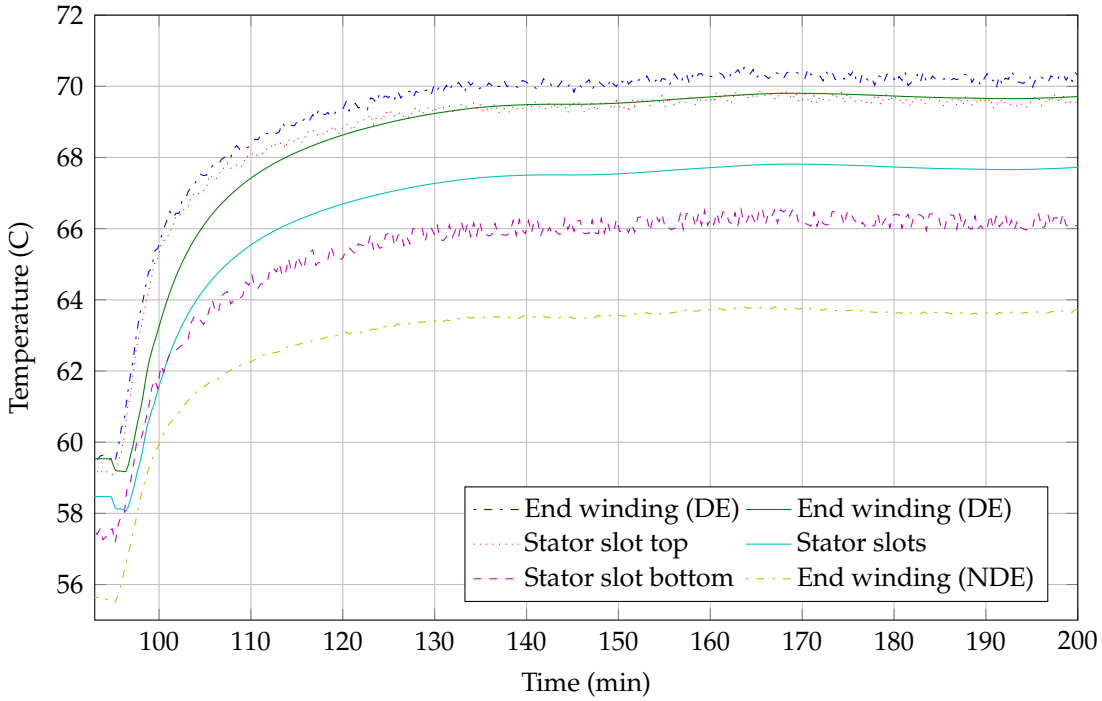

(a) Stator temperatures

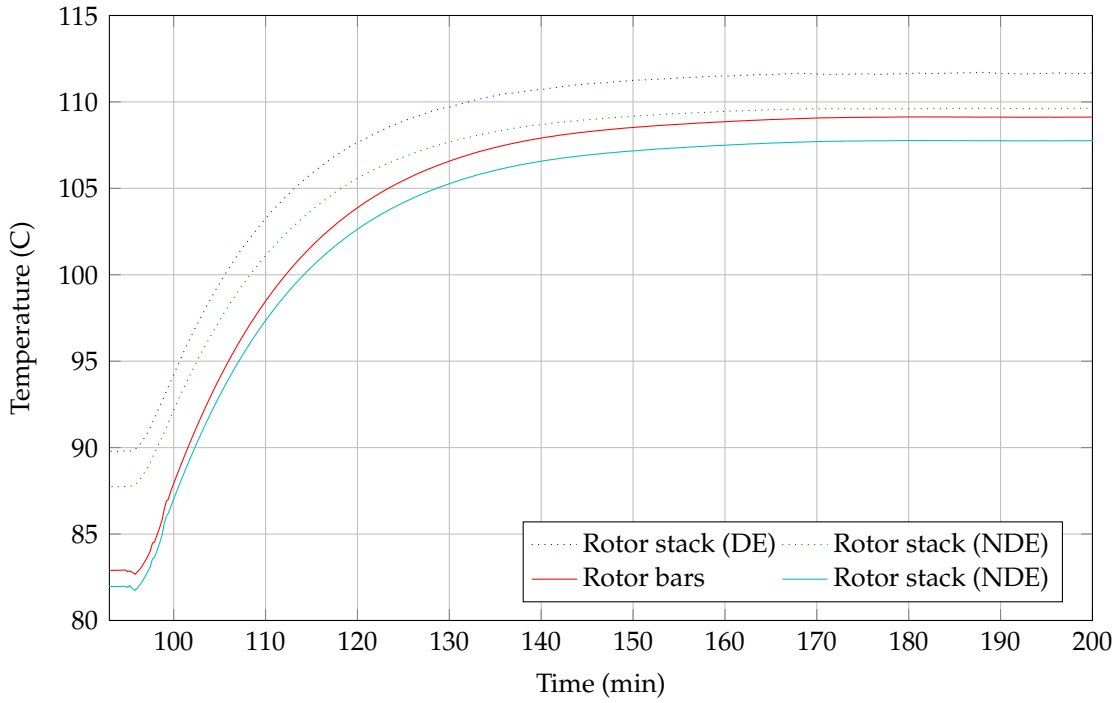

(b) Rotor temperatures

Figure A.2: Measured temperatures (dashed lines) & simulated temperatures (solid lines) during the second part of the transient load case.

Bibliography

[1] C. R. Soderberg, "Steady flow of heat in large turbine-generators," *Transactions of the American Institute of Electrical Engineers*, vol. 50, no. 2, pp. 782–798, 1931.

[2] Österreichischer Verband für Elektrotechnik, *ÖVE EN 60034-6: Umlaufende elektrische Maschinen – Teil 6: Einteilung der Kühlmethoden (IC-Code)*. Eigenverlag des Österreichischen Verbandes für Elektrotechnik, Wien, 1993.

[3] T. A. Lipo, *Introduction to AC machine design*. Wisconsin: Wisconsin Power Electronics Research Center, 3rd ed., 2011.

[4] A. Schoppa, J. Schneider, and C.-D. Wuppermann, "Influence of the manufacturing process on the magnetic properties of non-oriented electric steels," *Journal of Magnetism and Magnetic Materials*, vol. 215–216, pp. 74–78, 2000.

[5] A. Boglietti, A. Cavagnino, L. Ferraris, and M. Lazzari, "The annealing influence onto the magnetic and energetic properties in soft magnetic material after punching process," in *IEEE International Electric Machines and Drives Conference 2003 (IEMDC'03)*, vol. 1, pp. 503–508 vol.1, 2003.

[6] International Electrotechnical Commission, *IEC/TS 60349-3: Electric traction – Rotating electrical machines for rail and road vehicles – Part 3: Determination of the total losses of converter-fed alternating current motors by summation of the component losses*. IEC, Geneva, 2010.

[7] J. Pyrhönen, T. Jokinen, and V. Hrabovcová, *Design of rotating electrical machines*. Chichester: John Wiley & Sons, Ltd., 1st ed., 2008.

[8] P. A. Tipler and G. Mosca, *Physik für Wissenschaftler und Ingenieure*. München: Elsevier GmbH, 2nd ed., 2004.

[9] H. Hofman and J. Spindler, *Werkstoffe in der Elektrotechnik, Grundlagen – Struktur – Eigenschaften – Prüfung – Anwendung – Technologie*. München: Carl Hanser Verlag GmbH & Co. KG, 7th ed., 2013.

[10] C.-D. Wuppermann and A. Schoppa, *Merkblatt 401: Elektroband und -blech*. Düsseldorf: Stahl-Informations-Zentrum, 2005.

[11] A. Krings and J. Soulard, "Overview and comparison of iron loss models for elelectric machines," in *International Conference on Ecological Vehicles and Renewable Energies*, 2010.

[12] R. Fischer, *Elektrische Maschinen*. München: Carl Hanser Verlag GmbH & Co. KG, 16th ed., 2013.

[13] CEN, Europäisches Komitee für Normung, *EN 10106: Kaltgewalztes nichtkornorientiertes Elektroblech und -band im schlußgeglühten Zustand*. CEN Zentralsekretariat, Brüssel, 1995.

[14] G. Müller, K. Vogt, and B. Ponick, *Berechnung elektrischer Maschinen*. Weinheim: WILEY-VCH Verlag CmbH & Co. KGaA, 6th ed., 2008.

[15] Z. Zhu and D. Howe, "Electrical machines and drives for electric, hybrid, and fuel cell vehicles," *Proceedings of the IEEE*, vol. 95, no. 4, pp. 746–765, 2007.

[16] L. J. Wu, Z. Zhu, D. Staton, M. Popescu, and D. Hawkins, "Analytical model for predicting magnet loss of surface-mounted permanent magnet machines accounting for slotting effect and load," *IEEE Transactions on Magnetics*, vol. 48, no. 1, pp. 107–117, 2012.

[17] S.-H. Han, T. Jahns, and Z. Zhu, "Analysis of rotor core eddy-current losses in interior permanent-magnet synchronous machines," *IEEE Transactions on Industry Applications*, vol. 46, no. 1, pp. 196–205, 2010.

[18] K. Schwarz, "Survey of basic stray losses in squirrel-cage induction motors," *Proceedings of the Institution of Electrical Engineers*, vol. 111, no. 9, pp. 1565–1574, 1964.

[19] P. Richardson, "Stray losses in synchronous electrical machinery," *Journal of the Institution of Electrical Engineers - Part I: General*, vol. 92, no. 59, pp. 437–438, 1945.

[20] M. Schmitz, *Fahrzyklusgerechte Auslegung einer Asynchronmaschine für Elektrofahrzeuge*. PhD thesis, Rheinisch-Westfälische Technische Hochschule Aachen, 1998.

[21] SKF, *Rolling bearings*. PUB BU/P1 10000/2 EN, SKF Goup, 2013.

[22] Schaeffler Technologies, *Wälzlager*. Herzogenaurach and Schweinfurt: Schaeffler Technologies AG & Co. KG, 2012.

[23] W. Qian, *Dynamic Simulation of Cylindrical Roller Bearings*. PhD thesis, Rheinisch-Westfälische Technische Hochschule Aachen, 2013.

[24] International Organization for Standardization, *ISO 15312:2003(E): Rolling bearings – Thermal speed rating – Calculation and coefficients*. ISO, Geneva, 2003.

[25] Brändlein, Eschmann, Hasbargen, and Weigand, *Die Wälzlagerpraxis*. Mainz: Vereinigte Fachverlage GmbH, 3rd ed., 1998.

[26] J. E. Vrancik, "Prediction of windage power loss in alternators," NASA Technical Note TN D-4849, Lewis Research Center, Cleveland, Ohio, 1968.

[27] J. Saari, *Thermal Analysis of High-Speed Induction Machines*. PhD thesis, Helsinki University of Technology, 1998.

[28] G. I. Taylor, "Stability of a viscous liquid contained between two rotating cylinders," *Philosophical Transactions of the Royal Society of London. Series A, Containg Papers of a Mathematical or Physical Character*, vol. 223, pp. 289–343, 1923.

[29] T. Lu, *Weiterentwicklung von hochtourigen permanenterregten Drehstromantrieben mit Hilfe von Finite-Elemente-Berechnungen und experimentellen Untersuchungen*. PhD thesis, Technische Universität Darmstadt, 2004.

[30] F. P. Incropera, D. P. Dewitt, T. L. Bergman, and A. S. Lavine, *Introduction to Heat Transfer*. Hoboken, NJ: John Wiley & Sons, Inc., 5th ed., 2007.

[31] W. S. Janna, *Engineering Heat Transfer*. Boca Raton: Taylor & Francis Group, LLC, 3rd ed., 2009.

[32] L. Prandtl and A. Betz, *Vier Abhandlungen zur Hydrodynamik und Aerodynamik (Flüssigkeit mit kleiner Reibung; Tragflügeltheorie, I. und II. Mitteilung; Schraubenpropeller mit geringstem Energieverlust)*. Göttingen: Selbstverlag des Kaiser-Wilhelm-Instituts für Strömungsforschung, 1927. Reprint.

[33] J. P. Holman, *Heat Transfer*. New York: The McGraw-Hill Companies, Inc., 10th ed., 2010. International Edition.

[34] Verein Deutscher Ingenieure, VDI-Gesellschaft Verfahrenstechnik und Chemieingenieurwesen, *VDI-Wärmeatlas*. Berlin and Heidelberg: Springer-Verlag, 11th ed., 2013.

[35] A. F. Mills, *Basic Heat & Mass Transfer*. Upper Saddle River: Prentice Hall, Inc., 2nd ed., 1999.

[36] P. Mellor, D. Roberts, and D. Turner, "Lumped parameter thermal model for electrical machines of TEFC design," *Electric Power Applications, IEE Proceedings B*, vol. 138, no. 5, pp. 205–218, 1991.

[37] F. P. Incropera, D. P. Dewitt, T. L. Bergman, and A. S. Lavine, *Fundamentals of Heat and Mass Transfer*. Hoboken, NJ: John Wiley & Sons, Inc., 6th ed., 2007.

[38] D. Roberts, *The application of an induction motor thermal model to motor protection and other functions*. PhD thesis, University of Liverpool, 1986.

[39] CD-adapco, *STAR-CCM+ User Guide, Version 10.02*, 2015.

[40] T. Cebeci, J. P. Shao, F. Kafyeke, and E. Laurendeau, *Computational Fluid Dynamics for Engineers*. Long Beach: Horizons Publishing Inc., 2005.

[41] R. Schwarze, *CFD-Modellierung: Grundlagen und Anwendungen bei Strömungsprozessen*. Berlin, Heidelberg: Springer-Verlag, 2013.

[42] J. Lindström, *Development of an Experimental Permanent-Magnet Motor Drive*. Licentiate thesis, Chalmers University of Technology, 1999.

[43] A. Di Gerlando and I. Vistoli, "Improved thermal modelling of induction motors for design purposes," in *Sixth International Conference on Electrical Machines and Drives*, pp. 381–386, 1993.

[44] JSOL Corporation, *JMAG User's Manual, Version 14.1, Volume 2, Solver*, 2015.

[45] The MathWorks, Inc., *MATLAB R2011b Help*, 2011.

[46] Motor Design Ltd., *Motor-CAD v.7.4 Manual*, 2013.

[47] R. Bongartz, *Creo Parametric 2.0 - Einstiegskurs für Maschinenbauer*. Wiesbaden: Springer Fachmedien, 2013.

[48] S. Nategh, A. Krings, O. Wallmark, and M. Leksell, "Evaluation of impregnation materials for thermal management of liquid-cooled electric machines," *IEEE Transactions on Industrial Electronics*, vol. 61, no. 11, pp. 5956–5965, 2014.

[49] D. Staton, A. Boglietti, and A. Cavagnino, "Solving the more difficult aspects of electric motor thermal analysis in small and medium size industrial induction motors," *IEEE Transactions on Energy Conversion*, vol. 20, no. 3, pp. 620–628, 2005.

[50] A. Boglietti, A. Cavagnino, and D. Staton, "Determination of critical parameters in electrical machine thermal models," *IEEE Transactions on Industry Applications*, vol. 44, no. 4, pp. 1150–1159, 2008.

[51] D. Kulkarni, G. Rupertus, and E. Chen, "Experimental investigation of contact resistance for water cooled jacket for electric motors and generators," *IEEE Transactions on Energy Conversion*, vol. 27, pp. 204–210, March 2012.

[52] J. Fan, C. Zhang, Z. Wang, Y. Dong, C. Nino, A. Tariq, and E. Strangas, "Thermal analysis of permanent magnet motor for the electric vehicle application considering driving duty cycle," *IEEE Transactions on Magnetics*, vol. 46, no. 6, pp. 2493–2496, 2010.

[53] A. EL-Refaie, N. Harris, T. Jahns, and K. Rahman, "Thermal analysis of multibarrier interior PM synchronous machine using lumped parameter model," *IEEE Transactions on Energy Conversion*, vol. 19, no. 2, pp. 303–309, 2004.

[54] J. Fan, C. Zhang, Z. Wang, and E. Strangas, "Thermal analysis of water cooled surface mount permanent magnet electric motor for electric vehicle," in *International Conference on Electrical Machines and Systems (ICEMS), 2010*, pp. 1024–1028, 2010.

[55] V. Gnielinski, "New equations for heat and mass transfer in turbulent pipe and channel flow," *Int. Chem. Eng*, vol. 16, no. 2, pp. 359–368, 1976.

[56] W. Schmidt, H. G. Boldlehner, C. Mann, M. Nast, R. Schmid, B. Pertl, S. Meister, H. Köfler, and E. Bäuerle, *Umweltverträgliche Harzimprägnierung elektrischer Maschinen mittels Stromwärme*. Bundesministerium für Verkehr, Innovation und Technologie, Wien, 2006.

[57] International Electrotechnical Commission, *IEC 60317-0-1: Specifications for particular types of winding wires – Part 0-1: General requirements – Enamelled round copper wire*. IEC, Geneva, 2008.

[58] International Electrotechnical Commission, *IEC 60317-13: Polyester or polyesterimide overcoated with polyamide-imide enamelled round copper wire, class 200*. IEC, Geneva, 2010.

[59] T. J. Murray, "Poly(amide-imides): Wire enamels with excellent thermal and chemical properties," *Macromolecular Materials and Engineering*, vol. 293, no. 5, pp. 350–360, 2008.

[60] Synflex Elektro GmbH, *Voltatex® 4000 1K-Tränkharz – Voltatex® 4250 1K-Tränkharz*. Datasheets.

[61] International Electrotechnical Commission, *IEC 60085: Electrical Insulation – Thermal evaluation and designation*. IEC, Geneva, 2007.

[62] S. Nategh, *Thermal Analysis and Management of High-Performance Electrical Machines*. PhD thesis, KTH School of Electrical Engineering, 2013.

[63] H. Simbürger, "Vergleichende Beurteilung von Tränkmitteln in Elektroisoliersystemen," *11. Fachtagung Elektroisoliersysteme*, 2004.

[64] Phoenix Technologies International LLC, *Polyethylene terephthalate, Key Properties*. Datasheet.

[65] Goodfellow Corporation, *Polyethylene terephthalate*. Datasheet.

[66] E. I. du Pont de Nemours and Company, *NOMEX® Typ 410*. Datasheet.

[67] E. I. du Pont de Nemours and Company, *NOMEX® paper and pressboard: a range of engineering materials*. Datasheet.

[68] International Electrotechnical Commission, *IEC 60404-1-1: Magnetic materials - Part 1-1: Classification – Surface insulations of electrical steel sheet, strip and laminations*. IEC, Geneva, 2004.

[69] N. Brachthäuser, "Elektromobilität – Neue Herausforderungen an den Werkstoff Elektroband," in *11. Umformtechnischen Kolloquium, Darmstadt*, 2012.

[70] Cogent Power Ltd., *Electrical Steel, Thin Non Oriented*. Datasheet.

[71] T. Knopik, *Steigerung des Wirkungsgrades und der Ausnutzung von Norm-Asynchronmotoren mit Kurzschlusskäfig*. PhD thesis, Technische Universität Darmstadt, 2012.

[72] G. Kylander, *Thermal modelling of small cage induction motors*. PhD thesis, Charmers University of Technology, Göteborg, 1995.

[73] A. Boglietti, A. Cavagnino, M. Lazzari, and M. Pastorelli, "A simplified thermal model for variable-speed self-cooled industrial induction motor," *IEEE Transactions on Industry Applications*, vol. 39, no. 4, pp. 945–952, 2003.

[74] F. Unger, "Die Wärmeleitung in Runddrahtspulen," *Archiv für Elektrotechnik*, vol. 41, no. 7, pp. 357–364, 1955.

[75] J. Hak, "Der Wärmewiderstand zwischen Zahn und Joch," *Archiv für Elektrotechnik*, vol. 45, no. 1, pp. 49–58, 1960.

[76] A. Boglietti, A. Cavagnino, D. Staton, M. Shanel, M. Mueller, and C. Mejuto, "Evolution and modern approaches for thermal analysis of electrical machines," *IEEE Transactions on Industrial Electronics*, vol. 56, no. 3, pp. 871–882, 2009.

[77] S. Nategh, O. Wallmark, M. Leksell, and S. Zhao, "Thermal analysis of a PMaSRM using partial FEA and lumped parameter modeling," *IEEE Transactions on Energy Conversion*, vol. 27, no. 2, pp. 477–488, 2012.

[78] G. Longobardo and H. Elrod, "An experimental study of heat transfer at high temperature differences in turbulent air flow between a rotating cylinder and a stationary concentric outer cylinder." Final Report No. AFOSR 3207, Columbia University, 1962.

[79] D. A. Howey, P. R. N. Childs, and A. S. Holmes, "Air-gap convection in rotating electrical machines," *IEEE Transactions on Industrial Electronics*, vol. 59, no. 3, pp. 1367–1375, 2012.

[80] J. Hak, "Der Luftspalt-Wärmewiderstand einer elektrischen Maschine," *Archiv für Elektrotechnik*, vol. 42, no. 5, pp. 257–272, 1956.

[81] H. Neudorfer, *Thermische Untersuchung und Berechnung eines flüssigkeitsgekühlten Traktionsmotors mit Getriebewellenkühlung*. PhD thesis, Technische Universität Wien, 1998.

[82] G. Dajaku, *Electromagnetic and Thermal Modeling of Highly Utilized PM Machines*. PhD thesis, Universität der Bundeswehr München, 2006.

[83] C. Mademlis, N. Margaris, and J. Xypteras, "Magnetic and thermal performance of a synchronous motor under loss minimization control," *IEEE Transactions on Energy Conversion*, vol. 15, no. 2, pp. 135–142, 2000.

[84] M. Polikarpova, P. Röyttä, J. Alexandrova, S. Semken, J. Nerg, and J. Pyrhönen, "Thermal design and analysis of a direct-water cooled direct drive permanent magnet synchronous generator for high-power wind turbine application," in *XXth International Conference on Electrical Machines (ICEM)*, pp. 1488–1495, 2012.

[85] V. Hatziathanassiou, J. Xypteras, and G. Archontoulakis, "Electrical-thermal coupled calculation of an asynchronous machine," *Archiv für Elektrotechnik*, vol. 77, no. 2, pp. 117–122, 1994.

[86] K. Ball, B. Farouk, and V. Dixit, "An experimental study of heat transfer in a vertical annulus with a rotating inner cylinder," *International Journal of Heat and Mass Transfer*, vol. 32, no. 8, pp. 1517 – 1527, 1989.

[87] K. Mizuta, T. Inoue, Y. Takahashi, S. Huang, K. Ueda, and H. Omokawa, "Heat transfer characteristics between inner and outer rings of an angular ball bearing," *Heat Transfer–Asian Research*, vol. 32, no. 1, pp. 42–57, 2003.

[88] G. Stachowiak and A. Batchelor, *Engineering Tribology*. Burlington and Oxford: Elsevier Butterworth-Heinemann, 3rd ed., 2005.

[89] R. Guilbault, "A simplified thermal analysis of elastohydrodynamic contacts," *Journal of Tribology*, vol. 135, no. 2, pp. 021502-1–021502-13, 2013.

[90] A. Boglietti and A. Cavagnino, "Analysis of the endwinding cooling effects in TEFC induction motors," *IEEE Transactions on Industry Applications*, vol. 43, no. 5, pp. 1214–1222, 2007.

[91] A. Boglietti, A. Cavagnino, D. Staton, and M. Popescu, "Experimental assessment of end region cooling arrangements in induction motor endwindings," *Electric Power Applications, IET*, vol. 5, no. 2, pp. 203–209, 2011.

[92] M. Hettegger, B. Streibl, O. Biro, and H. Neudorfer, "Identifying the heat transfer coefficients on the end-windings of an electrical machine by measurements and simulations," in *XIXth International Conference on Electrical Machines (ICEM)*, pp. 1–5, 2010.

[93] M. Hettegger, A. Reinbacher-Kostinger, and O. Biro, "Characterizing the convective wall heat transfer on convoluted shapes in the end-region of an induction machine," in *XXth International Conference on Electrical Machines (ICEM)*, pp. 1219–1226, 2012.

[94] CD-adapco, "STAR-CCM+ & SPEED for Electric Machine Cooling Analysis," *dynamics*, no. 33, pp. 43–46, 2012.

[95] R. Richter, *Elektrische Maschinen, Allgemeine Berechnungselemente, Die Gleichstrommaschine*, vol. 1. Basel: Birkhäuser Verlag Basel und Stuttgart, 3rd expanded ed., 1967.

[96] W. Nürnberg, *Die Asynchronmaschine – Ihre Theorie und Berechnung unter besonderer Berücksichtigung der Keilstab- und Doppelkäfigläufer*. Berlin, Göttingen and Heidelberg: Springer-Verlag OHG, 1952.

[97] A. Binder, *Elektrische Maschinen und Antriebe, Grundlagen, Betriebsverhalten*. Berlin and Heidelberg: Springer-Verlag, 2012.

[98] I. Boldea and S. A. Nasar, *The Induction Machines Design Handbook*. Boca Raton: CRC Press, 2nd ed., 2010.

[99] A. Boglietti, A. Cavagnino, and M. Lazzari, "Computational algorithms for induction motor equivalent circuit parameter determination—part ii: Skin effect and magnetizing characteristics," *IEEE Transactions on Industrial Electronics*, vol. 58, no. 9, pp. 3734–3740, 2011.

[100] Institut für Elektrische Maschinen der RWTH Aachen, "Entwurf, Berechnung und Technologie elektrischer Maschinen. Vorlesung an der RWTH Aachen von Univ.-Prof. Dr.-Ing. habil. Dr. h.c. Kay Hameyer." Lecture notes, 2007.

Abbreviations

av. . . . . **av**erage

CAD . . . . . **c**omputer-**a**ided **d**esign

CFD . . . . . **c**omputational **f**luid **d**ynamics

coef. . . . . **coef**ficient

CPU . . . . . **c**entral **p**rocessing **u**nit

DC . . . . . **d**irect **c**urrent

DE . . . . . **d**rive **e**nd (side)

DIN . . . . . **D**eutsches **I**nstitut für **N**ormung e.V. (**e**ingetragener **V**erein)

DUT . . . . . **d**evice **u**nder **t**est

EAM . . . . . Institut für **E**lektrische **A**ntriebstechnik und **M**aschinen

EMAG . . . . . **e**lectro**mag**netic

EN . . . . . European standard

ETP . . . . . **e**lectrolytic **t**ough **p**itch

FEM . . . . . **f**inite **e**lement **m**ethod

FVM . . . . . **f**inite **v**olume **m**ethod

IEC . . . . . **I**nternational **E**lectrotechnical **C**ommission

IM . . . . . **i**nduction **m**achine

ISO . . . . . **I**nternational **O**rganization for **S**tandardization

max. . . . . **max**imum

mech. . . . . **mech**anical

min. . . . . **min**imum

MMF . . . . . **m**agneto**m**otive **f**orce

mod. . . . . **mod**ified

NDE . . . . . **n**on-**d**rive **e**nd (side)

ÖVE . . . . . **Ö**sterreichischer **V**erband für **E**lektrotechnik

PAI . . . . . **p**oly**a**mide-**i**mide

PEI . . . . . **p**oly**e**ster**i**mide

PET . . . . . **p**oly**e**thylene **t**erephthalate

PM . . . . . **p**ermanent **m**agnet

pu . . . . . **p**er-**u**nit

RAM . . . . . **r**andom-**a**ccess **m**emory

RMS . . . . . **r**oot **m**ean **s**quare

RTD . . . . . **r**esistance **t**emperature **d**etector

TC . . . . . **t**hermo**c**ouple

TEFC . . . . . **t**otally **e**nclosed **f**an-**c**ooled

List of figures

List of tables